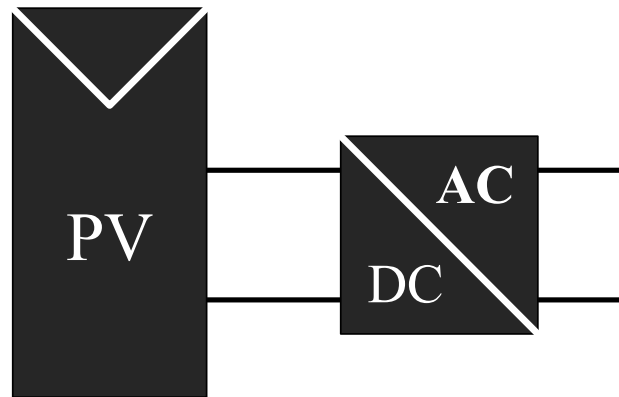




**TÉCNICO**  
LISBOA



## **Backstepping Control of a Photovoltaic DC/AC Converter**

**Calvin Mikael Pinto Santana**

Thesis to obtain the Master of Science Degree in  
**Electrical and Computer Engineering**

Supervisor: Prof. José Fernando Alves da Silva

### **Examination Committee**

Chairperson: Prof. Rui Manuel Gameiro de Castro

Supervisor: Prof. José Fernando Alves da Silva

Member of the Committee: Dr. Victor Manuel de Carvalho Fernão Pires

**November 2016**



# Acknowledgements

First of all I would like to thank my mother and brother for their unconditional support during my academic journey, even during the years that I may not have warranted such trust, without you I would not have been able to conclude this chapter of my life the way that I wanted to. I would also like to thank my maternal grandparents, aunt and cousins for all their help and positive encouragement.

A special thanks to my colleagues and friends Dinis Carreira, Temóteo Tembe and Atish Jaitilal for always being a positive influence and never shying away from helping me when needed. To any other colleagues and friends that I may have not mentioned thank you for your friendship and comradeship.

Last but not least, I would like to thank my dissertation supervisor Prof. Dr. J. Fernando Silva for his insight, patience and readiness to help and apologize for any troubles that I may or may not have caused.

Lisbon, Instituto Superior Técnico  
November, 2016

Calvin Santana

# Resumo

No contexto das energias renováveis, e em particular, na energia solar, a redução dos preços por painel solar tem levado a um contínuo crescimento no número de consumidores que utilizam sistemas fotovoltaico, e em particular, sistemas micro-inversor.

Ao contrário de sistemas PV tradicionais, onde os seus conversores de potência encontram-se instalados em abrigos, os micro-inversor são instalados na parte de trás dos painéis, o que faz com que eles sejam sujeitos às condições atmosféricas mais adversas, nomeadamente a temperaturas mais elevadas. Isto significa que a fiabilidade será afectada, tornando-se necessário acautelar que os elementos electrónicos a utilizar nos micro-inversor não sejam muito sensíveis a condições adversas.

Nesta dissertação, é proposto uma topologia de micro-inversor que garantirá uma maior fiabilidade. Isto é conseguido através da eliminação dos elementos que são mais sensíveis a alterações de temperatura, os condensadores electrolítico. Além de uma maior fiabilidade também são conseguidos rendimentos elevados para este tipo de sistema PV.

Para controlar este sistema serão dimensionados dois sistemas de controlo, de forma a maximizar a energia extraída do painel e a qualidade da energia injectada na rede. Ambos os sistemas de controlo terão de garantir uma elevada robustez a alterações atmosféricas ou da própria rede energética.

O primeiro controlador projectado utiliza técnicas lineares de controlo e servirá como referência para comparação. O segundo controlador projectado é baseado em teoria não linear de controlo, mais especificamente a teoria de estabilidade desenvolvida por Lyapunov. A técnica de controlo utilizado é o *backstepping* que é baseado no segundo teorema de Lyapunov. Para facilitar o cálculo das derivadas presentes em *backstepping* serão utilizadas filtros específicos designados de *command filters*.

**Palavras chave:** Micro-inversor, condensadores electrolítico, fiabilidade, controlo linear e controlo não linear.

# Abstract

In the context of renewable energies, and in particular solar power, the decrease in price of PV modules has led to a continued increase of the number of householders who use photovoltaic systems, in particular, AC modules (or microinverters).

Unlike conventional PV system topologies where the power converters are typically located indoors, the electronics in PV microinverters will reside in the same outdoor environment as the PV module, which exposes them to harsher and more variable operating conditions, mainly increased temperatures. This means that guaranteeing higher reliability becomes a more crucial task when compared to other topologies.

A highly reliable, current-fed microinverter is proposed, without the traditional problematic electrolytic capacitor, while simultaneously achieving a high nominal and European Weighted Efficiency.

Two different control systems that guarantee maximum power point tracking (MPPT) and DC-AC power control are implemented and compared in order to evaluate each control system in terms of: power quality, efficiency, operation span and dynamic response performance to atmospheric or grid changes.

The first control system utilizes linear control laws to stabilize and control the nonlinear system and will be used as a reference for comparison. The second control system utilizes nonlinear control techniques based on Lyapunov's second law, which include: backstepping control design and command filtering backstepping control design.

**Keywords:** Microinverter, Electrolytic-Less converter, Linear Control, Nonlinear Control, Lyapunov's Second Law, Backstepping control design and Command Filtering Backstepping.

# Contents

<b>Acknowledgements</b>	<b>i</b>
<b>Resumo</b>	<b>ii</b>
<b>Abstract</b>	<b>iii</b>
<b>Contents</b>	<b>iv</b>
<b>List of Figures</b>	<b>vii</b>
<b>List of Tables</b>	<b>x</b>
<b>List of Acronyms</b>	<b>xi</b>
<b>List of Symbols</b>	<b>xii</b>
<b>1 Introduction</b>	<b>1</b>
1.1 Background	1
1.2 Photovoltaic System	2
1.3 PV System Configurations	3
1.3.1 AC-Module Topology	3
1.3.2 String Inverter Topology	3
1.3.3 Multistring Topology	4
1.3.4 Central Topology	5
1.4 Motivation	6
1.5 Thesis Objective	7
1.6 Thesis Outline	7
<b>2 Power Decoupling Techniques</b>	<b>8</b>
2.1 PV-Side Decoupling	9
2.2 DC-Link Decoupling	11
2.2.1 Isolated Current-Fed DC-DC Topologies	11
<b>3 Nonlinear Lyapunov Control</b>	<b>14</b>
3.1 Lyapunov Stability	14
3.2 Lyapunov's Second Method	16
3.2.1 Control Lyapunov Functions	16
3.2.2 Backstepping Design	17
3.2.3 Command Filtering Backstepping	19

<b>4</b>	<b>PV-Module</b>	<b>21</b>
4.1	Mathematical Model	21
4.1.1	Computation of Model Parameters	22
4.1.2	Influence of Irradiance and Temperature on I-V Curve	24
4.1.3	PV Cell Temperature	25
4.2	Implementation of the Mathematical Model	25
<b>5</b>	<b>Proposed Microinverter</b>	<b>29</b>
5.1	Introduction	29
5.2	Active-Clamp Full-Bridge Boost Converter	29
5.2.1	Design Procedure	32
5.2.2	Transformer Turns Ratio	33
5.2.3	Transformer Parameters	33
5.2.4	Intermediate Inductor	34
5.2.5	Active-Clamp Capacitor	35
5.2.6	Active Components of Full-Bridge Inverter and Active-Clamp	36
5.3	Grid Inverter	39
5.3.1	DC Capacitors	40
5.3.2	AC Inductor	41
5.3.3	Active Components of Rectifier	43
5.3.4	Active Components of Inverter	44
5.4	Equivalent Losses	45
5.4.1	Conduction Losses	45
5.4.2	Switching Losses	46
5.4.3	Efficiency	47
<b>6</b>	<b>Maximum Power Point Tracking Control</b>	<b>48</b>
6.1	Introduction	48
6.2	Maximum Power Point Tracking	48
6.3	Pulse Width Modulation	52
6.4	Linear PI Controller of MPPT	54
6.4.1	PI Controller Stability Analysis	57
6.4.2	Anti-Windup	60
6.5	Nonlinear Backstepping Control of MPPT	61
<b>7</b>	<b>DC-AC Inverter Power Control</b>	<b>63</b>
7.1	Linear PI Controller of DC-Link	63
7.1.1	PI Controller Stability Analysis	66
7.1.2	Near Unity Power Factor Control	68
7.2	Nonlinear Backstepping Control of DC-Link	69
7.2.1	Gain Selection	71
<b>8</b>	<b>Simulation and Performance Analysis</b>	<b>72</b>
8.1	Varying Atmospheric Conditions	73
8.2	European Weighted Efficiency	77
8.3	Unbalanced Initial Voltages	77
8.4	Grid Disturbances	79

<b>9</b>	<b>Conclusions and Recommendations . . . . .</b>	<b>81</b>
9.1	Final Conclusions . . . . .	81
9.2	Recommendations . . . . .	82
	<b>Bibliography . . . . .</b>	<b>83</b>
	<b>Appendices . . . . .</b>	<b>87</b>
	<b>Appendix A MATLAB/Simulink Implementations . . . . .</b>	<b>87</b>
	<b>Appendix B Datasheets . . . . .</b>	<b>90</b>

# List of Figures

1.1	PV Module (or Solar panel) and respective PV cells. (source [9]) . . . . .	2
1.2	Location of Power Converters for different PV system configurations (source [17]). . . . .	4
1.3	Power converters used by different PV configuration systems. (source [10]) . . . . .	5
2.1	a) DC-Link Decoupling and b) PV-Side Decoupling. . . . .	8
2.2	Capacitance/voltage ranges for each capacitor technology. . . . .	9
2.3	a) Single-transistor flyback-type HF-link inverter and b) Flyback-type inverter with high-power decoupling [17]. . . . .	10
2.4	Active power decoupling control modes. (source [23]) . . . . .	10
2.5	Maximum allowed voltage ripple at the DC-link capacitor(s) in order for the voltage source inverter (VSI) to have a correct behaviour. . . . .	12
2.6	Isolated current-fed DC-DC topologies: a) ZVS-PWM Full-Bridge Boost Converter [25] b) Active-clamp Full-Bridge Boost Converter [26] c) Current-Fed ZCS High Frequency Inverter-applied Resonant DC-DC Converter for Inductive Power Transfer [27] and d) Soft-Switching Current-Fed Push-Pull Converter [28]. . . . .	13
3.1	Lyapunov stability in $\mathbb{R}^2$ . (source [37]) . . . . .	15
3.2	Example of a positive definite Lyapunov function with $\underline{x} \in \mathbb{R}^2$ . . . . .	17
3.3	Command filter (CF) block diagram [37],[38]. . . . .	19
3.4	Block diagram of the CFBS approach for $n = 3$ . The virtual controls $\alpha_i$ are computed according to (3.11). The dotted lines from the CF to the $\alpha_i$ represent the communication of the command derivative $\dot{\alpha}_i$ from the CF to the computation of $\alpha_{i+1}$ [38]. Colours have been added to highlight the pattern of repetitiveness in the construction. . . . .	20
4.1	Equivalent electrical circuit of a PV cell (One-Diode, five parameters model). . . . .	21
4.2	IV-curves for different levels of irradiance (with $\theta_c = 25^\circ C$ ). Left: Simulink Simulation. Right: PV Catalog. . . . .	26
4.3	IV-curves for different levels of temperature (with $G = 1000 W/m^2$ ). Left: Simulink Simulation. Right: PV Catalog. . . . .	26
4.4	Left: IV-curves with highlighted $V_{ca}$ and $I_{cc}$ points. Right: PV module power with highlighted $MPP$ point. . . . .	27
5.1	Proposed AC-module circuit. . . . .	29
5.2	Active-Clamp Boost Full-Bridge converter operation modes. . . . .	30
5.3	Expected waveforms of the Active-Clamp Boost Full-bridge converter. . . . .	31
5.4	Equivalent Electrical Transformer Circuit. . . . .	33
5.5	Resonant Tank Formed between $C_c$ and $L_\lambda$ . . . . .	36
5.6	Semiconductors highlighted (a): Transfer mode (b): Current boost mode. . . . .	37

5.7	Main voltages and currents of the half-bridge rectifier and grid inverter. . . . .	39
5.8	Power decoupling achieved by the buffer circuit. (source [34]) . . . . .	40
5.9	AC inductor responsible for enabling unity power factor and respective vector diagram. . . . .	42
5.10	Equivalent approximated real life components. . . . .	45
5.11	Expected evolution of efficiency. . . . .	47
6.1	Complete AC-module, respective controllers and electrical measurements. . . . .	48
6.2	Characteristic curves of the PV module. . . . .	49
6.3	Power curve (black) and its derivative (blue) for different levels of irradiance ( $[W/m^2]$ : Solid – 1000, dash – 800, dash-dot – 600 and dot – 400) and constant cell temperature of $25^\circ C$ . The red dashed line represents the proposed hysteresis band and the highlighted red dots the MPPT oscillation. . . . .	50
6.4	Power curve (black) and its derivative (blue) for different levels of cell temperature ( $[^\circ C]$ : Solid – 65, dash – 45, dash-dot – 25 and dot – 5) and constant irradiance of $1000 W/m^2$ . The red dashed line represents the proposed hysteresis band and the highlighted red dots the MPPT oscillation. . . . .	51
6.5	Hysteresis band maximum power point tracking control of $I_{mp}$ (virtual current), which is then fed into a controller that guarantees fixed frequency by computing the necessary duty cycle indirectly through $u_c$ . . . . .	52
6.6	3-Level PWM Flowchart. . . . .	52
6.7	3-Level PWM logic circuit. . . . .	53
6.8	3-Level PWM main waveforms. . . . .	53
6.9	Different stages of the Active-Clamp Full-Bridge Boost converter. . . . .	55
6.10	Block diagram of the feedback system of the MPPT current control. . . . .	55
6.11	Root-Locus of the current control system. Left: Neglecting higher order poles of the power converter. Right: Considering the 2nd order pole, which causes instability for high gains. . . . .	58
6.12	Left: Open-loop Bode Plot. Right: Nyquist Plot. The blue line represents the simplified TF while the orange line accounts for the 2nd order TF of the power converter. . . . .	58
6.13	Left: Closed-loop step response. Right: Sensitivity bode Plot. The blue line represents the simplified TF while the orange line accounts for the 2nd order TF of the power converter. . . . .	59
6.14	PI controller with a saturation block and an extra feedback loop used for Anti-Windup (based on Back-Calculation). . . . .	60
7.1	Block diagram of linearised voltage control. . . . .	65
7.2	Root Locus of DC-Link voltage control. . . . .	67
7.3	Step Response of DC-Link voltage control. . . . .	67
7.4	Illustration of the current ripple and respective control by the hysteresis upper and lower limits. . . . .	69
7.5	Hysteresis band nonlinear control. . . . .	69
8.1	MPPT current control. Top Fig.) <b>TCT</b> approach. Bottom Fig.) <b>CFBS</b> approach. . . . .	73
8.2	DC-AC Voltage Control. Top Fig.) <b>TCT</b> approach. Bottom Fig.) <b>CFBS</b> approach. . . . .	74
8.3	DC-AC Current Control. Top Fig.) <b>TCT</b> approach. Bottom Fig.) <b>CFBS</b> approach. . . . .	75
8.4	Injected current <i>THD</i> . Top Fig.) <b>TCT</b> approach. Bottom Fig.) <b>CFBS</b> approach. . . . .	75
8.5	Power factor <i>f.p.</i> . Top Fig.) <b>TCT</b> approach. Bottom Fig.) <b>CFBS</b> approach. . . . .	76

8.6	Input and Output Power Curves. Top Fig.) <b>TCT</b> . Bottom Fig.) <b>CFBS</b> . . . . .	76
8.7	Microinverter Efficiency. Top Fig.) <b>TCT</b> approach. Bottom Fig.) <b>CFBS</b> approach. . . . .	77
8.8	DC/AC voltage control when both capacitors are initially discharged. Top Fig.) <b>TCT</b> approach. Bottom Fig.) <b>CFBS</b> approach. . . . .	78
8.9	DC/AC voltage control when capacitors have different initial voltages. Top Fig.) <b>TCT</b> approach. Bottom Fig.) <b>CFBS</b> approach. . . . .	78
8.10	DC/AC control in presence of a grid voltage sag. Top two Fig.) <b>TCT</b> approach. Bottom two Fig.) <b>CFBS</b> approach. . . . .	79
8.11	DC/AC control in the presence of a grid voltage swell. Top two Fig.) <b>TCT</b> approach. Bottom two Fig.) <b>CFBS</b> approach. . . . .	80
A.1	Equivalent mathematical model of the PV module. . . . .	87
A.2	Complete control system using a command filtering backstepping approach. . . . .	88
A.3	Complete control system using traditional control techniques. . . . .	89
B.1	Canadian Solar - CS6K - 270 275 280 PV Module main characteristics. . . . .	90
B.2	Full-Bridge Semiconductors - Part 1 - Absolute Maximum Ratings. . . . .	91
B.3	Full-Bridge Semiconductors - Part 2 - Specifications MOSFET and Body Diode. . . . .	92
B.4	Active-Clamp Semiconductor - Part 1 - Absolute Maximum Ratings. . . . .	93
B.5	Active-Clamp Semiconductor - Part 2 - Specifications MOSFET and Body Diode. . . . .	94
B.6	Half-bridge Rectifier Semiconductor - Part 1 - Absolute Maximum Ratings. . . . .	95
B.7	Half-bridge Rectifier Semiconductor - Part 2 - Characteristic curves. . . . .	96
B.8	Half-bridge Inverter Semiconductor - Part 1 - Absolute Maximum Ratings. . . . .	97
B.9	Half-bridge Inverter Semiconductor - Part 2 - Specifications. . . . .	98
B.10	Film Capacitors - Part 1 - Features. . . . .	99
B.11	Film Capacitors - Part 2 - Electrical data. . . . .	100
B.12	Film Capacitors - Part 3 - Electrical data. . . . .	100

# List of Tables

1.1	Grid-connected PV system configurations overview. . . . .	3
2.1	Comparassion of different isolated current-fed DC-DC topologies. . . . .	13
4.1	PV module main electrical data (Appendix B). . . . .	25
4.2	Computed PV module mathematical model parameters. . . . .	26
4.3	Comparison of the mathematical model results to the PV catalog (Fig. 4.2). . . . .	27
4.4	Comparison of of mathematical model results to PV catalog data (Fig. 4.3). . . . .	27
4.5	Comparison of the mathematical model results to the PV catalog Table data. . . . .	28
5.1	Comparative Table of solar panel test conditions. . . . .	32
5.2	PV module expected output values for different testing conditions. . . . .	32
5.3	Necessary intermediate inductor and duty cycle for different atmospheric conditions. . . . .	35
5.4	Comparison of limit values and chosen semiconductors for the DC-DC converter. . . . .	39
5.5	Comparison of limit values and chosen semiconductors of the DC-AC converter. . . . .	44
5.6	Parasitic resistances responsible for power losses. . . . .	46
5.7	Switching power losses. . . . .	47
6.1	The time constants and gains of the MPPT current PI controller. . . . .	57
7.1	The time constants and gains of the DC-Link voltage PI controller. . . . .	66
8.1	All controller design gains and command filter parameters. . . . .	72

# List of Acronyms

Acronym	Meaning
AC	Alternating Current
CCM	Continuous Conduction Mode
CF	Command Filter
CFBS	Command Filtering Backstepping
CLF	Control Lyapunov function
CSI	Current Source Inverter
DC	Direct Current
DCM	Discontinuous Conduction Mode
DG	Distributed Generation
EPR	Equivalent Parallel Resistance
ESL	Equivalent Series Inductance
ESR	Equivalent Series Resistance
EU	European Union
HF	High-Frequency
HTC	High Temperature Conditions
IGBT	Insulated-Gate Bipolar Transistor
LIC	Low irradiance Conditions
LTC	Low temperature Conditions
LV	Low voltage
MG	Micro Generation
MOSFET	Metal–Oxide–Semiconductor Field-Effect Transistor
MPP	Maximum Power Point
MPPT	Maximum Power Point Tracking
NOCT	Nominal Operating Cell Temperature
pu	Per-unit System
PI	Proportional and Integral
PO	Perturb and Observe
PV	Photovoltaic
PWM	Pulse Width Modulation
RT	Resonant Tank
STC	Standard Test Conditions
TCT	Traditional Control Techniques
TF	Transfer Function
THD	Total Harmonic Distortion
VSI	Voltage Source Inverter
ZCS	Zero-Current Switching
ZVS	Zero-Voltage Switching

# List of Symbols

Roman Symbols	Meaning
$A_p$	Gain margin of PI controller
$b_k$	Polynomial coefficients
$c_*$	Backstepping control gain
$C_c$	Active-clamp capacitor
$D$	Open region containing the origin
$D_*$	Diodes of the half-bridge rectifier
$e_w$	Windup error quantity
$f_p$	Power factor
$f_{pwm}$	PWM frequency
$f_{rt}$	Resonant tank frequency
$f_s$	Working frequency of the transformer
$G$	Irradiance
$I$	PV cell output current
$I_{cc}$	Short-circuit current
$I_D$	p-n junction internal current
$I_{g_p}$	Peak grid current
$I_\lambda$	Primary transformer current
$I_{MP}$	Maximum power point current
$I_S$	Current generated by the PV cell
$I_0$	Diode saturation current
$K$	Boltzmann constant
$K_{iTHD}$	Current total harmonic distortion
$K_{i_V}$	Integration coefficient of DC-link controller
$K_i$	Integration coefficient of MPPT controller
$K_p$	Proportional gain of MPPT controller
$K_{pV}$	Proportional gain of DC-link controller
$K_w$	Anti-Windup feedback gain
$L_{ac}$	Grid-connected AC inductor
$L_{dc}$	Intermediate (boost) inductor
$L_\lambda$	Flux leakage inductor
$L_m$	Transformer equivalent core inductance
$L_p$	Transformer primary leakage inductance
$L_s$	Transformer secondary leakage inductance
$m$	Ideality factor of the diode
$M_p$	Maximum overshoot

$M_s$	Maximum sensitivity
$n$	Transformer turns ratio
$n_p$	Transformer primary turns
$n_s$	Transformer secondary turns
$N_s$	Number of PV cells in series
$N_p$	Number of PV cells in parallel
$P_{buff}$	Power that should be decoupled
$P_{in}$	PV module power
$P_o$	Output power
$P_p$	Peak Power
$Q_*$	Switches of the half-bridge inverter
$q$	Electron charge
$R_m$	Transformer equivalent core resistance
$R_p$	Transformer primary coil resistance
$R_s$	Series resistance of external PV contacts
$R_s$	Transformer secondary coil resistance
$R_{sh}$	Shunt resistance
$S_c$	Active-clamp switch
$S_*$	Switches of the full-bridge boost converter
$t$	Time
$t_e$	Settling time
$t_r$	Rise time
$T$	Absolute temperature
$T_c$	Absolute cell temperature
$T_d$	Average delay of power converter
$T_p$	Time constant of the pole of MPPT controller
$T_{pwm}$	Time period of the pulse width modulation
$T_{pv}$	Time constant of the pole of DC-link controller
$T_{rt}$	Resonant tank period
$T_s$	Time period of the high-frequency transformer
$T_z$	Time constant of the zero of MPPT controller
$T_{zv}$	Time constant of the zero of DC-link controller
$u$	System control input
$u_c$	Reference waveform of 3-level PWM
$u_{cmax}$	Upper limit of PWM carrier
$u_{cmin}$	Bottom limit of PWM carrier
$v_p$	Transformer primary voltage
$v_s$	Transformer secondary voltage
$V$	PV cell output voltage
$V_*$	(Control) Lyapunov function
$V_{ca}$	Open-circuit voltage
$V_{gp}$	Peak grid voltage
$V_{grms}$	RMS grid voltage
$V_o$	DC-link voltage
$V_{MP}$	Maximum power point voltage
$V_p$	Transformer primary voltage
$V_T$	Thermal voltage equivalent

$W$	Positive definitive function
$\underline{x}$	System state vector
$x_e$	Equilibrium point
$x_{f*}$	Filter state
$y_r$	Reference waveform
$z_*$	Tracking error
$\bar{z}_*$	Compensated tracking error
$Z_{Cc}$	Active-clamp capacitor impedance
$Z_{L\lambda}$	Equivalent leakage inductor impedance

Greek Symbols	Meaning
$\alpha_*$	Virtual control (feedback law)
$\alpha_i$	Current measurement gain
$\alpha_v$	Voltage measurement gain
$\gamma$	Mode of operation of DC-DC converter
$\gamma_g$	Mode of operation of DC-AC inverter
$\delta$	Duty-cycle of 3-level PWM
$\beta$	Reference waveform of 2-level PWM
$\Delta i$	Ripple of the current
$\Delta t$	Sampling time
$\Delta v$	Ripple of the voltage
$\epsilon I_{pv}$	PV current error
$\epsilon V_{oREF}$	DC-link voltage error
$\theta$	Angle between apparent and real power
$\theta_a$	Ambient temperature
$\theta_c$	Cell temperature
$\theta_v$	Angle between grid voltage and current
$\cos \varphi_1$	Displacement power factor
$\varphi_c$	Phase margin of PI controller
$\Lambda$	Presence or not of auxiliary snubber circuit
$\mu I_{cc}$	Short-circuit temperature coefficient
$\mu V_{ca}$	Open-circuit temperature coefficient
$\xi$	Damping ratio
$\tau_*$	Time constant
$\chi_*$	Unachieved portion of error
$\phi$	Angle between $v_{pwm}$ and $v_g$
$1\phi$	Single-phase
$\omega_c$	Crossover frequency
$\omega_n$	Natural frequency
$\omega_{pwm}$	PWM angular frequency

# Chapter 1

## Introduction

### 1.1 Background

Since the First World Climate Conference, held on February 1979 in Geneva, many efforts were made towards reducing the footprint made by all sort of mankind activities. In particular, one of the efforts adopted was to reduce the environmental impact of the energy sector by increasing the use of renewable energy sources over fossil fuels. The European Energy Union has set itself energy and climate targets for the next four decades, including reducing greenhouse gases by at least 20% and increasing the renewable energy share up to 20% before the end of 2020 [5].

Traditionally, power systems in Europe have mainly been built to accommodate central power plants, meaning large fossil fuel condensing plants, nuclear plants and hydro power stations. This is changing, more and more distributed energy resources are being introduced into the power system. The distributed energy resources include not just distributed generation, but also energy storage and demand response.

EU Directive 2009/72/EC defines distributed generation (DG) as generation plants connected to the distribution system where the distribution system is the high voltage, medium voltage and low voltage network as opposed to the extra-high voltage and high voltage transmission system. However, a broad consensus is that DG units are connected to the distribution grid and are not large-scale units. Their energy source is produced locally (wind, solar, biomass, biogas, geothermal, ocean energy, hydro) and production is used by the producer (prosumer), or the owner is a relatively small actor on the electricity market. Micro-generation is a term referring to very small generation units connected to the low voltage network, which means capacities below 50 kW [6].

The quantity of renewable energy produced within the EU-28 increased overall by 84.4% between 2003 and 2013, equivalent to an average increase of 6.3% per year [7]. The growth in electricity generated from renewable energy sources largely reflects an expansion in three renewable energy sources, namely wind turbines, solar power and biomass [7].

Solar power deals with the conversion of solar energy into electrical energy, using photovoltaic (PV) panels, or thermal energy, using concentrated solar power technology. PV panels produce electrical current when exposed to solar radiation irradiance (PV Effect) and are typically made of modified silicon. The global efficiency of PV systems are below 15% [8], which highlights the need to develop more efficient manufacturing processes, conversion devices and control techniques.

Many PV systems have so far been connected to the grid due to their relatively cleanness when compared to more traditional energy sources. The price of the PV modules was in the past the major contribution to the cost of these systems. A downward tendency is now seen in the price for the PV modules due to a massive increase in the production capacity of PV modules. A cost reduction per inverter watt is, therefore, important to make PV generated power more attractive. The focus has, therefore, been placed on new, cheap, and innovative inverter solutions, which has resulted in a high diversity within the inverters, and new PV system configurations [17].

## 1.2 Photovoltaic System

Photovoltaic is the direct conversion of light into electricity at the atomic level. Some materials exhibit a property known as the Photoelectric Effect that causes them to absorb photons of light and release electrons. When these free electrons are captured, an electric current results that can be used as electricity. PV systems: include cells, modules, strings, and arrays.

A PV *cell* (or solar cell) is the basic building block of photovoltaic power generation systems. The most common type of PV cell is made from silicon crystal [8], which is specially treated by introducing impurities (doping) to form an electric field (p-n junction), positive on one side (p-type, free holes) and negative on the other (n-type, free electrons). Doping greatly increases the number of charge carriers within the crystal by weakening the valence band. Each cell produces a maximum of 4.5 W (2016), which is clearly not enough for the majority of applications. To solve this problem PV cells are grouped to form a PV *module* (also known as solar *panel*) as is shown in Figure 1.1.

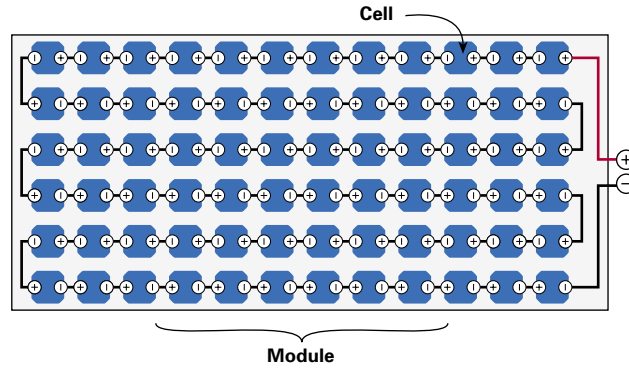


Figure 1.1: PV Module (or Solar panel) and respective PV cells. (source [9])

In general a *module* consists of a number of cells in series  $N_s$ , which increases the voltage, and a number of cells in parallel  $N_p$ , which increases the current. Currently (2016) mono-crystalline silicon PV modules use 60 cells (270 W) while poly-crystalline silicon PV modules use 72 cells (320 W).

A *string* is a group of PV modules wired in series while the term *array* is used to describe a large group of modules which commonly are connected both in series and in parallel on a single rack or multiple racks.

### 1.3 PV System Configurations

Grid-connected PV power generation systems can be found in different sizes and power levels for different needs and applications, ranging from a single PV module from around 200 W to more than a 100 thousand modules for PV plants over 100 MW [10]. The main characteristics of each configuration (topology) are displayed in Table 1.1 while an overview of the location of the power converters in each topology is shown in Figure 1.2.

Table 1.1: Grid-connected PV system configurations overview.

Topology	AC MODULE	STRING	MULTISTRING	CENTRAL
Scale	Small	Medium	Medium/Large	Large
Power Range	< 500 W	< 10 kW	< 500 kW	< 850 kW
Semiconductors	MOSFET	MOSFET/IGBT	MOSFET/IGBT	IGBT
Converter efficiency	Lowest	High	High	Highest
MPPT efficiency	Highest	Good	High	Good

#### 1.3.1 AC-Module Topology

The AC-module configuration uses an individual grid-tied inverter for each PV module of the system (Fig. 1.2). Therefore, this configuration is also known as a microinverter or module-integrated inverter due to the small size and low power rating of the converter.

The LV rating of PV modules (generally around 30 V) requires voltage boost for grid connection. This is why AC-module inverters are usually found with a transformer (at least in Europe, which has a higher grid-voltage when compared to Japan e.g.) to increase the voltage and simultaneously provide galvanic isolation. The presence of the additional transformer means that this is the configuration with the lowest power converter efficiency, which is compensated by the highest MPPT accuracy due to the dedicated converter. Other advantages include lower installation costs, enhanced modularity and flexibility [22].

This configuration is appropriate for locations with lots of partial shading, complex roof structures, small systems, or combinations of different roof orientations. The small size of the converter allows for a very compact enclosure design that is attached to the back of each PV module, hence the name module-integrated inverter. Because of their LV operation, metal-oxide-semiconductor field-effect transistor (MOSFET) devices are most commonly found in these topologies [10].

#### 1.3.2 String Inverter Topology

String inverters connect a single PV string to the grid (Fig. 1.2) and are subdivided into single-stage and two-stage conversion topologies, depending on the addition (or not) of a DC-DC stage used to adapt the DC voltage output from the PV string to the DC side voltage of the grid inverter.

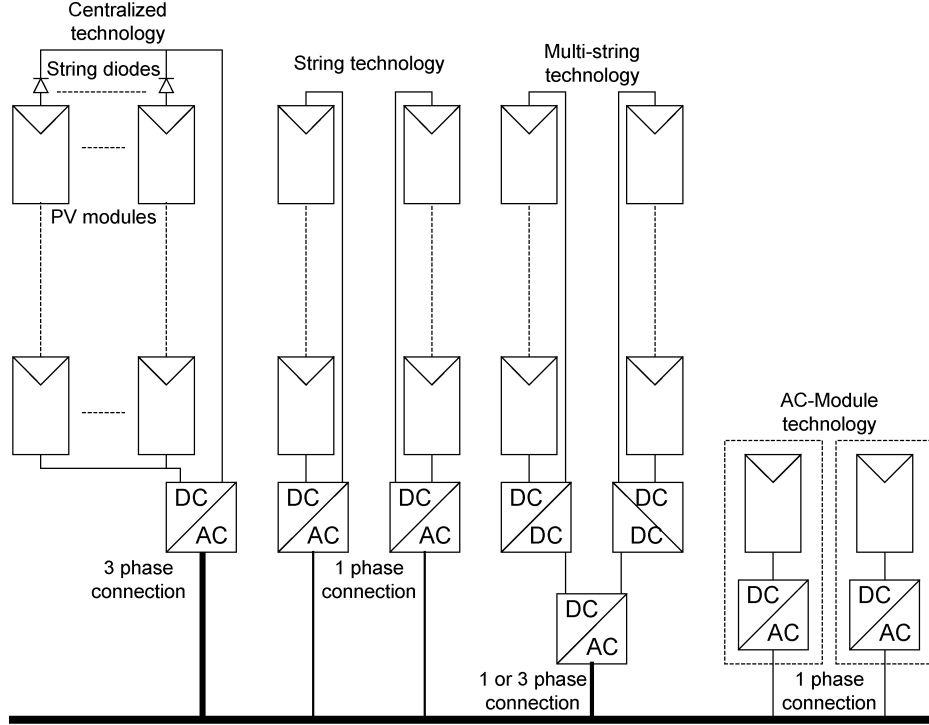


Figure 1.2: Location of Power Converters for different PV system configurations (source [17]).

Furthermore, grid inverters can be found with or without galvanic isolation. Isolation can be introduced at the grid side via a low-frequency transformers (large and heavy) or within the DC–DC stage via a high-frequency transformer (light and compact but with additional losses from several DC–DC converter semiconductors). The different combinations between single or two stage, with transformer or transformerless string inverters, has led to a wide range of different converter configurations, as shown in Figure 1.3.

In comparison to AC-module inverters, the string inverter has a less accurate MPPT which under partial shading reduces the total energy yield. The string inverter is very popular for small to medium scale PV systems, particularly for residential rooftop PV systems.

### 1.3.3 Multistring Topology

To add more flexibility to the string inverter and improve the MPPT performance of the PV system, the multistring concept was developed. The strings are divided into smaller pieces (fewer modules in series) and connected through independent MPPT DC–DC converters to the grid-tied inverter (Fig. 1.2). The DC–DC stage also boosts the voltage of the smaller strings. The additional DC–DC stages are a cost-effective solution compared to having several string inverters. Multistring inverters can also be found with or without isolation (Fig. 1.3). Since they reduce partial shading and mismatching, they are suitable not only for rooftop PV systems, but also for medium and large-scale PV plants.

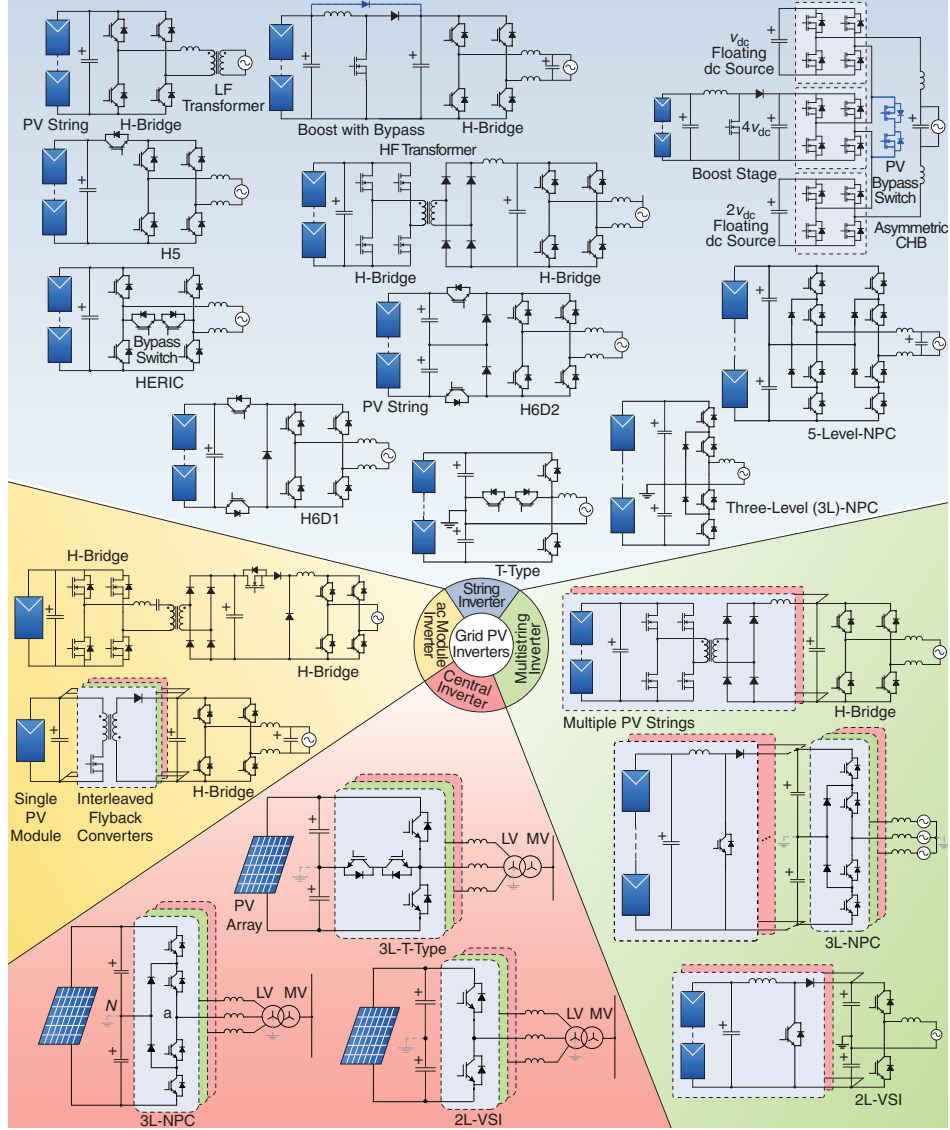


Figure 1.3: Power converters used by different PV configuration systems. (source [10])

### 1.3.4 Central Topology

Finally, the central inverter interfaces a whole PV array to the grid via a single inverter (Fig. 1.2). A blocking diode in series to each string is necessary to prevent them from acting as a load when partial shading or mismatch occurs. Because the whole array is connected to a single inverter, this configuration can only provide a single MPPT operation, leading to the lowest MPPT efficiency of all configurations. Nevertheless, it provides a simple structure with an efficient converter, making it one of the most common solutions for large-scale PV plants.

This centralized inverter includes some severe limitations such as high voltage DC cables between the PV modules and the inverter, power losses due to a centralized MPPT, mismatch losses between the PV modules, losses in the string diodes, and a non-flexible design where the benefits of mass production cannot be reached.

## 1.4 Motivation

Unlike conventional PV system topologies such as string, multistring and central inverters where the power converters are typically located indoors, the electronics in PV microinverters will reside in the same environment as the PV module, which exposes them to harsher and more variable operating conditions (temperatures from  $-30^{\circ}\text{C}$  to  $+70^{\circ}\text{C}$  and humidity levels from 0% to 100% combined with salty and corrosive conditions [18]). This means that guaranteeing higher reliability becomes a more imperative task when compared to the other topologies [19].

Since PV microinverters are typically attached to the back of the PV modules, and may well be integrated to the PV module back skin, it is desirable that the microinverter has a lifetime that matches the PV module one, which for the vast majority of manufactures is around 25 years.

It is well known that in single-phase ( $1\phi$ ) inverters there is a need to decouple the input from the output of the inverter since the DC source at the input (i.e. the PV generator) delivers a constant power, while the AC output leads to a time fluctuating instantaneous power with double the grid frequency. The decoupling circuit is normally composed by a large capacitance (DC-link capacitor) that acts as a buffer which delivers or receives the difference in instantaneous power [20].

Typically electrolytic capacitors are used as the decoupling element due to their good capacitance per volume ratio and low price. The use of electrolytic capacitors makes it is easy and affordable to install very high capacitances for decoupling between input and output of the  $1\phi$  inverter. This comes with a price, a severe drawback of this type of capacitor is its limited lifetime.

Electrolytics are affected by ageing effects more than other electronic components and are therefore a bottleneck for inverter reliability and lifetime. Disadvantages include low ripple current capability due to high equivalent series resistance (ESR) and equivalent series inductance (ESL), high thermal resistances limiting the ability to get the heat out, clumsy packaging sizes and mounting difficulties, weight and temperature range. Another characteristic is that over time the liquid of electrolyte evaporates through the rubber seals of the capacitor, degrading the capacitance [20]. This effect can be compensated by over sizing the capacitors by design, but a limit in lifetime will still exist. Electrolytic capacitor technology has also remained virtually unchanged over the years.

Many efforts have been made towards replacing electrolytic capacitors by film capacitors (metallized polyester or polypropylene films), due to this type having a much higher lifetime and can even be self-healing in case of minor isolation breakdowns. The disadvantage of film capacitors is a low capacitance per volume ratio (approximately 20 times lower than for electrolytics) and a much higher price. A direct replacement is therefore not feasible in terms of cost and size [20].

Numerous microinverters have been proposed each using different types of decoupling circuits in an attempt to lower values of needed capacitance and therefore enabling the use of film capacitors. Many of these topologies that use film capacitors were designed for the previous generation of PV modules that had output powers between 100 W and 150 W [17]. The current average PV module output power is around 270 W which leads to many previous microinverter topologies that used film capacitors no longer being adequate since the needed capacitance not being small enough.

## 1.5 Thesis Objective

The main purpose of this thesis is to design a PV microinverter for current power PV modules (270 W), isolated by a high frequency transformer which can be used by private householders. Other goals include:

- The power converter should not contain any electrolytic capacitors in order to increase expected lifetime.
- Design and compare through numerical simulation a linear and nonlinear control of the system to obtain the best possible performance of the proposed microinverter.

To verify the correctness of the design a numerical computing environment such as MATLAB/Simulink will be used.

## 1.6 Thesis Outline

This dissertation is composed by the following four parts:

- It begins by briefly introducing PV system configurations in **Chapter 1**. This is followed, in **Chapter 2** by an overview of the principle decoupling techniques in order to understand the role of electrolytic capacitors in PV microinverters (in order to achieve the first goal). While **Chapter 3** presents the main principles behind nonlinear control (Lyapunov method) while presenting design procedures (in order to achieve the second goal).
- In **Chapter 4** the mathematical model representation of PV modules is preformed which is then subsequently adapted and implemented in a Simulink environment. The proposed microinverter is introduced in **Chapter 5**, followed by the design of its high frequency transformer, active and passive components, which will then be used to choose suitable real world existing components.
- The maximum power point tracking controller is designed in **Chapter 6**, while the control of the voltage at the DC-link is performed in **Chapter 7**. Each control system is designed with both traditional controllers (such as PI compensators and nonlinear hysteresis band control) and new (or less common) nonlinear controllers (such as backstepping and command filtering backstepping control techniques).
- Finally, in **Chapter 8** the proposed power converter and the designed controllers are evaluated under various simulation scenarios to prove the correct operation of the system and choose the best control system. In **Chapter 9** some final remarks are made on the power converter overall performance and suggestions for further issues that were not covered in this dissertation.

## Chapter 2

# Power Decoupling Techniques

As explained in Chapter 1, single-phase grid connected inverters typically use an electrolytic capacitor of large capacitance in order to decouple the power pulsation caused by the  $1\phi$  utility line. Innovative power decoupling circuits can reduce the size of the required energy storage capacitor, thus improving the inverter lifetime, which is a much desired feature for AC-modules.

However, the power decoupling circuit will also result in additional power losses, due to the power flow through the decoupling circuit, consequently, reducing the overall efficiency [21]. Although the power decoupling circuit may increase the total system cost due to the additional circuitry required, the extended lifetime eliminates the then otherwise reoccurring cost of inverter maintenance or replacement that would haunt the PV system return on investment [22].

The goal of this chapter is to give an overview of the different power decoupling techniques in order to choose a suitable topology to obtain small decoupling capacitance while guaranteeing high efficiency. The two main power decoupling techniques are displayed in Figure 2.1, while some authors [22] and [21], consider a third technique where the decoupling capacitor is usually embedded in the grid inverter stage itself. Figure 2.2 shows the ranges of capacitance per technology.

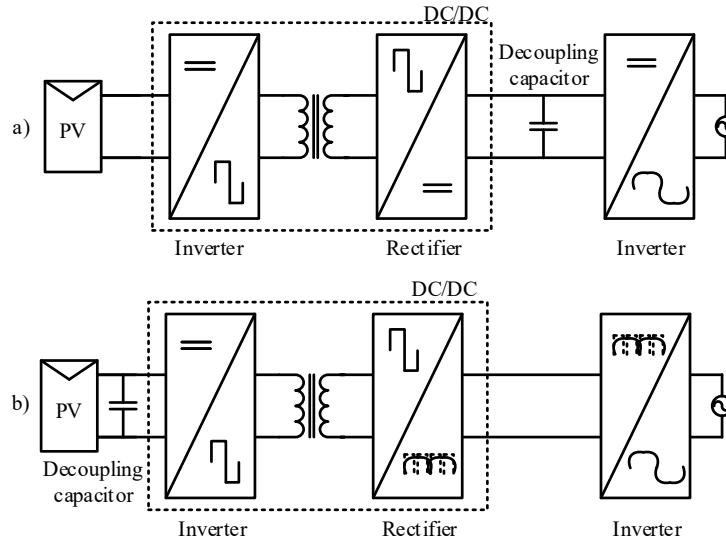


Figure 2.1: a) DC-Link Decoupling and b) PV-Side Decoupling.

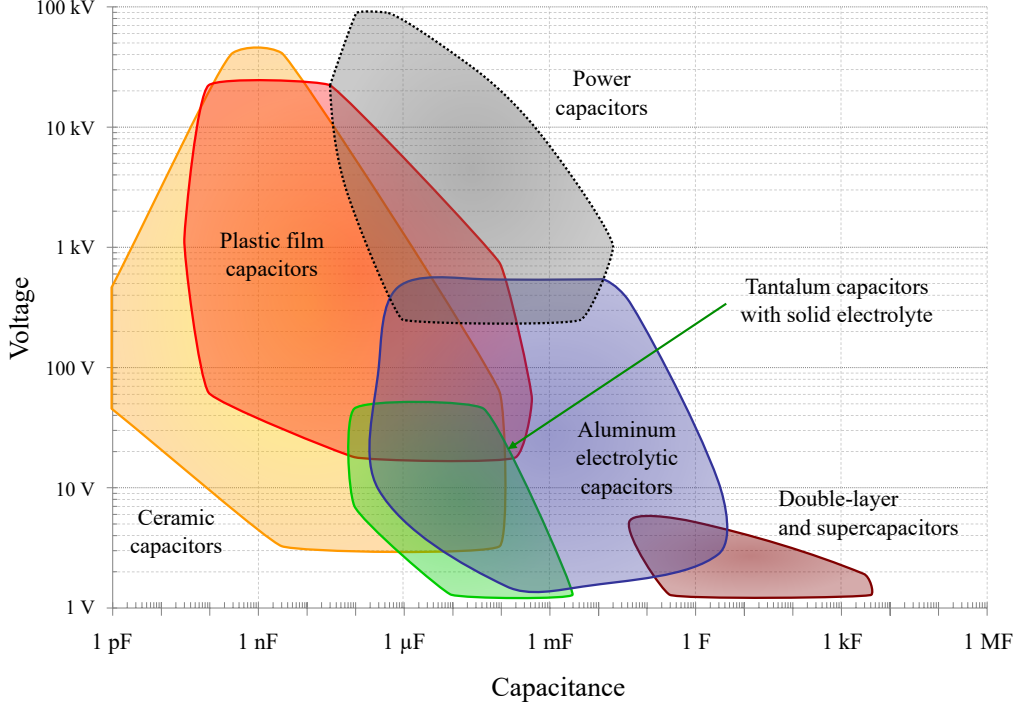


Figure 2.2: Capacitance/voltage ranges for each capacitor technology.

## 2.1 PV-Side Decoupling

PV-side decoupling (also known as pseudo DC-link configuration) is the designation used to describe microinverters that have the decoupling reactive element on the primary side of the transformer, Figure 2.1. This configuration is considered a single-stage converter since there is no intermediate energy storage on the secondary side of the transformer.

The primary side of the converter is responsible for guaranteeing MPPT of the PV module, increasing the voltage via a step-up transformer (and a boost inductor if present) and generating a rectified sine waveform using a high frequency modulation technique.

The secondary side of the converter is responsible for the unfolding of the high-frequency sine waveform from the primary side via an inverter which uses a line frequency commutation. Since the output inverter has a low frequency commutation, the switching losses are decreased, which is one of the benefits of this microinverter decoupling topology.

One of the main drawbacks of PV-side decoupling is the low power density ( $W/m^3$ ) of the decoupling capacitor. This can be explained by the following two reasons:

- The power capacitor across the PV module terminals results in a very large capacitor since the allowable voltage ripple must be kept to very low values ( $< 1\%$ ) in order to achieve high MPPT efficiency [22].
- The high current present in the primary side of the step-up transformer means that a higher capacitance value is needed due to the capacitance being proportional to its current, equation (5.31).

A typical case of a microinverter which utilizes a large capacitance is illustrated in Figure 2.3 a). The solution used to reduce the size of the capacitor at the terminals of the PV module is the addition of an extra decoupling circuit as shown in Figure 2.3 b).

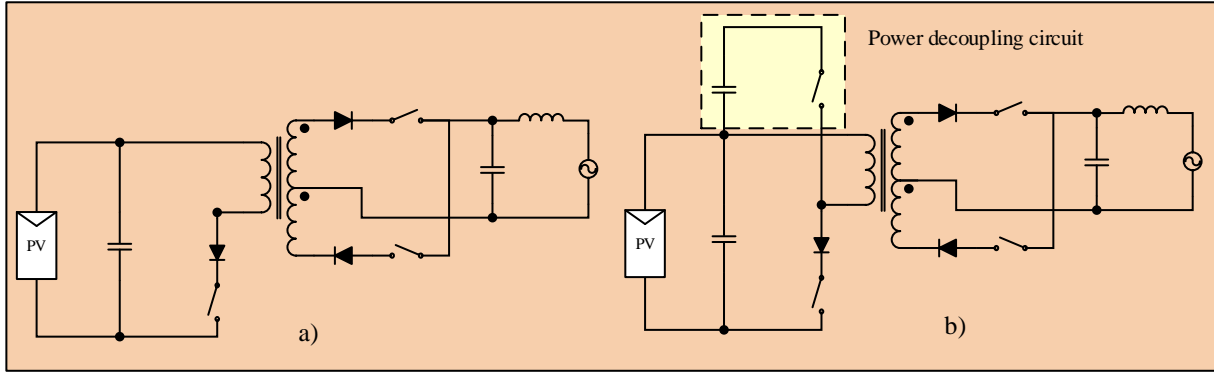


Figure 2.3: a) Single-transistor flyback-type HF-link inverter and b) Flyback-type inverter with high-power decoupling [17].

Many solutions which use different power decoupling circuits have been proposed [21][22], but they all use the same principle shown in 2.3 b) and explained in [23] (Fig. 2.4).

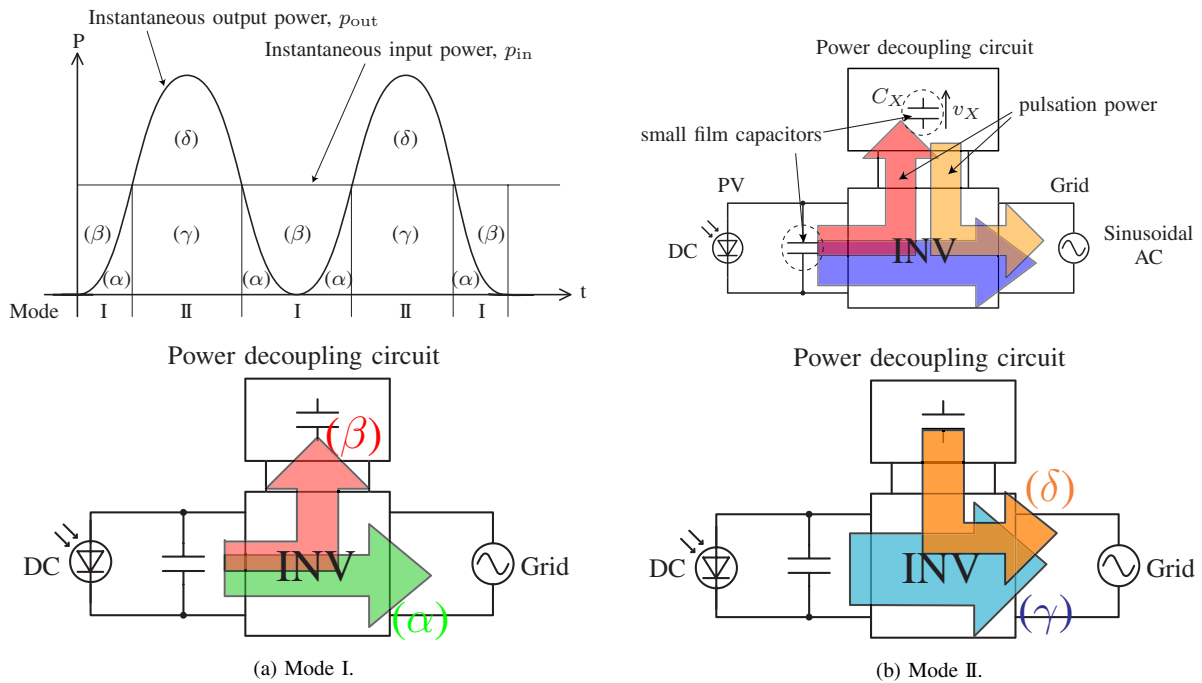


Figure 2.4: Active power decoupling control modes. (source [23])

## 2.2 DC-Link Decoupling

The DC-link decoupling topology is considered a multi-stage converter typically with a DC-AC-DC-AC configuration, while the power conversion process can be divided into two separate stages: DC-DC and DC-AC conversions. For this multi-stage converter the main power decoupling capacitor is placed at the high voltage secondary side, as shown in Figure 2.1 b).

The primary side of the transformer, or DC-DC converter, is responsible for guaranteeing MPPT, amplifying the PV DC voltage to a sufficient voltage level compatible with the grid maximum voltage while simultaneously providing galvanic isolation. Any isolated DC-DC converter can be a candidate to the this power conversion stage [22]. Isolated DC-DC converters can be classified as:

- *Hard-switching*: Less active/reactive components are needed, but switching losses tend to be high due to the leakage inductance (of the transformer) being opened while its current is not equal to zero and/or by connecting it in series with other elements equivalent to current sources.
- *Soft-switching*: Extra circuitry elements are added which implement zero-voltage switching (ZVS), zero-current switching (ZCS), or active clamp techniques to improve the efficiency and overcome problems caused by the leakage inductance.

The DC-link capacitance has a higher power density ( $W/m^3$ ) when compared to the pseudo DC-link topology due to the following two reasons:

- The lower current at the DC-link (when compared to the PV-side of the transformer) reduces the required decoupling capacitance as shown in equation (5.31) that is deduced in subchapter 5.3.1.
- Higher voltage ripple is allowed at this decoupling element since it is not responsible for guaranteeing MPPT, with the constraint that the lowest DC-link voltage should be greater than or equal to the peak grid voltage, as illustrated in Figure 2.5.

Compared to the PV-side decoupling, the DC-link decoupling does not need no additional circuitry to perform the decoupling of the system.

As stated before, any isolated DC-DC converter can be used to perform the MPPT. A solution to increase the reliability of the AC-module can pass by using an isolated current-fed DC-DC power converter since inductors have a much longer lifetime when compared to capacitors [19].

### 2.2.1 Isolated Current-Fed DC-DC Topologies

Isolated current source DC-DC topologies decrease the turn ratio of the transformer since the primary voltage of the transformer is larger than the PV module output, due to the boost inductor. This leads to copper losses and leakage of transformer elements being reduced.

In Figure 2.6 four different soft-switching isolated current-fed converters are displayed. The main principles of soft-switching techniques are briefly discussed below [25]:

- *ZVS techniques*: A ZVS turn-on is achieved by forcing current through the body-diode of the semiconductors, just before they are turned on. This clamps the voltage across the device to a

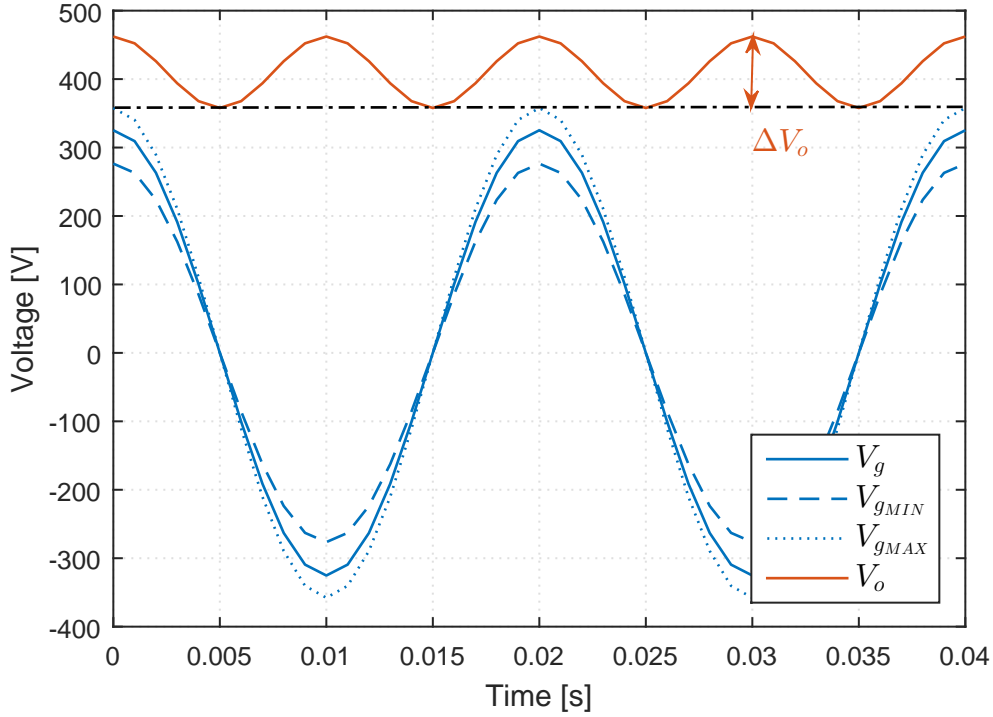


Figure 2.5: Maximum allowed voltage ripple at the DC-link capacitor(s) in order for the voltage source inverter (VSI) to have a correct behaviour.

single diode drop (negligible voltage) during a switching transition so that turn-on switching losses are greatly reduced. A ZVS turn-off is achieved by slowing down the rate of voltage rise across a switch when it is turned off by adding some capacitance across the switch, limiting the overlap between voltage and current during the switching transition.

- *ZCS techniques*: are techniques that force the current through a switch to be zero when the switch is about to turn on or off and keep this current zero while a switching transition occurs. A ZCS turn-off is achieved by diverting current away from the switch into the rest of the power converter just before the switch is turned off. This is typically done by providing a path of negative voltage potential to the switch or by imposing a negative voltage somewhere in the current path. A ZCS turn-on can be done by adding an inductor.
- *Active-clamp*: The clamp capacitor clamps the voltage that appears across the full-bridge whenever full-bridge switches are turned off and is allowed to discharge into the full-bridge converter whenever a pair of diagonally opposed switches is on. The additional switch is always off whenever the converter is in a current boosting mode to avoid it being short-circuited. The term "active clamp" refers to the fact that the DC bus capacitor acts as a clamp and is in series with an active switch.
- *Resonant Tank*: resonant inductor-capacitor (LC) networks have voltage and current waveforms that vary sinusoidally during one or more subintervals of each switching period. By inserting a the LC network in parallel with full-bridge switches, the voltage across the switches can be shaped so that they are able to turn on and off with ZVS.

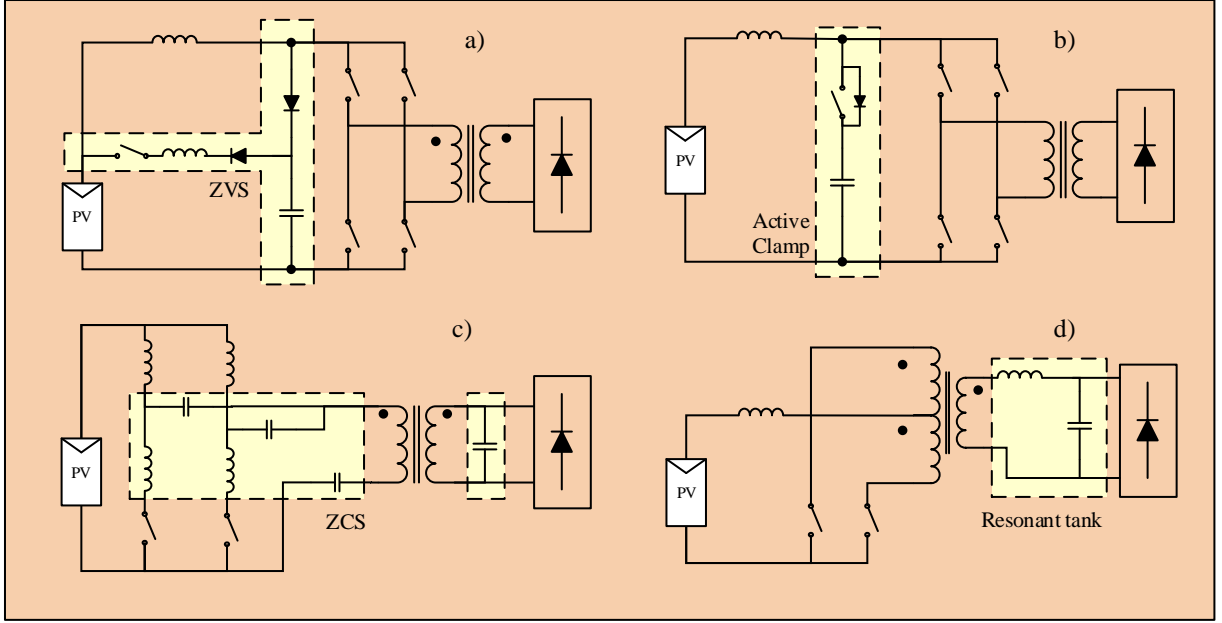


Figure 2.6: Isolated current-fed DC-DC topologies: a) ZVS-PWM Full-Bridge Boost Converter [25] b) Active-clamp Full-Bridge Boost Converter [26] c) Current-Fed ZCS High Frequency Inverter-applied Resonant DC-DC Converter for Inductive Power Transfer [27] and d) Soft-Switching Current-Fed Push-Pull Converter [28].

Component count (for soft-switching), the control strategies and major disadvantage of each of the different current-fed isolated DC-DC converters of Figure 2.6 are listed in the Table 2.1 below. Analysing Table 2.1, topology b) is chosen (and studied in Chapter 5) due to it combining a low component count with an easy control system, both criteria which reduce the overall cost of the microinverter.

Table 2.1: Comparasson of different isolated current-fed DC-DC topologies.

	Fig.2.6 a)	Fig.2.6 b)	Fig.2.6 c)	Fig.2.6 d)
Extra Components	Medium	Low	High	Very Low
Control Strategy	PWM control	PWM control	Current phasor control	PWM control
Major Disadvantage	Complex components design	High current through full-bridge	Efficiency highly load dependent	Variable switching frequency

## Chapter 3

# Nonlinear Lyapunov Control

Physical systems are commonly treated as linear approximations of more complex nonlinear systems. To control, nonlinear systems, the application of linear control techniques is possible, but may lead to limitations in terms of performance and operation span. The account of nonlinearities by a control design allows for an expansion of the operating region [37]. The Russian mathematician Aleksandr Lyapunov deduced some of the most useful tools for stability analysis. Listed below is a summary of the main concepts of Lyapunov's stability theory. A more extensive description than the one listed below of Lyapunov stability concepts can be found in [37].

### 3.1 Lyapunov Stability

Consider the nonlinear non-autonomous<sup>1</sup> system

$$\dot{\underline{x}} = f(\underline{x}, t) \quad (3.1)$$

where the state vector  $\underline{x} \in \mathbb{R}^n$  and the nonlinear function  $f : \mathbb{R}^n \times \mathbb{R}^+ \rightarrow \mathbb{R}^n$  is locally Lipschitz continuous in  $\underline{x}$  and piecewise continuous in  $t$ . Let  $\underline{x}_e$  be an equilibrium point of (3.1),  $f(\underline{x}_e, t) = 0$ ,  $\forall t \geq 0$ , and, for simplicity, suppose that  $\underline{x}_e$  is the origin of  $\mathbb{R}^n$ .

In the sense of Lyapunov, *stability* means that all trajectories starting close enough to the origin (equilibrium point) will remain near the origin ( $\|\underline{x}(t)\| < \epsilon$ ), that is, in the vicinity of that equilibrium state (Fig. 3.1).

**stable** if, for each  $\epsilon > 0$  and  $t_0 \geq 0$ , there is  $\delta(\epsilon, t_0) > 0$  such that

$$\|\underline{x}(t_0)\| < \delta(\epsilon, t_0) \quad \Rightarrow \quad \|\underline{x}(t)\| < \epsilon, \quad \forall t \geq t_0;$$

**unstable** if it is not stable;

**attractive** if, for each  $\epsilon > 0$  and  $t_0 \geq 0$ , there is both  $\delta(t_0) > 0$  and  $T(\epsilon, t_0)$  such that

$$\|\underline{x}(t_0)\| < \delta(t_0) \quad \Rightarrow \quad \|\underline{x}(t)\| < \epsilon, \quad \forall t \geq t_0 + T;$$

*Asymptotic stability* is a more strict property, since it requires that the system converges to the equilibrium state from which it was disturbed as  $t \rightarrow \infty$ .

---

<sup>1</sup>non-autonomous: The vector field of the system depends explicitly on time [42].

**asymptotically stable** if it is stable and, for  $t_0 \geq 0$ , there exists a  $\delta(t_0) > 0$  such that

$$\|\underline{x}(t_0)\| < \delta(t_0) \quad \Rightarrow \quad \lim_{t \rightarrow \infty} \underline{x}(t) = 0;$$

If the constraint  $\delta$  on the initial state does not depend on the initial time  $t_0$  then the equilibrium point is said to have *uniform stability*.

**uniformly stable** if the stability condition is independent of  $t_0$ , i.e., for any  $t_0 \geq 0$  and  $\epsilon > 0$ , there is a  $\delta(\epsilon) > 0$  such that

$$\|\underline{x}(t_0)\| < \delta \quad \Rightarrow \quad \|\underline{x}(t)\| < \epsilon, \quad \forall t \geq t_0;$$

If, added to this, the states converge to the initial equilibrium state, then it is *uniformly asymptotically stable*.

**uniformly asymptotically stable** if the asymptotic stability condition is independent of the initial time  $t_0$ , i.e., there is a  $\delta > 0$  for all  $t_0 \geq 0$  such that

$$\|\underline{x}(t_0)\| < \delta \quad \Rightarrow \quad \lim_{t \rightarrow \infty} \underline{x}(t) = 0;$$

The rate of this convergence can be exponential, making it an *exponentially stable* equilibrium

**exponentially stable** if, for  $\epsilon > 0$ , there exists a pair  $\delta(\epsilon) > 0$  and  $\lambda > 0$  that satisfies

$$\|\underline{x}(t_0)\| < \delta(\epsilon) \quad \Rightarrow \quad \|\underline{x}(t)\| < \epsilon e^{-\lambda(t-t_0)}, \quad \forall t \geq t_0 \geq 0.$$

It should be noted that, contrarily to linear systems, that have only one equilibrium state, nonlinear systems can have several, making no sense to talk about stability of the system. Instead stability is defined for each equilibrium point.

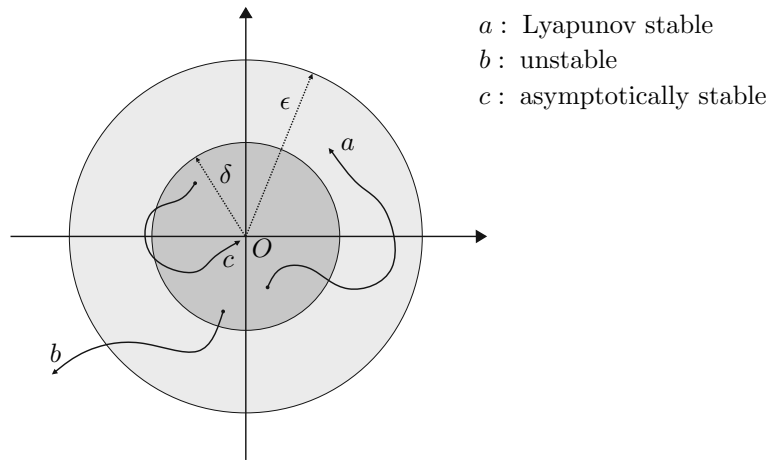


Figure 3.1: Lyapunov stability in  $\mathbb{R}^2$ . (source [37])

## 3.2 Lyapunov's Second Method

The minima of the potential energy function of a conservative system is a stable equilibrium point and its maxima is an unstable equilibrium (Lagrange). Lyapunov's second method (or direct method) is a mathematical extension of the fundamental physics principle: the total mechanical energy of a system is continuously dissipated until it reaches an equilibrium point.

Lyapunov generalized this idea for stability analysis. He did so by introducing a scalar function that has similar properties to the ones of an energy function. Consider an appropriate function  $V(\underline{x}, t)$  (the Lyapunov function) and its time derivative along the trajectories of (3.1), which is:

$$\dot{V}(\underline{x}, t) \Big|_{\dot{\underline{x}}=f(\underline{x}, t)} = \frac{\partial V}{\partial t} + \frac{\partial V}{\partial \underline{x}} f(\underline{x}, t) \quad (3.2)$$

**Theorem 3.2.1** (Lyapunov's Second Method). Let  $V(\underline{x}, t) : \mathbb{R}^+ \times D \rightarrow \mathbb{R}^+$  be a continuously differentiable and positive definite function, where  $D$  is an open region containing the origin. The equilibrium  $x_e = 0$  is:

**stable** if  $\dot{V}(\underline{x}, t) \Big|_{\dot{\underline{x}}=f(\underline{x}, t)}$  is negative semi-definite for  $\underline{x} \in D$ ;

**uniformly stable** if  $V(\underline{x}, t)$  is decrescent and  $\dot{V}(\underline{x}, t) \Big|_{\dot{\underline{x}}=f(\underline{x}, t)}$  is negative semi-definite for  $\underline{x} \in D$ ;

**asymptotically stable** if  $\dot{V}(\underline{x}, t) \Big|_{\dot{\underline{x}}=f(\underline{x}, t)}$  is negative for  $\underline{x} \in D$ ;

**uniformly asymptotically stable** if  $V(\underline{x}, t)$  is decrescent and  $\dot{V}(\underline{x}, t) \Big|_{\dot{\underline{x}}=f(\underline{x}, t)}$  is negative definite  $\underline{x} \in D$ ;

**exponentially stable** if there exist constants  $c_1, c_2$  and  $c_3$  such that

$$c_1 |\underline{x}|^2 \leq V(\underline{x}, t) \leq c_2 |\underline{x}|^2 \quad \text{and} \quad \dot{V}(\underline{x}, t) \Big|_{\dot{\underline{x}}=f(\underline{x}, t)} \leq -c_3 |\underline{x}|^2, \quad \forall t \geq 0, \underline{x} \in D.$$

### 3.2.1 Control Lyapunov Functions

The tools presented in this subsection 3.2 are mainly directed towards the stability analysis of a system. In this section it will be shown how to use them to design a closed-loop system with the desired stability properties. To this end consider the nonlinear time-invariant system

$$\dot{\underline{x}} = f(\underline{x}, u), \quad \underline{x} \in \mathbb{R}, \quad u \in \mathbb{R}, \quad f(0, 0) = 0 \quad (3.3)$$

for which a feedback law  $\alpha(\underline{x})$  for the input  $u$  is to be designed. The goal is to make the equilibrium point  $\underline{x} = 0$  globally asymptotically stable. For this to be achieved a Lyapunov function  $V(\underline{x})$  must be defined that has a negative definite time derivative along (3.3), as exemplified in Figure 3.2.

**Definition 3.2.1** (Control Lyapunov function). A smooth positive definite and radially unbounded function  $V(\underline{x}) : \mathbb{R}^n \rightarrow \mathbb{R}^+$  is called a control Lyapunov function (CLF) for (3.3) if:

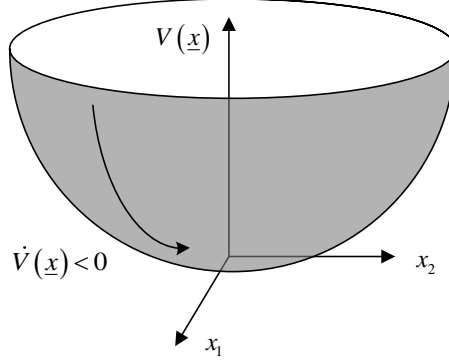


Figure 3.2: Example of a positive definite Lyapunov function with  $\underline{x} \in \mathbb{R}^2$ .

$$\inf_{u \in \mathbb{R}} \left\{ \frac{\partial V}{\partial \underline{x}}(\underline{x}) f(\underline{x}, u) \right\} < 0, \quad \forall \underline{x} \neq 0$$

The existence of a CLF proves asymptotic stability, since it is sufficient condition for the existence of a feedback law  $\alpha(\underline{x})$  that satisfies (LaSalle-Yoshizawa Theorem):

$$\frac{\partial V}{\partial \underline{x}}(\underline{x}) f(\underline{x}, \alpha(\underline{x})) \leq -W(\underline{x}) < 0, \quad \forall \underline{x} \in \mathbb{R}^n. \quad (3.4)$$

where if  $W(\underline{x})$  is a positive definite continuous function, then the equilibrium  $\underline{x}_e = 0$  is globally uniformly asymptotically stable.

### 3.2.2 Backstepping Design

The backstepping technique is as a recursive Lyapunov method for the design of controllers for nonlinear systems. The name “backstepping” derives from the fact that, during the procedure, the designer “steps back” from the scalar equation ( $\dot{x}_1$ ) that is the furthest (number-of-integrations-wise) from the control input ( $u$ ) towards this same control input in a recursive manner.

$$\left\{ \begin{array}{l} \dot{x}_n = f_n(x_1, x_2, \dots, x_{n-1}, x_n) + g_n(x_1, x_2, \dots, x_{n-1}, x_n)(u) \\ \left\{ \begin{array}{l} \dot{x}_{n-2} = f_{n-2}(x_1, x_2, \dots, x_{n-3}, x_{n-2}) + g_{n-2}(x_1, x_2, \dots, x_{n-3}, x_{n-2})(x_n) \\ \vdots \\ \dot{x}_2 = f_2(x_1, x_2) + g_2(x_1, x_2)(x_3) \\ \left\{ \begin{array}{l} \dot{x}_1 = f_1(x_1) + g_1(x_1)(x_2) \\ \alpha_0 = y_r \\ \dot{z}_1 = \dot{x}_1 - \dot{\alpha}_0 \\ \dot{z}_2 = \dot{x}_2 - \dot{\alpha}_1 \\ \vdots \\ \dot{z}_{n-1} = \dot{x}_{n-1} - \dot{\alpha}_{n-2} \end{array} \right. \\ \dot{z}_n = u \end{array} \right. \end{array} \right. \quad (3.5)$$

The backstepping design can be extended to arbitrarily higher order systems in strict-feedback

form. Such a system of  $n^{th}$  order is:

$$\begin{aligned}\dot{x}_1 &= f_1(x_1) + g_1(x_1)x_2 \\ \dot{x}_2 &= f_2(x_1, x_2) + g_2(x_1, x_2)x_3 \\ &\vdots \\ \dot{x}_n &= f_n(x_1, x_2, \dots, x_{n-1}, x_n) + g_n(x_1, x_2, \dots, x_{n-1}, x_n)u\end{aligned}\tag{3.6}$$

with  $(x_1, \dots, x_n, u) \in \mathbb{R}^{n+1}$  and  $g_i \neq 0, \forall i \in \{1, 2, \dots, n\}$ .

The objective is to make  $x_1$  asymptotically track a smooth waveform  $y_r$ . The process starts by defining the tracking error coordinates:

$$z_i = x_i - \alpha_{i-1}, \quad i \in \{1, 2, \dots, n\}\tag{3.7}$$

where  $\alpha_0 = y_r$  (is the reference). With the change of coordinates (3.7) it is now possible to build a positive quadratic control Lyapunov function<sup>2</sup> of  $z_i$  recursively to each design step as:

$$V_i(z_1, z_2, \dots, z_{i-1}, z_i) = V_{i-1}(z_1, z_2, \dots, z_{i-1}) + \frac{1}{2}z_i^2\tag{3.8}$$

The time derivatives of (3.8) is given by:

$$\dot{V}(z_1, z_2, \dots, z_{i-1}, z_i) = \dot{V}_{i-1}(z_1, z_2, \dots, z_{i-1}) + z_i \dot{z}_i\tag{3.9}$$

where the dynamics of the error coordinates is:

$$\dot{z}_i = \dot{x}_i - \dot{\alpha}_{i-1} = (f_i + g_i x_{i+1}) - \dot{\alpha}_{i-1} = [f_i + g_i (z_{i+1} + \alpha_{i+1})] - \dot{\alpha}_{i-1}\tag{3.10}$$

with  $x_{n+1} = u$ . The application of LaSalle-Yoshizawa Theorem (3.4) results in stabilizing virtual controls  $\alpha_j$  and control input  $u$  given, for example, by:

$$\begin{aligned}\alpha_1 &= \frac{1}{g_1}(-c_1 z_1 - f_1 + \dot{y}_r), \quad c_1 > 0 \\ \alpha_j &= \frac{1}{g_j}(-c_j z_j - f_j - g_{j-1} z_{j-1} + \dot{\alpha}_{j-1}), \quad c_j > 0, \quad j \in \{2, 3, \dots, n-1\} \\ u &= \frac{1}{g_n}(-c_n z_n - f_n - g_{n-1} z_{n-1} + \dot{\alpha}_{n-1}), \quad c_n > 0\end{aligned}\tag{3.11}$$

If the system (3.6) is feedback with the control inputs (3.11) asymptotic tracking of  $y_r$  by  $x_1$  is achieved.

---

<sup>2</sup>Lyapunov functions - Although very often the control Lyapunov functions are chosen to have a quadratic form, similar to the ones used in this derivation, it is possible, and sometimes even beneficial, to use different forms that, for example, to avoid the cancellation of stable nonlinearities.

### 3.2.3 Command Filtering Backstepping

In the previous subsection the Backstepping design was explained for any strict-feedback system of any order. Although the design seems simple, the increase in order dramatically complicates the computation of the time-derivative of the virtual control laws ( $\dot{\alpha}_i$ ). This calculation can be brought down to a differentiation by filtering using a command filter [38],[39] as shown in Figure 3.3.

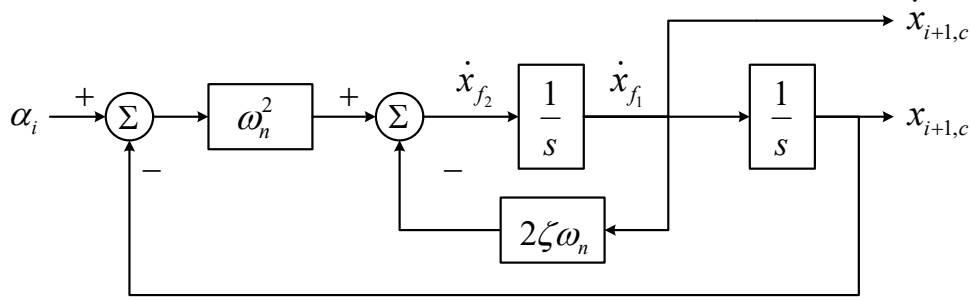


Figure 3.3: Command filter (CF) block diagram [37],[38].

where  $\zeta$  and  $\omega_n$  are, respectively, the damping coefficient  $\in ]0 ; 1]$  and the fixed natural frequency of the filter. Analysing Figure 3.3 it can be shown that the signal  $\dot{x}_{i+1,c}$  is obtained by using integral method rather than a differential method which attenuates the high frequency disturbances [44]. The CF shown in Figure 3.3 has the following state-space representation:

$$\begin{bmatrix} \dot{x}_{f1} \\ \dot{x}_{f2} \end{bmatrix} = \begin{bmatrix} 0 & 1 \\ -\omega_n^2 & -2\zeta\omega_n \end{bmatrix} \begin{bmatrix} x_{f1} \\ x_{f2} \end{bmatrix} + \begin{bmatrix} 0 \\ \omega_n^2 \end{bmatrix} \alpha_i \quad (3.12)$$

where  $\alpha_i$  is the filter input signal and  $x_{f1}$ ,  $x_{f2}$  are filter states.

$$\begin{bmatrix} x_{i+1,c} \\ \dot{x}_{i+1,c} \end{bmatrix} = \begin{bmatrix} 1 & 0 \\ 0 & 1 \end{bmatrix} \begin{bmatrix} x_{f1} \\ x_{f2} \end{bmatrix} \quad (3.13)$$

The CF transfer function is given by:

$$\begin{bmatrix} x_{f1} \\ x_{f2} \end{bmatrix} = \frac{\omega_n^2}{s^2 + 2\zeta\omega_n s + \omega_n^2} \begin{bmatrix} 1 \\ s \end{bmatrix} \alpha_i \quad (3.14)$$

which has a DC unit gain for the first output, whereas the second output is the derivative of the first output. The CF should be implemented with a finite natural frequency not necessarily much greater than that of the natural frequency of the input [43], in order that  $x_{i+1,c}$  and  $\dot{x}_{i+1,c}$  accurately track  $\alpha_i$  and  $\dot{\alpha}_i$ , the range of  $c_i$  gains is restricted to be:

$$c_i \leq \omega_n \quad (3.15)$$

The signal flow in block diagram form for the command filtering backstepping approach (CFBS) can be found in Figure 3.4, where the feedback control signals (3.11) are not directly applied, instead these signals are corrected by the CF resulting in  $x_{i+1,c} \equiv \alpha_i$  and  $\dot{x}_{i+1,c} \equiv \dot{\alpha}_i$ .

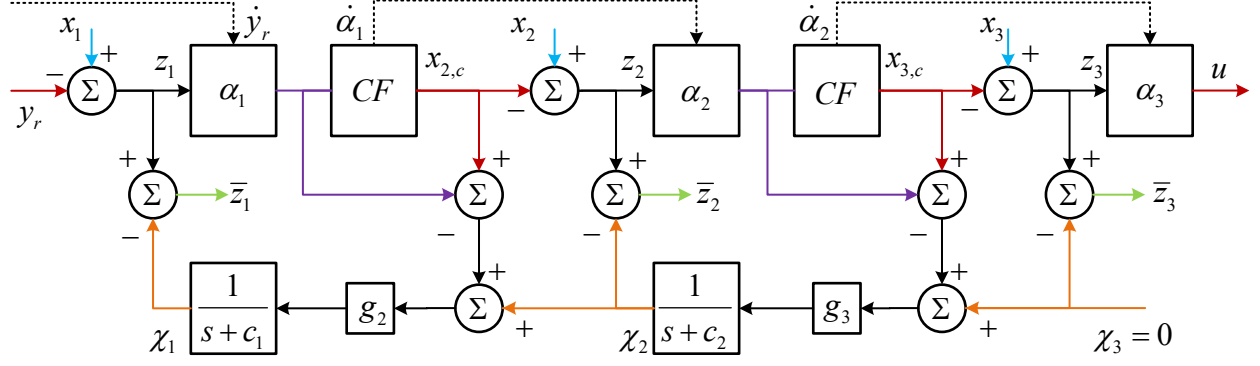


Figure 3.4: Block diagram of the CFBS approach for  $n = 3$ . The virtual controls  $\alpha_i$  are computed according to (3.11). The dotted lines from the CF to the  $\alpha_i$  represent the communication of the command derivative  $\dot{\alpha}_i$  from the CF to the computation of  $\alpha_{i+1}$  [38]. Colours have been added to highlight the pattern of repetitiveness in the construction.

The variables  $\bar{z}_i$  are referred as compensated tracking errors because they are obtained by removing the filtered unachieved portion of  $\alpha_i$ , represented by  $\chi_i$ , from the tracking error.

$$\bar{z}_i = z_i - \chi_i, \quad i = 1, 2, \dots, n \quad (3.16)$$

Which leads to the following stabilizing virtual controls  $\alpha_j$  and control input  $u$ :

$$\begin{aligned} \alpha_1 &= \frac{1}{g_1}(-c_1 z_1 - f_1 + \dot{y}_r), \quad c_1 > 0 \\ \alpha_j &= \frac{1}{g_j}(-c_j z_j - f_j - g_{j-1} \bar{z}_{j-1} + \dot{\alpha}_{j-1}), \quad c_j > 0, \quad j \in \{2, 3, \dots, n-1\} \\ u &= \frac{1}{g_n}(-c_n z_n - f_n - g_{n-1} \bar{z}_{n-1} + \dot{\alpha}_{n-1}), \quad c_n > 0 \end{aligned} \quad (3.17)$$

The control input  $u$  obtained by a CFBS approach for  $n = 2$  (for example) is given by:

$$u = \frac{1}{g_2} [-c_2 z_2 - f_2 - g_1 \bar{z}_1 - \dot{x}_{c,2}] \quad (3.18)$$

The complete stability proof of CFBS approach can be found in [39].

## Chapter 4

# PV-Module

### 4.1 Mathematical Model

Since the output current  $I$  and voltage  $V$  of PV modules change not only with the output load, but also change under varying atmospheric conditions, to correctly study the proposed power converter it is mandatory to utilize a mathematical model that simulates the behaviour of a real PV module. The three models that are typically used to represent PV cells [11] are listed below in ascending order of accuracy:

- One-Diode Model (three parameters) - Includes voltage and current relation.
- One-Diode Model (five parameters) - Includes voltage drop and leakage current.
- Two-Diode Model (seven parameters) - Includes the effect of recombination.

The One-Diode model, five parameters, is a good choice that combines both accuracy and some level of simplicity, while its equivalent circuit is shown in figure 4.1.

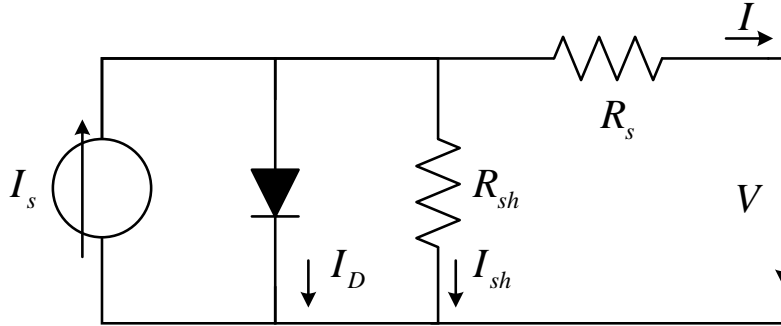


Figure 4.1: Equivalent electrical circuit of a PV cell (One-Diode, five parameters model).

The current source  $I_s$  represents the electrical current generated by the PV cell when exposed to a certain irradiance  $G$ , while the diode represents the p-n junction and its internal current  $I_D$  which depends on the output voltage. The additional accuracy of the One-Diode five parameter model compared to the three parameter model is due to the inclusion of losses represented by the resistances  $R_s$  and  $R_{sh}$ . The series resistance represents the voltage drop between the semiconductor and the external contacts while the parallel (shunt) resistance represents existing leakage currents.

Applying Kirchhoff's current law to the equivalent circuit of the PV cell, figure 4.1, the output current  $I$  is obtained:

$$\begin{aligned} I &= I_S - I_D - I_{sh} \\ I &= I_S - I_0 \left[ \exp \left( \frac{V + R_s I}{m V_T} \right) - 1 \right] - \frac{V + R_s I}{R_{sh}} \end{aligned} \quad (4.1)$$

where:

- $I_0$  - diode saturation current [A];
- $m$  - ideality factor of the diode (ideal diode:  $m = 1$ ; real diode:  $m > 1$ );
- $V_T$  - thermal voltage equivalent [V];

$$V_T = \frac{K T_c}{q} \quad (4.2)$$

$K$ : Boltzmann constant ( $K = 1,38 \times 10^{-23}$  [J/K]);

$T_c$ : absolute cell temperature [K];

$q$ : electron charge ( $q = 1,6 \times 10^{-19}$  [C]);

- $V$  - PV cell output voltage [V];

#### 4.1.1 Computation of Model Parameters

Analysing equation 4.1 and considering STC<sup>1</sup> the five parameters (unknowns) of the model are  $I_s^r$ ,  $I_0^r$ ,  $m$ ,  $R_s$  and  $R_{sh}$ . A methodology to compute these unknowns using the data present in PV panel catalogs (Table 4.1) is presented in [8]. The first step is to write the equation 4.1 at the three characteristic points of the PV curve I-V — short-circuit point ( $I_{cc}^r$ ), open-circuit point ( $V_{ca}^r$ ) and maximum power point ( $V_{MP}^r$  and  $I_{MP}^r$ ):

$$I_{cc}^r = I_s^r - I_0^r \left[ \exp \left( \frac{0 + R_s I_{cc}^r}{m V_T^r} \right) - 1 \right] - \frac{0 + R_s I_{cc}^r}{R_{sh}} \quad (4.3)$$

$$0 = I_s^r - I_0^r \left[ \exp \left( \frac{V_{ca}^r + 0}{m V_T^r} \right) - 1 \right] - \frac{V_{ca}^r + 0}{R_{sh}} \quad (4.4)$$

$$I_{MP}^r = I_s^r - I_0^r \left[ \exp \left( \frac{V_{MP}^r + R_s I_{MP}^r}{m V_T^r} \right) - 1 \right] - \frac{V_{MP}^r + R_s I_{MP}^r}{R_{sh}} \quad (4.5)$$

To facilitate the calculations, the next simplifications can be made:

$$\exp \left( \frac{V + R_s I}{m V_T} \right) - 1 \approx \exp \left( \frac{V + R_s I}{m V_T} \right) \quad (4.6)$$

---

<sup>1</sup>Standard Test Conditions (STC):  $G^r = 1000$  W/m<sup>2</sup>,  $\theta_c^r = 25$  °C. Typically referenced by using the superscript <sup>r</sup>.

$$\exp\left(\frac{R_s I_{cc}^r}{m V_T^r}\right) \ll \exp\left(\frac{V_{ca}^r}{m V_T^r}\right) \quad (4.7)$$

Considering the previous two simplifications and manipulating equations 4.3 and 4.4 two unknowns can be eliminated:

$$I_0^r = \left(I_{cc}^r - \frac{V_{ca}^r - R_s I_{cc}^r}{R_{sh}}\right) \exp\left(\frac{-V_{ca}^r}{m V_T^r}\right) \quad (4.8)$$

$$I_s^r = I_0^r \exp\left(\frac{V_{ca}^r}{m V_T^r}\right) + \frac{V_{ca}^r}{R_{sh}} \quad (4.9)$$

Substituting equations 4.8 and 4.9 in 4.5 we obtain:

$$I_{MP}^r = I_{cc}^r - \frac{V_{MP}^r + R_s I_{MP}^r - R_s I_{cc}^r}{R_{sh}} - \left(I_{cc}^r - \frac{V_{ca}^r - R_s I_{cc}^r}{R_{sh}}\right) \exp\left(\frac{V_{MP}^r + R_s I_{MP}^r - V_{ca}^r}{m V_T^r}\right) \quad (4.10)$$

In order to complete the system of unknowns, it is necessary two extra equations since there are five unknowns. One of the equations can be obtained from knowing that differentiating the I-V equation 4.1 at MPP is equal to zero:

$$\left.\frac{dP}{dV}\right|_{\substack{V=V_{MP}^r \\ I=I_{MP}^r}} = \left.\frac{d(VI)}{dV}\right|_{\substack{V=V_{MP}^r \\ I=I_{MP}^r}} = \left(I + \frac{dI}{dV} V\right)\bigg|_{\substack{V=V_{MP}^r \\ I=I_{MP}^r}} = \left(I + \frac{\frac{\partial f(I,V)}{\partial V}}{1 - \frac{\partial f(I,V)}{\partial I}} V\right)\bigg|_{\substack{V=V_{MP}^r \\ I=I_{MP}^r}} = 0 \quad (4.11)$$

The last equation necessary to complete the system is obtained from an empirical notion of the shunt resistance obeying the following relation.

$$\left.\frac{dI}{dV}\right|_{I=I_{cc}^r} = \frac{\frac{\partial f(I,V)}{\partial V}}{1 - \frac{\partial f(I,V)}{\partial I}}\bigg|_{I=I_{cc}^r} = -\frac{1}{R_{sh}} \quad (4.12)$$

After some algebraic manipulation of equations 4.11 and 4.12, and including equation 4.10 the system of equations 4.13 can be used to compute the three unknowns  $m$ ,  $R_{sh}$  and  $R_s$ , since the rest of the variables are given by PV panel catalogs. In order to solve the system of equations 4.13 a nonlinear numerical solver should be used. Finally, using equations 4.8 and 4.9 the rest of the unknowns can be computed.

$$\left\{ \begin{aligned}
& I_{cc}^r - \frac{V_{MP}^r + R_s I_{MP}^r - R_s I_{cc}^r}{R_{sh}} - \left( I_{cc}^r - \frac{V_{ca}^r - R_s I_{cc}^r}{R_{sh}} \right) \exp \left( \frac{V_{MP}^r + R_s I_{MP}^r - V_{ca}^r}{m V_T^r} \right) - I_{MP}^r = 0 \\
& I_{MP}^r + \frac{(R_{sh} I_{cc}^r - V_{ca}^r + R_s I_{cc}^r) \exp \left( \frac{V_{MP}^r + R_s I_{MP}^r - V_{ca}^r}{m V_T^r} \right)}{m V_T^r R_{sh}} - \frac{1}{R_{sh}} V_{MP}^r = 0 \\
& 1 + \frac{R_s (R_{sh} I_{cc}^r - V_{ca}^r + R_s I_{cc}^r) \exp \left( \frac{V_{MP}^r + R_s I_{MP}^r - V_{ca}^r}{m V_T^r} \right)}{m V_T^r R_{sh}} + \frac{R_s}{R_{sh}} \\
& \frac{1}{R_{sh}} + \frac{(R_{sh} I_{cc}^r - V_{ca}^r + R_s I_{cc}^r) \exp \left( \frac{R_s I_{cc}^r - V_{ca}^r}{m V_T^r} \right)}{m V_T^r R_{sh}} - \frac{1}{R_{sh}} = 0 \\
& 1 + \frac{R_s (R_{sh} I_{cc}^r - V_{ca}^r + R_s I_{cc}^r) \exp \left( \frac{R_s I_{cc}^r - V_{ca}^r}{m V_T^r} \right)}{m V_T^r R_{sh}} + \frac{R_s}{R_{sh}}
\end{aligned} \right. \quad (4.13)$$

#### 4.1.2 Influence of Irradiance and Temperature on I-V Curve

The One-Diode Model considers that parameters  $m$ ,  $R_s$  and  $R_{sh}$  are independent of atmospheric variations because in reality compared to the other parameters there changes are less significant (the Two-Diode model takes into account variations in parameter  $m$ ). Parameters  $I_0$  and  $I_s$  can be computed by using equations 4.3 and 4.4 and taking into account the relations 4.14 and 4.15 (these can be proven experimentally and/or mathematically).

$$I_{cc}(G, T) = \frac{G}{G_r} [I_{cc}^r + \mu_{I_{cc}}(T - T_r)] \quad (4.14)$$

$$V_{ca}(G, T) = V_{ca}^r + \mu_{V_{ca}}(T - T_r) + m V_T \ln \left( \frac{G}{G_r} \right) \quad (4.15)$$

where:

- $\mu_{I_{cc}}$  - short-circuit current temperature coefficient [A/°C]
- $\mu_{V_{ca}}$  - open-circuit voltage temperature coefficient [V/°C]

Most of the solar manufactures provide temperature coefficients  $\mu_{I_{cc}}$  and  $\mu_{V_{ca}}$  as [%/°C]. In order to utilize the data provided in PV module catalogs in equations 4.14 and 4.15 the next unit modifications should be made.

$$I_{cc}^r [A] \times \frac{\mu_{I_{cc}}}{100} [\%/^{\circ}C] = \mu_{I_{cc}} [A/^{\circ}C] \quad (4.16)$$

$$V_{ca}^r [V] \times \frac{\mu_{V_{ca}}}{100} [\%/^{\circ}C] = \mu_{V_{ca}} [V/^{\circ}C] \quad (4.17)$$

### 4.1.3 PV Cell Temperature

Equations 4.1 to 4.15 utilize the PV cell temperature, however, typically the data available is atmospheric temperatures. So in order to calculate the expected temperature of the PV cell for a specific atmospheric temperature a simplified temperature model can be used:

$$\theta_c = \theta_a + \frac{G(NOCT - 20)}{800} \quad (4.18)$$

where:

- $\theta_c$  - cell temperature [ $^{\circ}\text{C}$ ]
- $\theta_a$  - atmospheric temperature [ $^{\circ}\text{C}$ ]
- $NOCT^2$  - nominal operating cell temperature [ $^{\circ}\text{C}$ ]

## 4.2 Implementation of the Mathematical Model

Since the proposed power converter has the current as a state variable, a common practice [12], [13] and [14] is to substitute the current source  $I_S$  and diode  $D$  for an equivalent controlled voltage source. Since equation 4.1 is transcendent a simplification can be made by neglecting the leakage current  $I_{sh}$  (because  $I_{sh} \ll I$ ), which allows it to become non-transcendent and enables the equivalent voltage source to be computed.

$$V_D = V + R_s I = mV_T \ln \left( \frac{I_S - I}{I_0} + 1 \right) \quad (4.19)$$

Currently the average peak power<sup>3</sup> of the predominant PV module technology, Mono-crystalline silicon 60-cell, is around 270W, so it only makes sense to design the proposed power converter for a similar power. The main electrical data for the chosen PV module can be found in Table below.

Table 4.1: PV module main electrical data (Appendix B).

$P_{MP}^r [\text{W}_p]$	$V_{MP}^r [\text{W}]$	$I_{MP}^r [\text{A}]$	$V_{ca}^r [\text{V}]$	$I_{cc}^r [\text{A}]$	$NOCT [^{\circ}\text{C}]$	$\mu_{Vca} [\text{mV}/^{\circ}\text{C}]$	$\mu_{Icc} [\text{mA}/^{\circ}\text{C}]$
270	31.1	8.67	38.2	9.19	45 $\pm$ 2	-118.4	4.9

Utilizing the data in Table 4.1 and the equations of subchapter 4.1.1, the parameters of the mathematical model can be computed and found in Table 4.2.

In order to prove that the model behaves as expected a number of tests can be made, including varying atmospheric conditions and comparing the results to available catalog data. Analysing Figures 4.2 and 4.3 it is shown that the proposed model is a good approximation to the real PV module since the IV-curves of the Simulink simulation and catalog data are nearly identical.

<sup>2</sup>Nominal Operating Cell Temperature (NOCT): irradiance of  $800\text{W}/\text{m}^2$  and ambient temperature  $20^{\circ}\text{C}$ . More realistic conditions than STC for atmospheric exposed PV modules.

<sup>3</sup>Peak Power ( $P_p$ ): equivalent to maximum power at STC.

Table 4.2: Computed PV module mathematical model parameters.

$m$	$R_{sh} [\Omega]$	$R_s [\Omega]$	$I_0^r [\text{pA}]$	$I_s^r [\text{A}]$
62.3	786	0.2748	407.33	9.1932

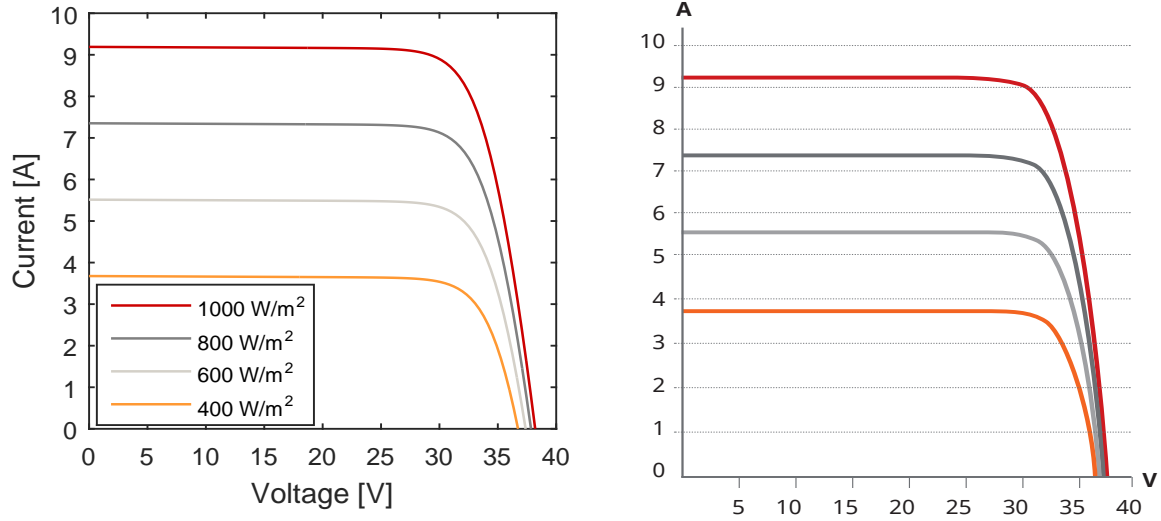


Figure 4.2: IV-curves for different levels of irradiance (with  $\theta_c = 25^\circ\text{C}$ ). Left: Simulink Simulation. Right: PV Catalog.

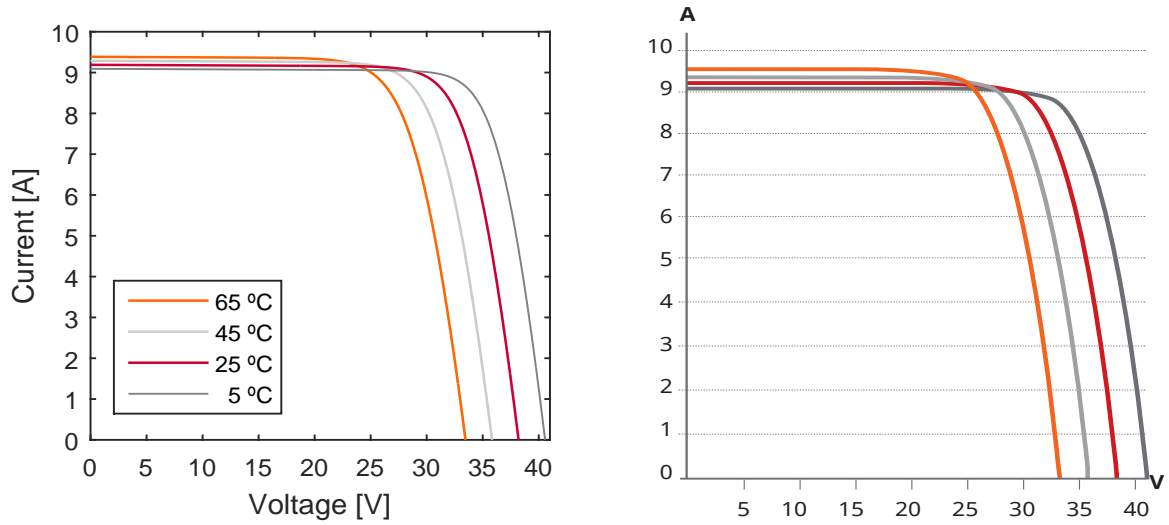


Figure 4.3: IV-curves for different levels of temperature (with  $G = 1000 \text{ W/m}^2$ ). Left: Simulink Simulation. Right: PV Catalog.

A more strict evaluation of the simulations shown in Figures 4.2 and 4.3 can be made based on the percentage error, equation (4.20), which results are depicted in Table 4.3 and Table 4.4.

$$\%error = \frac{|catalog - simulated|}{catalog} \times 100 \quad (4.20)$$

Table 4.3: Comparison of the mathematical model results to the PV catalog (Fig. 4.2).

$[W/m^2]$	$G = 1000$	$G = 800$	$G = 600$	$G = 400$
% error $I_{cc}$	0.0	0.2	0.3	0.3
% error $V_{ca}$	0.0	1.2	1.1	1.2

Table 4.4: Comparison of of mathematical model results to PV catalog data (Fig. 4.3).

$[^{\circ}C]$	$\theta_c = 65$	$\theta_c = 45$	$\theta_c = 25$	$\theta_c = 5$
% error $I_{cc}$	0.3	0.2	0.0	0.2
% error $V_{ca}$	0.8	0.5	0.0	0.6

STC and NOCT condition simulations (Fig. 4.4) should also be compared to the data available in Tables in the PV catalog B.1. Note that in Figure 4.4 both irradiance and temperature are changed, while previous Figures 4.2 and 4.3 only one of these changes while the other remains constant.

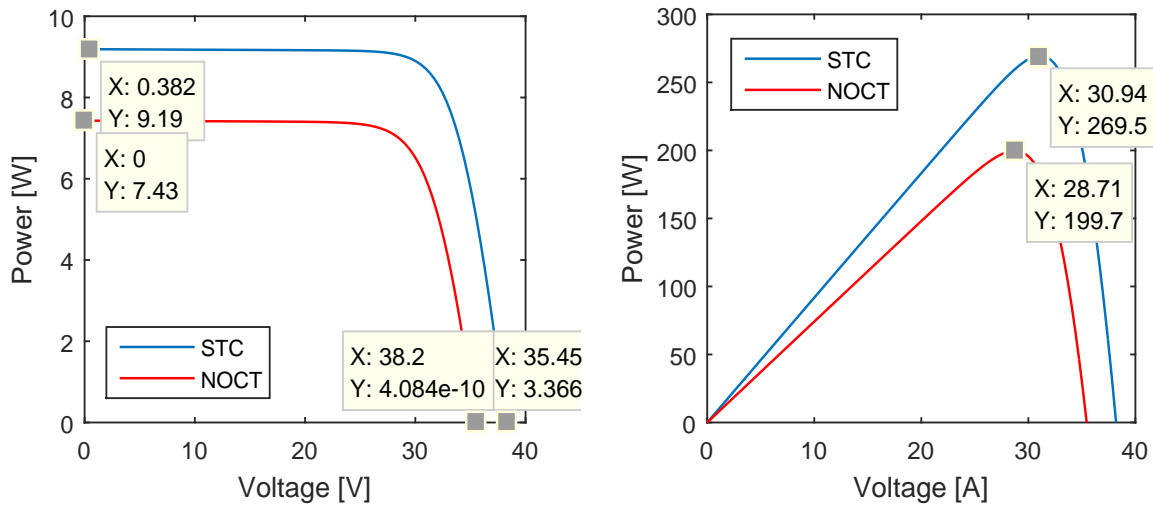


Figure 4.4: Left: IV-curves with highlighted  $V_{ca}$  and  $I_{cc}$  points. Right: PV module power with highlighted  $MPP$  point.

Analysing Figures 4.2, 4.3 and Tables 4.3, 4.4 and 4.5, which all have low % *error*, prove that the mathematical model is an adequate representation of the real PV module (Appendix B).

Table 4.5: Comparison of the mathematical model results to the PV catalog Table data.

	$P_{MP}$	$V_{MP}$	$V_{ca}$	$I_{cc}$
% error <sub>STC</sub>	0.19	0.51	0	0
% error <sub>NOCT</sub>	2.41	1.09	1.29	0.13

## Chapter 5

# Proposed Microinverter

### 5.1 Introduction

As explained in Chapter 2, the Active-Clamp Full-Bridge Boost Converter [26] is a good solution for the isolated DC-DC converter stage due to its low number of components and easy control. The interface between the DC-DC converter and the grid will be done using a half-bridge inverter since it further decreases the needed capacitance. The complete microinverter is shown in Figure 5.1.

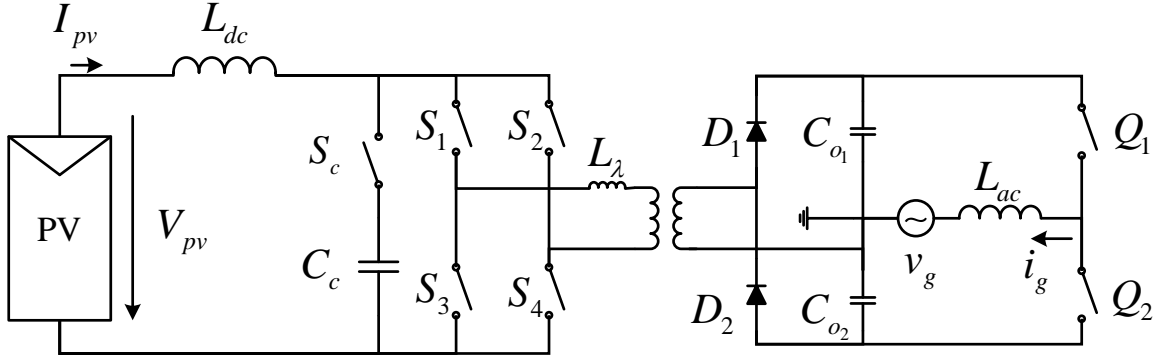


Figure 5.1: Proposed AC-module circuit.

### 5.2 Active-Clamp Full-Bridge Boost Converter

The Active-Clamp Full-Bridge Boost Converter is responsible for guaranteeing MPPT while boosting the voltage. By controlling the DC current level of the intermediate inductor  $L_{dc}$  the MPPT can be achieved while the elevation of the voltage is obtained by two boost stages, one in the intermediate inductor  $L_{dc}$  which acts naturally as a step-up converter and the other at the step-up transformer. The full-bridge is responsible for transforming the DC voltage to an AC high frequency rectangular voltage waveform which can then be applied to the high frequency transformer, to avoid this this one from saturating.

The Active-Clamp circuit is composed by a capacitor  $C_c$  and a bidirectional semiconductor  $S_c$  (i.e. with a parallel diode) and is used in order to connect the intermediate inductor  $L_{dc}$  to the high frequency transformer which has an intrinsic leakage inductor  $L_\lambda$ . Then, the Active-Clamp

semiconductor  $S_c$  should be turned on whenever the circuit is in a transfer mode (Subfigures (a) to (d) of Fig. 5.2). At the beginning of this mode (Subfigures (a) and (c)) the diode of the semiconductor  $S_c$  will be forward biased since the voltage at the terminal of  $L_{dc}$  will be higher than the voltage of  $C_c$ . This will cause the current to flow to the capacitor  $C_c$  while the current  $I_{L_\lambda}$  increases gradually. Once the currents  $I_{L_{dc}}$  and  $I_{L_\lambda}$  are equal, the capacitor  $C_c$  will start to discharge (Subfigures (b) and (d)) since voltage  $V_{C_c}$  will be greater than the voltage at the terminal of  $L_{dc}$ .

When the circuit is in the current boost mode (Subfigure (e)) the voltage across the terminal of  $L_{dc}$  will be positive so its current will increase. During this mode the semiconductor  $S_c$  should be switched off in order to not short-circuit the active-clamp capacitor  $C_c$ . The diode of the semiconductor  $S_c$  will be reversed polarized so the capacitor  $C_c$  is open circuited maintaining its voltage.

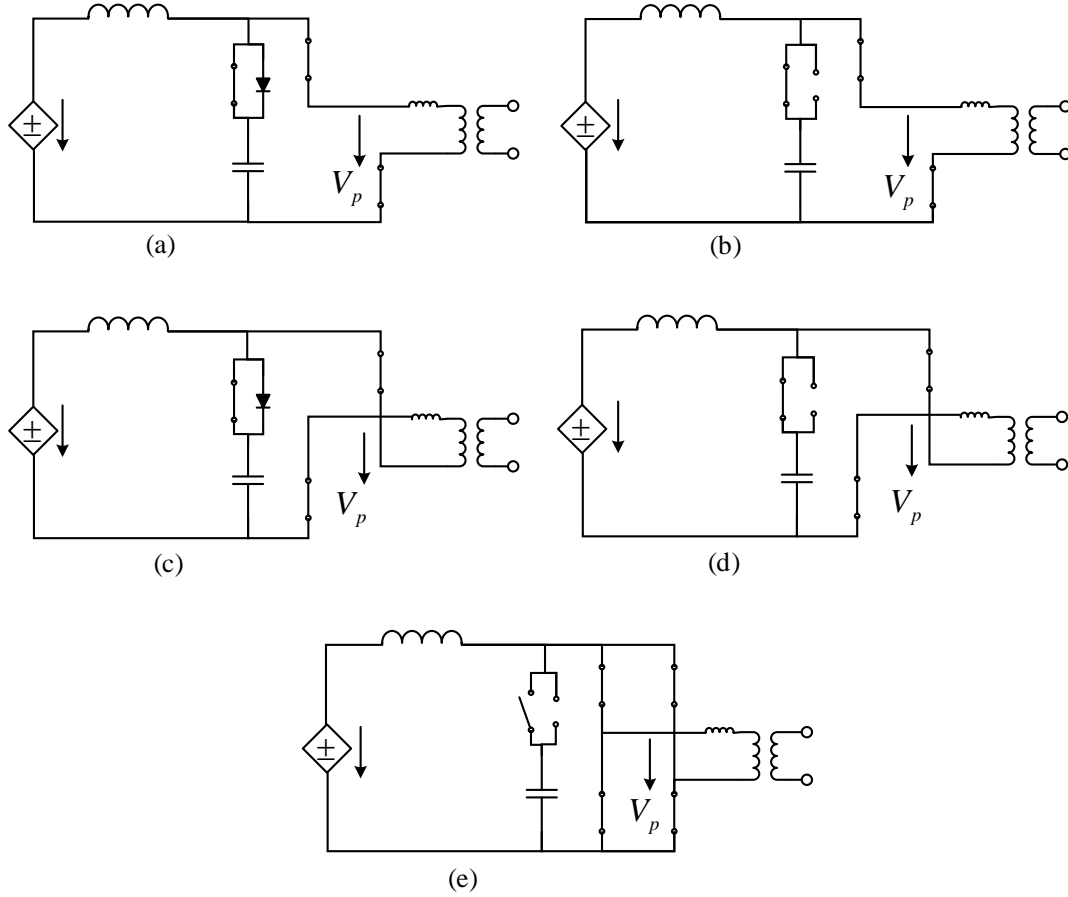


Figure 5.2: Active-Clamp Boost Full-Bridge converter operation modes.

In order to achieve an AC voltage with a zero mean value a pulse width modulation technique can be used. The firing angles of the semiconductors of this type of modulation can be found in equation 5.1 where  $\delta$  represents the duty cycle provided from the MPPT controller and  $\omega_{pwm}$  represents the angular frequency of the PWM triangular carrier. The chosen frequency of the PWM is  $f_{pwm} = 10\text{ kHz}$ .

$$\begin{aligned}
\frac{\pi - \delta}{2} < \omega_{pwm} t < \frac{\pi + \delta}{2} &\implies S_{1,4} \text{ \& } S_c \text{ on } \wedge S_{2,3} \text{ off} \implies v_p = +V_{dc} \text{ (transfer)} \\
\frac{\pi + \delta}{2} < \omega_{pwm} t < \frac{3\pi - \delta}{2} &\implies S_{1,2,3,4} \text{ on } \wedge S_c \text{ off} \implies v_p = 0 \text{ (boost)} \\
\frac{3\pi - \delta}{2} < \omega_{pwm} t < \frac{3\pi + \delta}{2} &\implies S_{2,3} \text{ \& } S_c \text{ on } \wedge S_{1,4} \text{ off} \implies v_p = -V_{dc} \text{ (transfer)} \\
\frac{3\pi + \delta}{2} < \omega_{pwm} t < 2\pi + \frac{\pi - \delta}{2} &\implies S_{1,2,3,4} \text{ on } \wedge S_c \text{ off} \implies v_p = 0 \text{ (boost)}
\end{aligned} \tag{5.1}$$

Using the PWM described in (5.1), the waveforms of the Active-Clamp Full-Bridge can be obtained. An approximated representation of the waveforms which result from the PWM are shown in Figure 5.3 (found in [4]), where  $T_s$  is the time period of the transformer. These waveforms will be used to design the active components of the DC-DC converter later on.

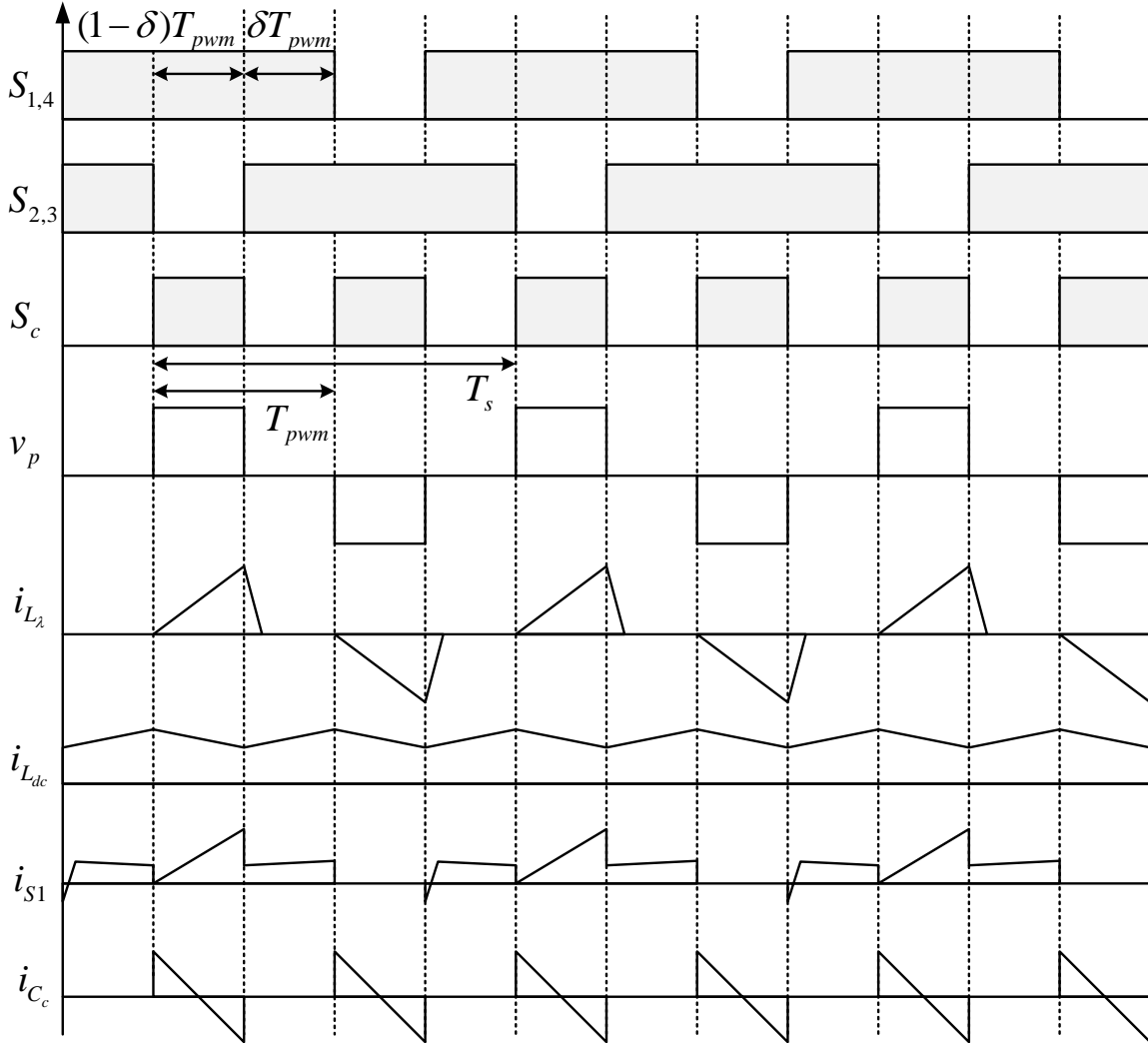


Figure 5.3: Expected waveforms of the Active-Clamp Boost Full-bridge converter.

### 5.2.1 Design Procedure

The DC-DC converter is expected to be able to maintain MPPT for a wide range of atmospheric conditions. So in order for the DC-DC converter to work correctly its passive components should be sized taking into account the different possible ranges of atmospheric conditions while taking care to not over-size each component.

Currently, there are various testing conditions [15] to test the performance and output of solar PV modules. This approach can be used to dimension the power converter connected to the PV module. The main test conditions are shown in Table 5.1.

Table 5.1: Comparative Table of solar panel test conditions.

Testing Condition	Abbreviation	$G$ [ $W/m^2$ ]	$\theta_c$ [ $^{\circ}C$ ]
High Temperature Conditions	HTC	1000	75
Low Irradiance Conditions	LIC	200	25
Low Temperature Conditions	LTC	500	15
Nominal Operating Cell Temperature	NOCT	800	45
Standard Test Conditions	STC	1000	25

Using the mathematical model explained in the previous chapter, the voltage and current at MPP for the various test conditions can be computed and found in Table 5.2.

Table 5.2: PV module expected output values for different testing conditions.

Testing Condition	$V_{MP}$ [V]	$I_{MP}$ [A]	$P_{MP}$ [W]
HTC	25.07	8.69	218
LIC	30.35	1.71	52
LTC	32.39	4.32	140
NOCT	28.72	6.95	200
STC	31.10	8.67	270

By analysing Figure 5.2, it can be shown that there are clear similarities between the Active-Clamp Full-bridge converter and a boost converter. Based on this premise the components of the

Active-Clamp Full-Bridge Boost converter can be determined [4]. A methodology to compute the components of a Boost converter is presented in [1] and will be used in the following sections along with the different electrical values presented in Table 5.2.

### 5.2.2 Transformer Turns Ratio

The first element that should be designed is the turns ratio  $n$  of the high-frequency transformer, since the rest of the components depend on the value of  $n$ . In order for the output inverter to work correctly the voltage at capacitors  $C_o$  should be maintained at a higher level than the maximum expected grid voltage ( $V_o > 1.1\sqrt{2}v_{g_{RMS}} = 358\text{ V}$ , Figure 2.5) to be able to impose the current flow through inductor  $L_{ac}$ .

By choosing  $V_o = 410\text{ V}$  (which allows for a greater ripple and consequent smaller capacitance - Figure 2.5 and equation 5.31) and assuming that the voltage boost from the intermediate inductor  $L_{dc}$  has a gain equal to two, the turns ratio should be sized for the lowest voltage present in Table 5.2.

$$n = \frac{n_p}{n_s} = \frac{2 \times V_{MP_{MIN}}}{V_o} \approx \frac{1}{8} \quad (5.2)$$

Since  $V_o$  is maintained constant the primary voltage of the transformer will be equal to:

$$V_p = n \times V_o \quad (5.3)$$

### 5.2.3 Transformer Parameters

Power converters switching frequencies are normally dependent on the type of active components that are needed to withstand a certain electrical power. Since there is a large range of possible frequencies, its not as easy to find an appropriate high frequency transformer for a specific power converter as their counterpart low frequency grid transformers. The transformer design is out of the scope of this thesis, so a simplified procedure [4] to estimate the transformer parameters will be used. The equivalent electrical circuit of the transformer is shown in the Figure 5.4.

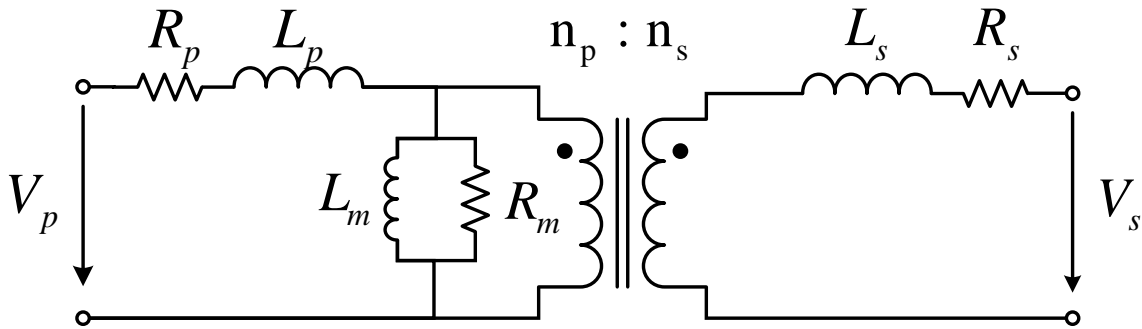


Figure 5.4: Equivalent Electrical Transformer Circuit.

where:

- $R_p$  and  $R_s$  - primary and secondary equivalent windings resistances (joule losses);
- $L_p$  and  $L_s$  - primary and secondary equivalent leakage inductances (magnetic flux losses, which leads to a decrease in voltage or voltage drop);

- $R_m$  - equivalent iron core resistance (Eddy current and hysteresis losses);
- $L_m$  - equivalent magnetizing inductance (magnetic energy stored);

Since the PV module has a power of 270 W the semiconductor technology chosen is the MOSFET, with a switching frequency of 10 kHz (PWM). In Figure 5.1 its shown that the working frequency of the transformer  $f_s$  is half of that of the PWM frequency. The simplified approach to designing the transformer considers that the losses can be assumed. We are going to assume that the transformer has 0.004 pu of coil resistance and 0.02 pu of leakage inductance.

As shown in Figure 5.1 the voltage applied to the transformer is rectangular, meaning its rms value is equal to the peak voltage applied. With this in mind the base values for the transformer are given below:

$$\begin{cases} S_{base} = 270 \text{ VA} \\ V_{base_P} = 51 \text{ Vrms} \\ V_{base_S} = 410 \text{ Vrms} \end{cases} \quad (5.4)$$

The rest of the based units can be derived from power and voltage bases:

$$\begin{cases} R_{base_P} = \frac{V_{base_P}^2}{S_{base}} \\ L_{base_P} = \frac{V_{base_P}^2}{S_{base}} \frac{1}{2\pi f_s} \\ R_{base_S} = \frac{V_{base_S}^2}{S_{base}} \\ L_{base_S} = \frac{V_{base_S}^2}{S_{base}} \frac{1}{2\pi f_s} \end{cases} \quad (5.5)$$

Finally by assuming the expected losses at the dissipative elements of the transformer, the parameters of the circuit can be computed as:

$$\begin{cases} R_p = 0.004 R_{base_P} \\ L_p = 0.02 L_{base_P} \\ R_s = 0.004 R_{base_S} \\ L_s = 0.02 L_{base_S} \end{cases} \quad (5.6)$$

In order to correctly design the active clamp capacitor  $C_C$  later on, the total leakage inductance must be determined beforehand, as shown in equation (5.7).

$$L_\lambda = L_p + L_s n^2 = 12 \mu H \quad (5.7)$$

#### 5.2.4 Intermediate Inductor

The Intermediate Inductor  $L_{dc}$ , has to be sized to maintain a constant DC current that is provided by the PV module. The current should have a low ripple in order to obtain a stable MPPT. The voltages seen across the inductor are:

$$v_{Ldc}(t) = \begin{cases} V_{mp} - V_p & , 0 < t < \delta T_{pwm} \\ V_{mp} & , \delta T_{pwm} < t < T_{pwm} \end{cases} \quad (5.8)$$

Assuming a current ripple of  $\Delta i_{Ldc} = 0.03 I_{mp}$  the intermediate inductor can be computed [1] as:

$$L_{dc} = \frac{V_{mp}}{\Delta i_{Ldc}} \delta T_{pwm} = \frac{V_p - V_{mp}}{\Delta i_{Ldc}} (1 - \delta) T_{pwm} = \frac{V_{mp}(V_p - V_{mp})}{\Delta i_{Ldc} V_p f_{pwm}} \quad (5.9)$$

where the duty cycle  $\delta$  can be obtained from knowing that the average inductance voltage is equal to zero:

$$v_{LdcAV} = \frac{1}{T_{pwm}} \left[ \int_0^{\delta T_{pwm}} V_{mp} dt + \int_{\delta T_{pwm}}^{T_{pwm}} (V_{mp} - V_p) dt \right] = 0 \quad (5.10)$$

after some computation:

$$\delta = 1 - \frac{V_{mp}}{V_p} \quad (5.11)$$

Considering low current ripple in order to guarantee MPPT (3%) and using the data available in Table 5.2, the different values of  $L_{dc}$  can be obtained using the equation (5.9). Analysing Table 5.3 its shown that the inductor for LIC conditions is substantially higher to the other conditions. In order to not over-size the inductor the worst case will not be chosen, instead we will choose an intermediate inductor with a value equal to  $L_{dc} = 6 \text{ mH}$  closer to NOCT.

Table 5.3: Necessary intermediate inductor and duty cycle for different atmospheric conditions.

Testing Condition	$L_{dc} [\text{mH}]$	$\delta$
HTC	3.6	0.50
LIC	22.4	0.39
LTC	9.4	0.35
NOCT	5.2	0.43
STC	4.5	0.38

### 5.2.5 Active-Clamp Capacitor

The design proposed in [26] is based on the resonant tank formed by  $C_c$  and  $L_\lambda$ . The resonance occurs during the transfer mode operation. A condition of resonance will be experienced in a tank circuit (Fig. 5.5) when the reactances of the capacitor and inductor are equal to each other. Because inductive reactance increases with increasing frequency and the capacitive reactance decreases with

increasing frequency, there will only be one frequency where these two reactances are equal, this premise will be used in the MPPT and is the reason why the active-clamp full-bridge should have a fixed PWM frequency controller.

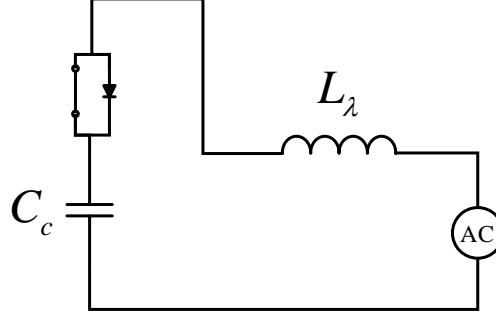


Figure 5.5: Resonant Tank Formed between  $C_c$  and  $L_\lambda$ .

Since the resonant tank occurs during the transfer mode, it has a duration equal to  $T_{rt} = T_{pwm}(1 - \delta)$  which leads to a frequency of  $f_{rt} = 1/T_{rt}$ . The value of  $C_c$  can be determined by equalizing both reactances  $Z_{C_c}$  and  $Z_{L_\lambda}$ :

$$\frac{1}{2\pi f_{rt} C_c} = 2\pi f_{rt} L_\lambda \quad (5.12)$$

after some manipulation:

$$C_c = \frac{\left(\frac{T_{rt}}{2\pi}\right)^2}{L_\lambda} = 8.3 \mu F \quad (5.13)$$

### 5.2.6 Active Components of Full-Bridge Inverter and Active-Clamp

The semiconductors should be chosen based on the following voltage parameters:

- $V_{DRM}$  - maximum repetitive peak forward voltage (MOSFET).
- $V_{RRM}$  - maximum repetitive peak reverse voltage (Diode).

and two current parameters:

- $I_{AV}$  - average current.
- $I_{MAX}$  - maximum current.

while:

- $I_{RMS}$  - root-mean-square value of the current is used to compute the losses.

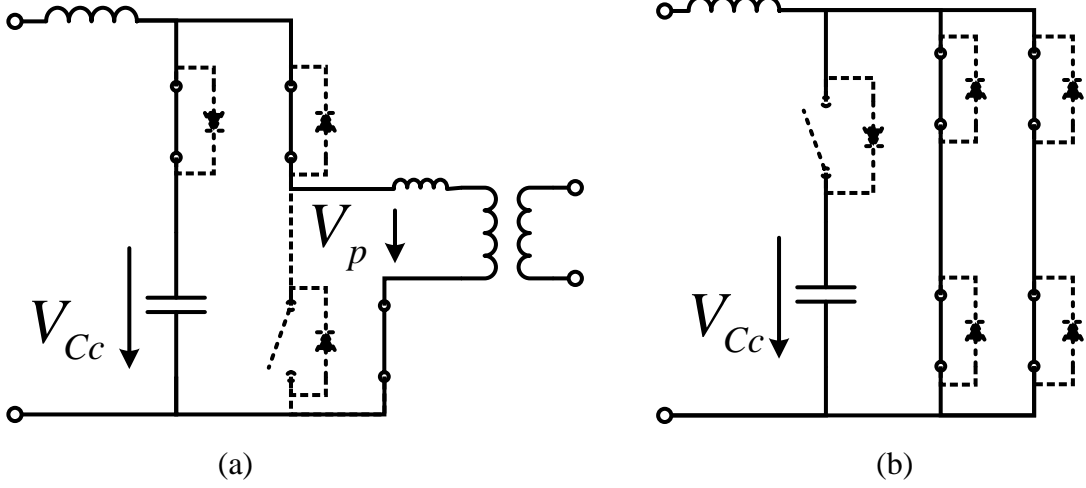


Figure 5.6: Semiconductors highlighted (a): Transfer mode (b): Current boost mode.

Analysing Figure 5.6 it can be shown that semiconductors  $S_1, S_2, S_3, S_4$  (transfer mode) and  $S_c$  (current boost mode) have a  $V_{RRM}$  of:

$$V_{RRM} \geq \frac{V_{Cc}}{2} = \frac{V_p}{2} \quad (5.14)$$

while the  $V_{DRM}$  value of semiconductors  $S_1, S_2, S_3, S_4$  (current boost mode) and  $S_c$  (transfer mode) is given by:

$$V_{DRM} \geq V_{Cc} = V_p \quad (5.15)$$

The current parameters  $I_{AV}$ ,  $I_M$  and  $I_{RMS}$  can be estimated from the key waveforms in Figure 5.3 as explained in [4]. The average current through the full-bridge semiconductors can be computed as:

$$I_{Si_{AV}} = \frac{1}{T_s} \left[ \int_0^{\frac{\delta T_s}{2}} \frac{I_{mp}}{2} dt + \int_{\frac{\delta T_s}{2}}^{\frac{T_s}{2}} (I_{mp} - I_{Cc}) dt + \int_{\frac{T_s}{2}}^{\frac{T_s}{2} + \frac{\delta T_s}{2}} \frac{I_{mp}}{2} dt \right] \quad (5.16)$$

Analysing Figure 5.3 it can be shown that the integral can be approximated by a sum of two equal rectangles with a height of  $\frac{1}{2}I_{mp}$  and width  $\frac{\delta T_s}{2}$ , and a triangle with a height of  $2I_{mp}$  and width equal to  $(1 - \delta)\frac{T_s}{2}$  resulting in:

$$I_{Si_{AV}} \cong \frac{1}{T_s} \left[ 2 \left( \frac{I_{mp}}{2} \times \frac{\delta T_s}{2} \right) + \left( 2I_{mp} \times \frac{(1 - \delta)T_s}{2} \right) \frac{1}{2} \right] \quad (5.17)$$

The full-bridge currents root-mean-square value is given by:

$$I_{Si_{RMS}} = \sqrt{\frac{1}{T_s} \left[ \int_0^{\frac{\delta T_s}{2}} \left( \frac{I_{mp}}{2} \right)^2 dt + \int_{\frac{\delta T_s}{2}}^{\frac{T_s}{2}} (I_{mp} - I_{Cc})^2 dt + \int_{\frac{T_s}{2}}^{\frac{T_s}{2} + \frac{\delta T_s}{2}} \left( \frac{I_{mp}}{2} \right)^2 dt \right]} \quad (5.18)$$

Considering that between  $\delta \frac{T_s}{2}$  and  $\frac{T_s}{2}$  the current  $I_{Si}$  follows a line equation equal to  $y = \frac{2I_{mp}}{(1-\delta)T_s} t$  the previous equation can be transformed to:

$$I_{Si_{RMS}} \approx \sqrt{\frac{1}{T_s} \left[ \int_0^{\frac{\delta T_s}{2}} \left( \frac{I_{mp}}{2} \right)^2 dt + \int_{\frac{\delta T_s}{2}}^{\frac{T_s}{2}} \left( \frac{2I_{mp}}{(1-\delta)T_s} t \right)^2 dt + \int_{\frac{T_s}{2}}^{\frac{T_s}{2} + \frac{\delta T_s}{2}} \left( \frac{I_{mp}}{2} \right)^2 dt \right]} \quad (5.19)$$

The maximum current through the full-bridge semiconductors is (main disadvantage of this power converter, Table 2.1, full-bridge converters switches must conduct current from the auxiliary active-clamp circuit in addition to that of PV module.):

$$I_{Si_{MAX}} = 2 \times I_{mp} \quad (5.20)$$

In steady state the average current flowing through the capacitor is equal to zero, so the average current through  $S_C$  is:

$$I_{Sc_{AV}} = 0 \quad (5.21)$$

To determine the RMS current of semiconductor  $S_C$  the same procedure can be used as before.

$$I_{Sc_{RMS}} = \sqrt{\frac{1}{T_{pwm}} \left[ \int_0^{(1-\delta)T_{pwm}} (I_{Cc})^2 dt \right]} \quad (5.22)$$

The current  $I_{Cc}$  can be approximated by a line equation equal to  $y = -\frac{I_{mp}}{(1-\delta)T_{pwm}} t + I_{mp}$ , the previous equation is transformed into:

$$I_{Sc_{RMS}} \approx \sqrt{\frac{1}{T_{pwm}} \left[ \int_0^{(1-\delta)T_{pwm}} \left( -\frac{I_{mp}}{(1-\delta)T_{pwm}} t + I_{mp} \right)^2 dt \right]} \quad (5.23)$$

while the maximum current is given by:

$$I_{Sc_{MAX}} = I_{mp} \quad (5.24)$$

Finally, we have all the necessary equations to compute the limit voltage and current values which are parameters used to select adequate semiconductors (Table 5.4). The active components should have a safety margin as a countermeasure against possible over-voltages or over-currents.

Table 5.4: Comparison of limit values and chosen semiconductors for the DC-DC converter.

	$S_i$		$S_c$	
Parameter	Limit Value	Chosen MOSFET	Limit Value	Chosen MOSFET
$V_{DRM}$ [V]	51	100	51	100
$I_{AV}$ [A]	7.0	19.7	0.0	8.8
$I_{RMS}$ [A]	11.3	—	3.9	—
$I_{MAX}$ [A]	17.3	70	8.7	60

### 5.3 Grid Inverter

The inverter is responsible for injecting the power produced locally by the PV module into the utility grid. There are two principle typologies used, voltage switched inverters (VSI) and current source inverters (CSI). CSI are used typically for medium to high current applications because for low currents the energy storage DC inductance needed is very large in order to avoid discontinuous mode operation [33], [34].

The VSI chosen is the half-bridge topology. This type of inverter has a higher total harmonic distortion (THD) when compared to a  $1\phi$  three-level full-bridge inverter, but the capacitors needed for the DC-link are smaller. The Active-Clamp Full-Bridge converter is connected to the inverter via a half-bridge rectifier as shown in Figure 5.7.

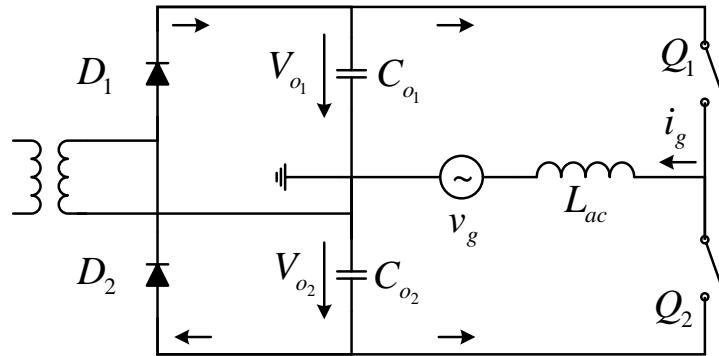


Figure 5.7: Main voltages and currents of the half-bridge rectifier and grid inverter.

### 5.3.1 DC Capacitors

When both the grid voltage  $v_g$  and the output current  $i_g$  have sinusoidal unity power factor, the instantaneous output power is expressed as follows:

$$\begin{aligned} p_o &= V_{g_p} I_{g_p} \sin^2(\omega t) \\ &= \frac{1}{2} V_{g_p} I_{g_p} - \frac{1}{2} V_{g_p} I_{g_p} \cos(2\omega t) \end{aligned} \quad (5.25)$$

Equation 5.25 shows a power pulsation with twice the grid frequency which appears in the output power. In order to decouple the power pulsation, the buffer circuit (capacitors  $C_o$ ) instantaneous power  $p_{buf}$  required is given by:

$$p_{buf} = -\frac{1}{2} V_{g_p} I_{g_p} \cos(2\omega t) \quad (5.26)$$

where the polarity of  $p_{buf}$  is defined as positive when the buffer capacitor discharges. The mean power of the buffer circuit is zero and the buffer capacitors only absorb the power pulsation. Consequently, the instantaneous input power  $p_{in}$  will be constant and equal to:

$$p_{in} = \frac{1}{2} \frac{V_{g_p} I_{g_p}}{\eta} = V_{mp} I_{mp} \quad (5.27)$$

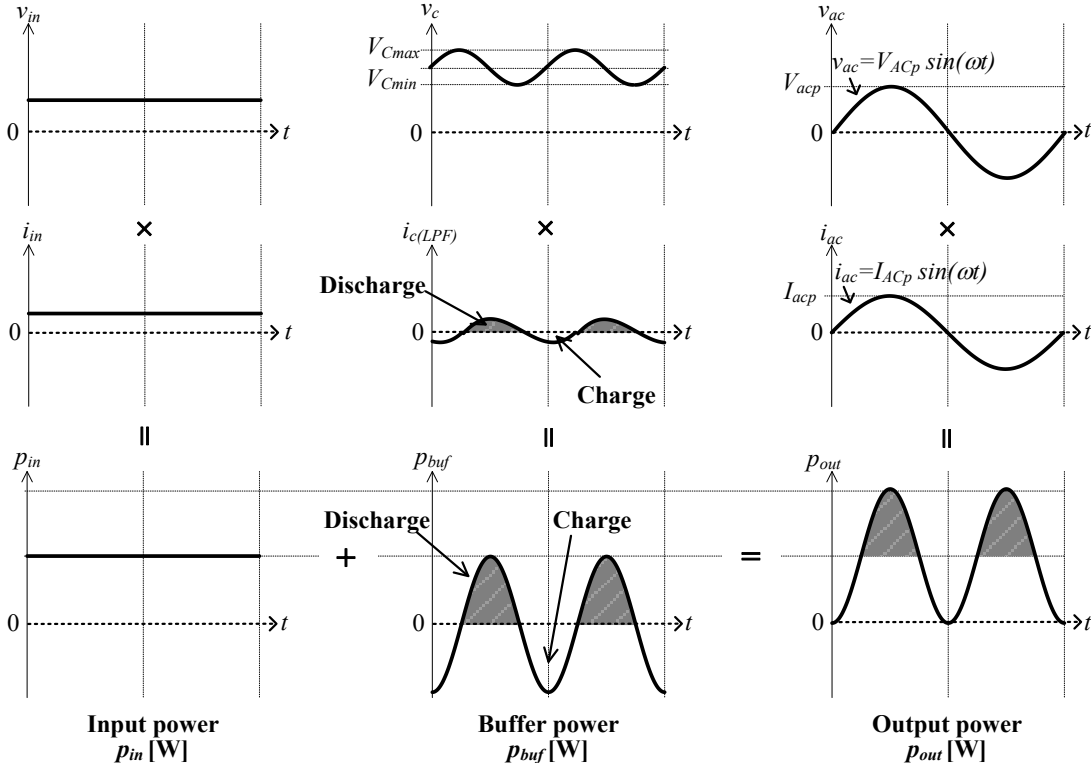


Figure 5.8: Power decoupling achieved by the buffer circuit. (source [34])

If each capacitor stores half of the power pulsation  $p_{buf}$  we have:

$$\begin{aligned} p_{buf} &= \frac{1}{2} V_{g_p} I_{g_p} \cos(2\omega t) \\ p_{C_o} + p_{C_o} &= V_{g_{RMS}} I_{g_{RMS}} \cos(2\omega t) \\ 2V_o i_{C_o} &= V_{g_{RMS}} I_{g_{RMS}} \cos(2\omega t) \end{aligned} \quad (5.28)$$

A method to compute the  $C_o$  capacitors is proposed in [2] and listed below:

$$\begin{aligned} v_{C_oAC} &= \frac{1}{C_o} \int_0^t i_{C_o} dt \\ &= \frac{1}{C_o} \int_0^t \frac{1}{2} \frac{V_{g_{RMS}} I_{g_{RMS}}}{V_o} \cos(2\omega t) dt \\ &= \frac{1}{4} \frac{V_{g_{RMS}} I_{g_{RMS}}}{\omega C_o V_o} \sin(2\omega t) \end{aligned} \quad (5.29)$$

where if:

$$\begin{aligned} \Delta V_o &= v_{C_oMAX} - v_{C_oMIN} \\ &= \frac{1}{4} \frac{V_{g_{RMS}} I_{g_{RMS}}}{\omega C_o V_o} [1 - (-1)] \end{aligned} \quad (5.30)$$

Then, if we assume a voltage ripple equal to 5% and an efficiency  $\eta = 95\%$  then:

$$C_o = \frac{1}{2} \frac{\eta V_{mp} I_{mp}}{\Delta V_o \omega V_o} \approx 50 \mu F \quad (5.31)$$

### 5.3.2 AC Inductor

The AC inductor is responsible for enabling unity power factor by the VSI, since it imposes continuous conduction mode in the grid injected current  $i_g$ . There are two premises [2] which can be used to estimate the limit values of the AC inductor as explained below.

Analysing Figure 5.9 it can be shown that in order to achieve near unity power factor the voltage at the output of the half-bridge inverter  $v_{pwm}$  must be such that:

$$v_{pwmAV}(t) = v_g + v_{Lac} = \sqrt{2} V_{g_{RMS}} \sin(\omega t) + \sqrt{2} \omega L_{ac} I_{1g_{RMS}} \sin\left(\omega t - \frac{\pi}{2}\right) \quad (5.32)$$

which implies that:

$$V_o > |v_{pwmAV}| = \sqrt{2 \left( V_{g_{RMS}}^2 + \omega^2 L_{ac}^2 I_{1g_{RMS}}^2 \right)} \quad (5.33)$$

where  $I_{1g_{RMS}}$  can be computed based on the desired displacement power factor  $\cos \varphi_1$ :

$$I_{1g_{RMS}} = \frac{\eta P_{mp}^{Total}}{V_{g_{RMSMIN}} \cos \varphi_1} \quad (5.34)$$

After some manipulation of the inequality 5.33 the upper limit of the AC inductor can be computed as:

$$L_{acMAX} < \frac{\sqrt{\frac{V_o^2}{2} - V_{gRMS}^2}}{\omega I_{1gRMS}} \quad (5.35)$$

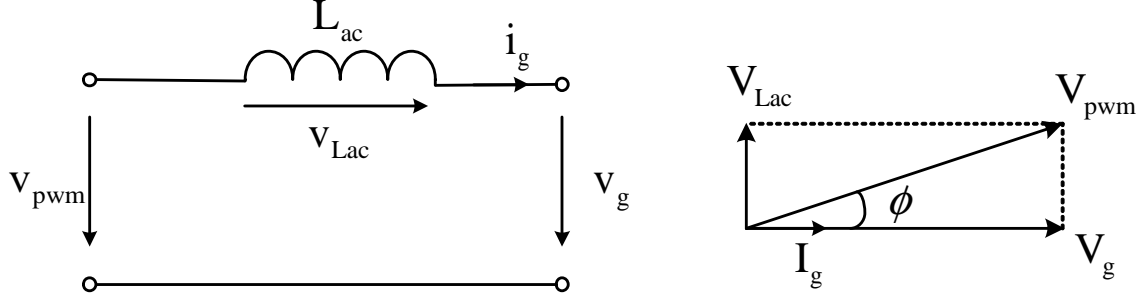


Figure 5.9: AC inductor responsible for enabling unity power factor and respective vector diagram.

The reactive power injected into the grid by the VSI can be controlled by adjusting the magnitude of  $v_{pwm}$  while the active power is controlled by adjusting the angle  $\phi$  (as done in [33]).

The lower limit value of the AC inductor is based on the fact that the VSI acts as a buck converter since the grid voltage  $v_g$  is lower than the capacitors voltage  $V_o$ . To compute the AC inductor  $L_{ac}$  the same method used in sub-chapter 5.2.4 can be preformed.

$$v_{Lac}(t) = \begin{cases} V_o - V_{gAV} & , 0 < t < \delta T_{pwm} \\ -V_o - V_{gAV} & , \delta T_{pwm} < t < T_{pwm} \end{cases} \quad (5.36)$$

where:

$$V_{pwmAV} = \frac{1}{T_{pwm}} \left[ \int_0^{\delta T_{pwm}} V_o dt + \int_{\delta T_{pwm}}^{T_{pwm}} -V_o dt \right] = V_o (2\delta - 1) \quad (5.37)$$

Since  $V_{LacAV} = 0$  the relation between  $V_{pwmAV}$  and  $V_{gAV}$  can be obtained:

$$\begin{aligned} V_{gAV} &= V_{pwmAV} - V_{LAV} \\ &= V_o (2\delta - 1) \end{aligned} \quad (5.38)$$

Using equations 5.36 and 5.38  $L_{ac}$  can be given by:

$$L_{ac} = \frac{V_o - V_o (2\delta - 1)}{\Delta i_{Lac}} \delta T_{pwm} = \frac{2V_o (1 - \delta)}{\Delta i_{Lac}} \delta T_{pwm} \quad (5.39)$$

Considering  $V_o$  and  $T_{pwm}$  constant, the minimum value of  $L_{ac}$  occurs when  $\delta = 0.5$ :

$$L_{acMIN} = \frac{V_o T_{pwm}}{2 \Delta i_{LacMAX}} \quad (5.40)$$

where  $\Delta i_{LacMAX}$  is obtained based on the desired power factor  $f_p$  which is related to the current THD  $K_{iTHD}$  and power displacement factor  $\cos \varphi_1$  as shown in [2]:

$$\Delta i_{LacMAX} = \frac{I_{1gRMS} \cos \varphi_1}{f_p} \sqrt{12 \left( 1 - \frac{f_p^2}{\cos^2 \varphi_1} \right)} \quad (5.41)$$

By assuming values for  $\cos \varphi_1 = 0.997$ ,  $f_p = 0.995$  and  $V_{gRMS MIN} = 0.9 \times 230$  one can compute the upper and lower limit values of  $L_{ac}$  and consequently choose an appropriate value.

$$\begin{aligned} L_{acMIN} &\leq L_{ac} < L_{acMAX} \\ \Leftrightarrow 75.2 \text{ mH} &\leq L_{ac} < 452.6 \text{ mH} \end{aligned} \quad (5.42)$$

Finally the chosen value for the AC inductor is equal to:

$$L_{ac} = 82.7 \text{ mH} \quad (5.43)$$

### 5.3.3 Active Components of Rectifier

Since the rectifier is composed only by diodes (not active components), the main voltage parameter is the maximum repetitive peak reverse voltage  $V_{RRM}$  which should be:

$$V_{RRM} \geq 2V_o \quad (5.44)$$

The average current in each diode, equation 5.45, is related to the current in the primary of the transformer  $I_{L\lambda}$  which is shown in Figure 5.3 multiplied by the turns ratio  $n$  of the transformer.

$$I_{DAV} = \frac{1}{T_s} \left[ \int_0^{(1-\delta)T_{pwm}} (i_D) dt \right] \quad (5.45)$$

Assuming that the integral can be approximated to a triangle area with a width of  $(1 - \delta) T_{pwm}$  and height of  $2I_{mp}n$ , where  $T_{pwm} = \frac{T_s}{2}$ , we obtain:

$$I_{DAV} = \frac{1}{T_s} \left[ \left( (1 - \delta) \frac{T_s}{2} \times 2I_{mp}n \right) \frac{1}{2} \right] \quad (5.46)$$

On the other hand the root-mean-square current can be computed by:

$$I_{DRMS} = \sqrt{\frac{1}{T_s} \left[ \int_0^{(1-\delta)T_{pwm}} (i_D)^2 dt \right]} \quad (5.47)$$

Assuming that the current between 0 and  $(1 - \delta)T_{pwm}$  can be described by a line equation equal to  $y = \frac{2I_{mp}n}{(1 - \delta)T_{pwm}}t$ , then:

$$I_{DRMS} = \sqrt{\frac{1}{T_s} \left[ \int_0^{(1-\delta)T_{pwm}} \left( \frac{2I_{mp}n}{(1 - \delta)T_{pwm}}t \right)^2 dt \right]} \quad (5.48)$$

The maximum current is:

$$I_{D_{MAX}} = 2I_{mp}n \quad (5.49)$$

### 5.3.4 Active Components of Inverter

The semiconductors used in the half-bridge inverter has the following voltage parameter:

$$V_{DRM} = 2V_o \quad (5.50)$$

Since the current waveform is too complex to be described analytically, we will consider that the average current is related to the output power as described in [2]. Considering that each semiconductor conducts half of the output power we obtain:

$$I_{AV} = \frac{I_o}{2} = \frac{P_o}{2V_o} = \frac{V_{g_{RMS}} I_{1_{RMS}} \cos \varphi_1}{2V_o} \quad (5.51)$$

Using the same principle, the root-mean-square current can be computed as:

$$I_{RMS} = \frac{I_{1_{RMS}}}{\sqrt{2}} = \frac{P_o}{\sqrt{2}V_{g_{RMS}}} = \frac{\eta V_{mp} I_{mp}}{\sqrt{2}V_{g_{RMS}}} \quad (5.52)$$

The maximum current is given by (where  $\Delta i_g$  is computed using (5.41)):

$$I_{MAX} = \sqrt{2}I_{g_{RMS}} + \frac{\Delta i_g}{2} \quad (5.53)$$

Based on the equations described in sub-chapters 5.3.3 and 5.3.4 the semiconductors for the rectifier and the inverter are shown in the Table below.

Table 5.5: Comparison of limit values and chosen semiconductors of the DC-AC converter.

	$D_i$		$Q_i$	
Parameter	Limit Value	Chosen Diode	Limit Value	Chosen MOSFET
$V_{DRM}$ [V]	—	—	820	1700
$V_{RRM}$ [V]	820	1600	—	—
$I_{AV}$ [A]	0.35	1	0.31	5.3
$I_{RMS}$ [A]	0.70	—	0.79	—
$I_{MAX}$ [A]	2.11	30	1.18	6.0

## 5.4 Equivalent Losses

### 5.4.1 Conduction Losses

In order to obtain a more realistic value of the expected "real life" efficiency, it is important to take into account all conduction losses related to equivalent series resistances (ESR),  $R_{DS_{on}}$  or forward voltages drops  $V_F$  between the various components of the power converter. There are many complex models [3] that include parasitic resistances, inductances and capacitances, that can be used to represent each components "real" circuit, but are out of the scope of this thesis. The models shown in Figure 5.10 will be used as a more realistic model approach to the ideal model.

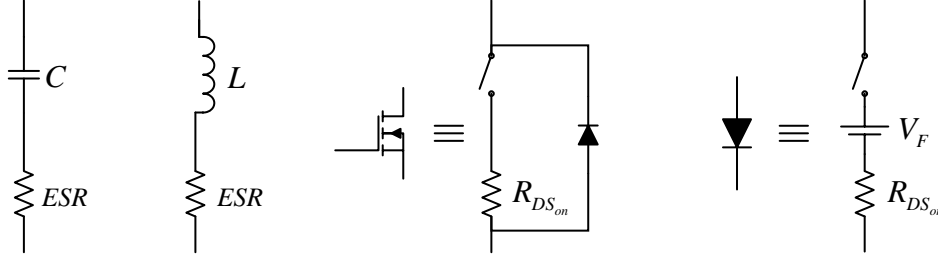


Figure 5.10: Equivalent approximated real life components.

Most of the needed values can be found via the Datasheets presented in Appendix B, except the ESR of the intermediate inductor  $L_{dc}$  which has to be assumed (as done for the HF transformer). By assuming joule losses equal to 1% of PV modules power due to the  $ESR$  of  $L_{dc}$ , is obtained:

$$1\% P_{MP}^r = r_{Ldc} I_{L_{RMS}}^2 \Leftrightarrow r_{Ldc} = \frac{1\% P_{MP}^r}{I_{L_{RMS}}^2} \quad (5.54)$$

where:

$$I_{L_{RMS}} = \sqrt{(I_{MP})^2 + \left(\frac{\Delta I_{MP}}{2\sqrt{3}}\right)^2} \approx I_{MP} \quad (5.55)$$

Due to the high nonlinearity of the diodes current, its equivalent  $R_{DS_{on}}$  resistance, value has to be obtained from its forward current  $I_F$  - forward voltage  $V_F$  curve found in Figure B.7. By using the working currents of  $D_{1,2}$  (Table 5.5) the equivalent  $R_{DS_{on}}$  is obtained as follows:

$$R_{DS_{on}} = \frac{\Delta V_F}{\Delta I_F} = \frac{V_{F_2} - V_{F_1}}{I_{F_2} - I_{F_1}} \approx \frac{V_F(I_{D_{MAX}}) - V_F(I_{D_{AV}})}{I_{D_{MAX}} - I_{D_{AV}}} \quad (5.56)$$

The forward voltage (shown in Fig. 5.10) is equal to  $V_F(I_{D_{AV}})$ .

All equivalent parasitic resistances are listed in Table 5.6 while there equivalent losses can be computed by using the following equation:

$$P_{Joule\ Losses} = ESR \times I_{RMS}^2 \quad (5.57)$$

It is also important to refer that the full-bridge inverter, half-bridge rectifier and half-bridge inverter, only half of their semiconductors contribute to conduction losses, due to the other being turned "off".

The power losses in the transformer iron core can be approximately computed by equation (5.58) if one neglects the voltage drop that occurs at  $R_p$  and  $L_p$ .

$$P_{Losses\ Iron\ Core} = \frac{(V_p)^2}{R_m} = \frac{(nV_o)^2}{R_m} \quad (5.58)$$

Table 5.6: Parasitic resistances responsible for power losses.

	EPR [ $k\Omega$ ]	ESR [ $m\Omega$ ]	$R_{DSon}$ [ $m\Omega$ ]	$P_{Losses}$ [W]
$L_{dc}$	—	35.9	—	2.7
Active-clamp semiconductor	—	—	24	0.4
$C_c$	—	8	—	0.1
Full-bridge inverter	—	—	10	2.6
$R_p$ transformer	—	37.1	—	2.3
$R_s$ transformer	—	2493.7	—	1.2
$R_m$ transformer	4.6	—	—	0.5
Half-bridge rectifier	—	—	1124	0.55
$C_o$	—	5.5	—	—
Half-bridge inverter	—	—	1000	0.6

#### 5.4.2 Switching Losses

Other very important losses that occur in power converters are the switching losses. Switching losses occur when a switching element in a circuit transitions from one state to another. During this transition, neither the current neither the voltage is zero (as occurs when: conducting - no voltage; when turned off - no current), the product of the current and voltage represent a loss that occurs during a short interval of time.

The equations that will be used to compute the switching losses are proposed in [3] and given by:

$$P_{Diode} = V_{RRM} I_{MAX} \frac{t_{rr} - t_s}{2T_s} \quad (5.59)$$

and:

$$P_{MOSFET} = V_{DRM} I_{MAX} \frac{t_r + t_f}{\Lambda T_{pwm}} \quad (5.60)$$

where:

$$\Lambda = \begin{cases} 2, & \text{if: MOSFET has no snubber circuit} \\ 6, & \text{if: MOSFET has a snubber circuit} \end{cases} \quad (5.61)$$

The values  $t_{rr}$ ,  $t_r$  and  $t_f$  can all be found in the Datasheets present in Appendix B, while  $t_s$  can be assumed  $t_s \approx t_{rr}/2$ . In Table 5.7 the various (computed) switching losses can be found.

Table 5.7: Switching power losses.

	Active-clamp semiconductor	Full-bridge inverter	Half-bridge rectifier	Half-bridge inverter
$P_{Losses} [W]$	0.02	0.12	0.33	0.15

### 5.4.3 Efficiency

Based on the losses computed in Tables 5.6 and 5.7, one can compute the total expected efficiency using the following equation:

$$\eta = \frac{P_{mp} - \sum (P_{Losses})}{P_{mp}} \quad (5.62)$$

In Figure 5.11, it is illustrated the decrease in efficiency from the PV module up to the grid, this will be useful later on when sizing the controllers. The maximum expected efficiency should be  $\eta_{Total} \leq 95.7$  since the losses at  $C_o$  and at the snubber circuits were not calculated theoretically, but will be present in the simulation results.

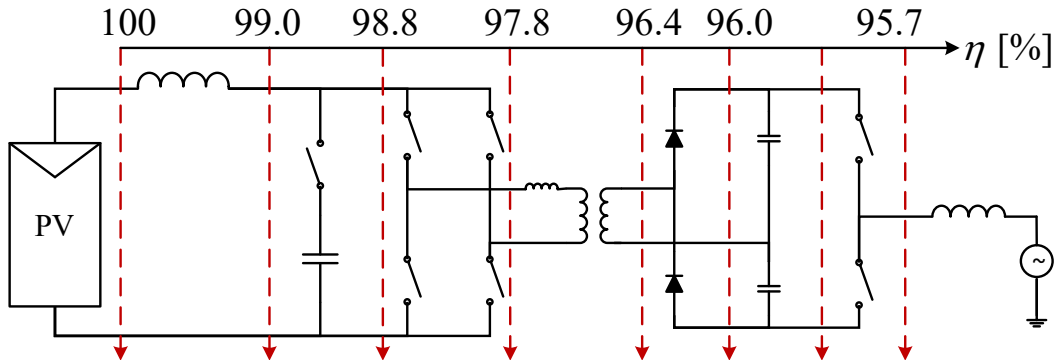


Figure 5.11: Expected evolution of efficiency.

The DC-link and unity power factor control, which will be explained further on, may also have a negative impact on the efficiency due to the expected sinusoidal grid current waveform being distorted by less capable controllers, and there for loss in active power.

## Chapter 6

# Maximum Power Point Tracking Control

### 6.1 Introduction

In order for the AC-module to extract power from the PV module and inject it into the grid it should be equipped with at least two main controllers (Fig. 6.1):

- Maximum Power Point Tracking Control – Responsible for maximizing the power output of the PV module for varying atmospheric conditions.
- Power Control – Responsible for injecting the power from the PV module into the grid while maximizing unitary power factor.

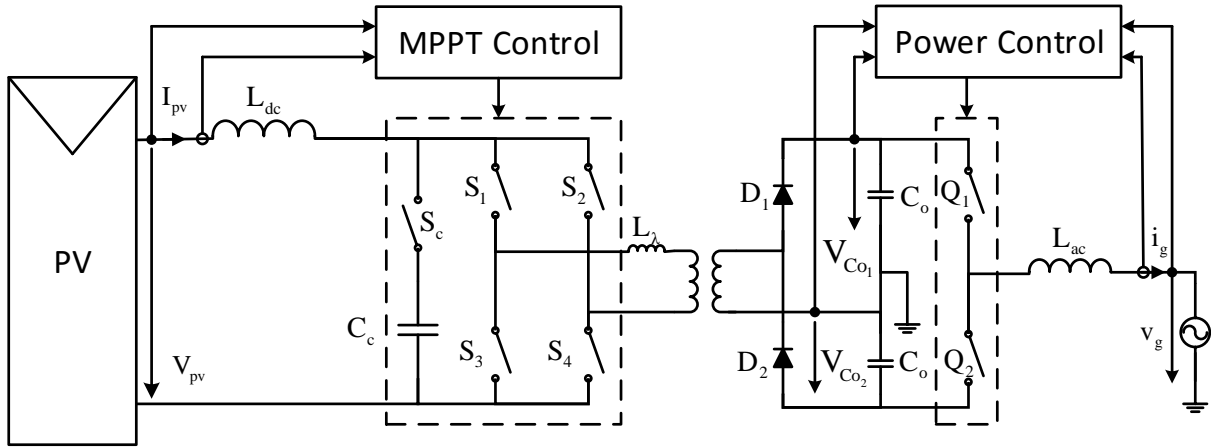


Figure 6.1: Complete AC-module, respective controllers and electrical measurements.

### 6.2 Maximum Power Point Tracking

The MPPT system controls the voltage  $V_{pv}$  and the current  $I_{pv}$  output of the PV module to deliver maximum power, which is an important feature in achieving higher efficiency in photovoltaic power generation systems. As shown in Figure 6.2 the nonlinear relation between current and voltage (of

PV cells) results in a unique global maximum power point which can be achieved by imposing a specific voltage  $V_{mp}$  or current  $I_{mp}$ .

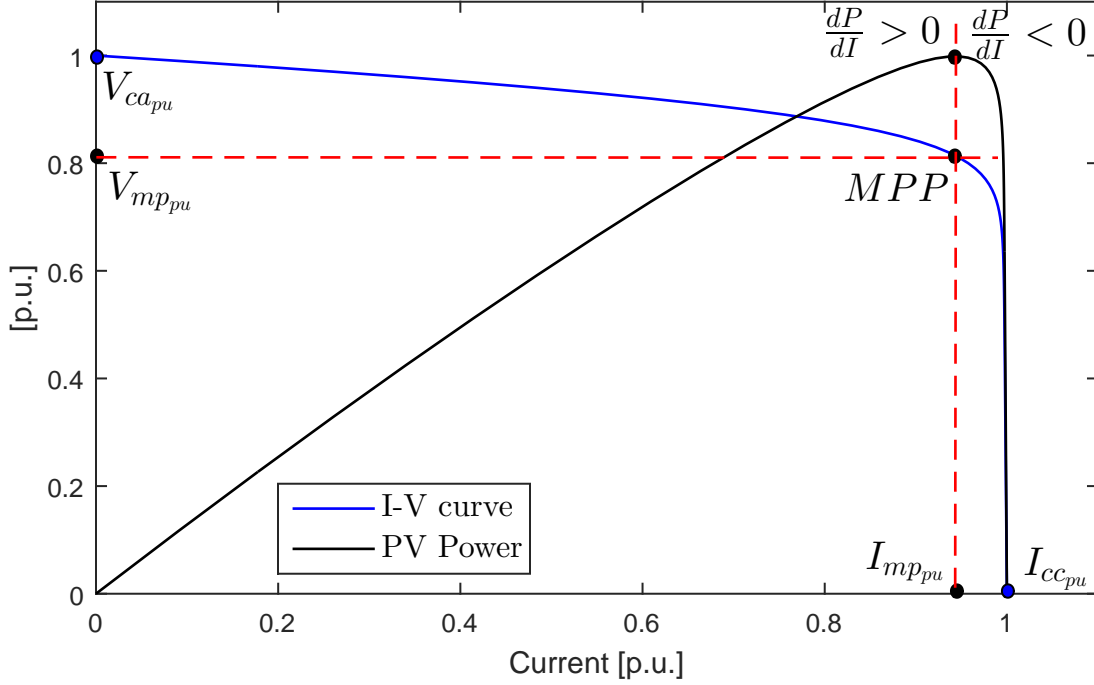


Figure 6.2: Characteristic curves of the PV module.

The premise that will be used to obtain MPPT will be based on the derivative of the power which as evidenced in Figure 6.2 is equal to zero at MPP, monotonously positive before and monotonously negative after (due to the shape of the power curve).

Since the proposed power converter has the current as a state variable, the derivative of the power used will be in order to the current:

$$\frac{dP}{dI} = \frac{d(VI)}{dI} = V \frac{dI}{dI} + I \frac{dV}{dI} = V + I \frac{dV}{dI} \quad (6.1)$$

Assuming that the sampling frequency ( $\Delta t$  - sampling time) of the current and voltage is much higher than the PWM frequency of the power converter, we can assume that the incremental changes in voltage and current are quasi-linear and that the derivative of the power can be given by [4]:

$$\frac{dP}{dI} \approx V(t) + I \frac{V(t) - V(t - \Delta t)}{I(t) - I(t - \Delta t)} \quad (6.2)$$

This method is similar to the common used incremental conductance method, but uses the incremental variation of resistance ( $dV/dI$ ) instead. Compared to the perturb and observe method, it requires more computation by the controller [16], but can track changing conditions more rapidly.

The control objective is to obtain MPPT, which is equivalent to:

$$\frac{dP}{dI} = 0 \quad (6.3)$$

To achieve the control objective (Eq. 6.3) the frequency of the power converter would tend to infinite which is not plausible, meaning that a hysteresis band should be sized to maintain power oscillations close to MPP.

To correctly size the hysteresis band it is useful to analyse the values of  $\frac{dP}{dI}$  close to MPP at different atmospheric conditions as shown in Figures 6.3 and 6.4.

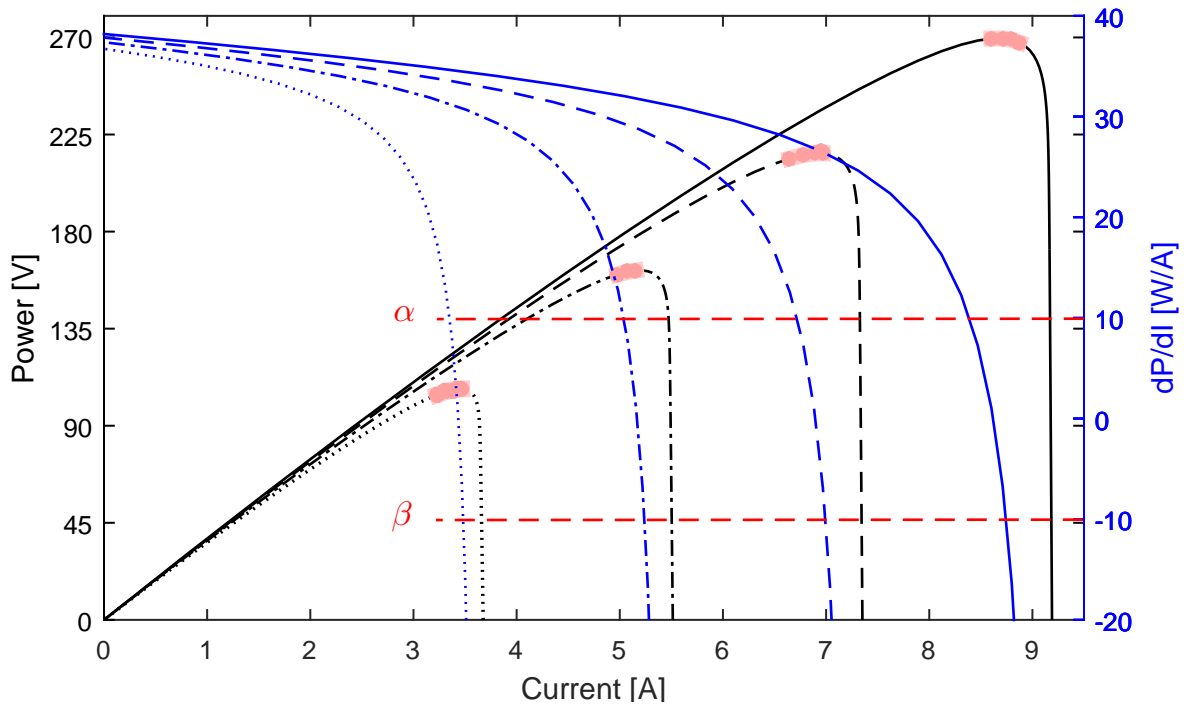


Figure 6.3: Power curve (black) and its derivative (blue) for different levels of irradiance ( $[W/m^2]$ : Solid – 1000, dash – 800, dash-dot – 600 and dot – 400) and constant cell temperature of  $25^\circ C$ . The red dashed line represents the proposed hysteresis band and the highlighted red dots the MPPT oscillation.

Once the hysteresis band  $[\beta, \alpha]$  is defined, where  $\beta < 0$  and  $\alpha > 0$ , the MPPT strategy can be designed based on the sign of the derivative power. The possible scenarios are listed below:

- $\frac{dP}{dI} > \alpha \Rightarrow I \uparrow \Rightarrow$  Current boost mode.
- $\alpha < \frac{dP}{dI} < \beta \Rightarrow I \rightarrow \Rightarrow$  Maintain mode.
- $\frac{dP}{dI} < \beta \Rightarrow I \downarrow \Rightarrow$  Transfer mode.

A fixed hysteresis band control has the disadvantage that the switching frequency varies which is particularly problematic for the proposed converter because of the way the active-clamp capacitor  $C_c$  and the transformer flux inductor  $L_\lambda$  interact (subchapter 5.2.5). To obtain a MPPT with a constant frequency, a PWM control should be used.

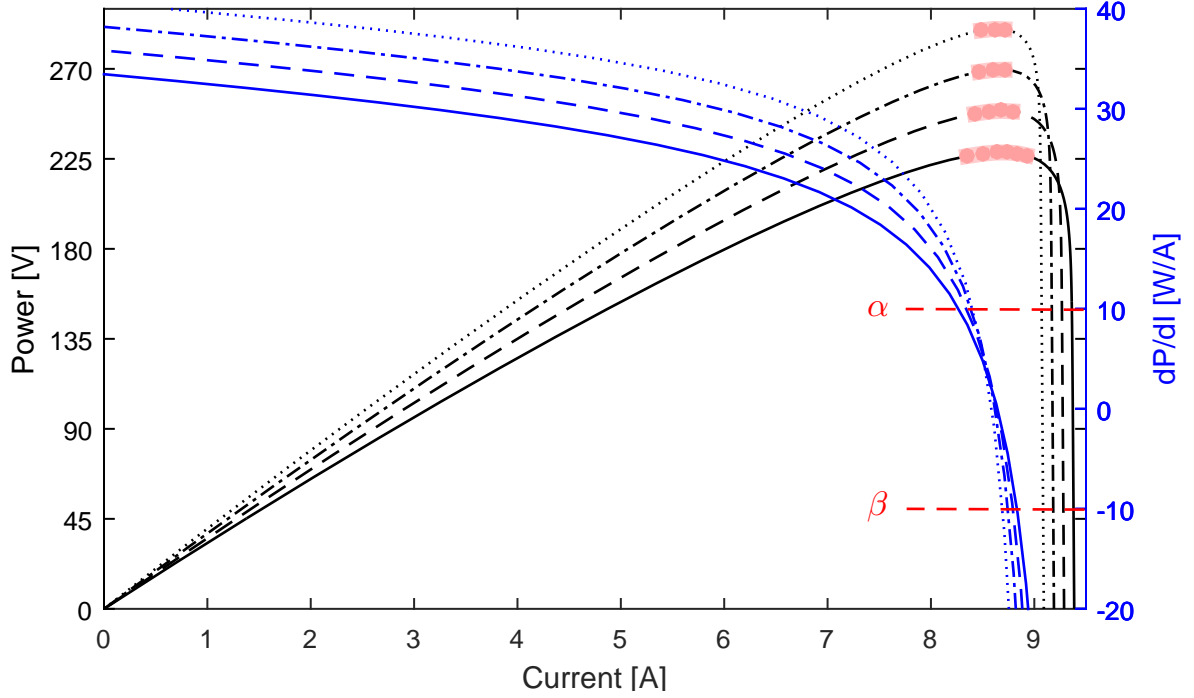


Figure 6.4: Power curve (black) and its derivative (blue) for different levels of cell temperature ( $^{\circ}\text{C}$ ): Solid – 65, dash – 45, dash-dot – 25 and dot – 5) and constant irradiance of  $1000 \text{ W/m}^2$ . The red dashed line represents the proposed hysteresis band and the highlighted red dots the MPPT oscillation.

Since the proposed power converter has the current as a state variable, the reference current  $I_{pv_{ref}} = I_{mp}$  can be tracked by a traditional fixed hysteresis band control (variable frequency) by using the following equation, deduced from Figure 6.1 and given by:

$$L_{dc} \frac{dI_{pv}}{dt} + r_{Ldc} I_{pv} = V_{pv} - \gamma n V_{Co} \quad (6.4)$$

where  $\gamma = 0$  in current boost mode operation,  $\gamma = 1$  in transfer mode operation and  $\gamma$  being controlled by the hysteresis band of the PV power derivative. By applying the Laplace transformation to equation 6.4 we obtain the integrator that allows to track (the virtual current - does not exist)  $I_{mp}$ :

$$I_{mp} = I_{pv_{ref}} = \frac{V_{pv} - \gamma n V_{Co}}{s L_{dc} + r_{Ldc}} \quad (6.5)$$

This value will then be fed into a fixed frequency controller as shown in Figure 6.5:

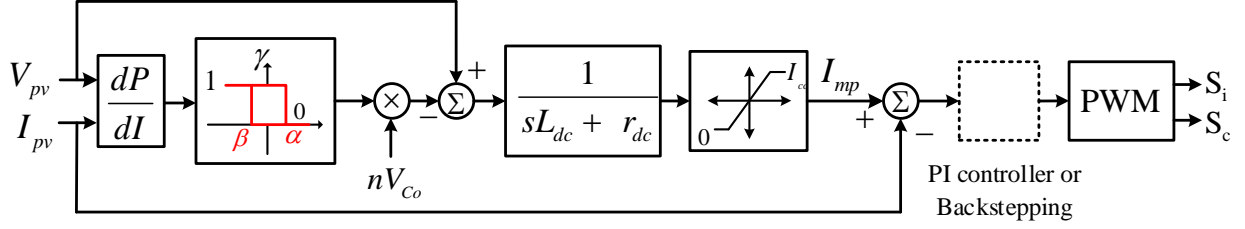


Figure 6.5: Hysteresis band maximum power point tracking control of  $I_{mp}$  (virtual current), which is then fed into a controller that guarantees fixed frequency by computing the necessary duty cycle indirectly through  $u_c$ .

### 6.3 Pulse Width Modulation

As explained in chapter 5.2 the Active-Clamp Full-Bridge Boost Converter uses a PWM technique to achieve an AC voltage with a zero mean value at the transformer. The proposed [4] PWM technique is created based on the flowchart shown in Figure 6.6.

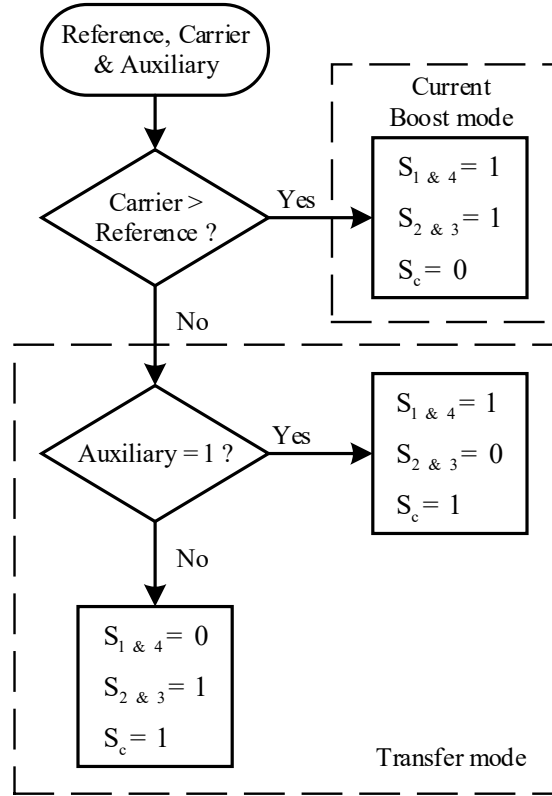


Figure 6.6: 3-Level PWM Flowchart.

Where: the carrier represents a unipolar double-edged triangular modulation; the reference waveform represents a varying quantity from the PI controller or backstepping controller; while the auxiliary waveform is used to create a bipolar waveform at the transformer. The logic circuit of the flowchart is shown in Figure 6.7.

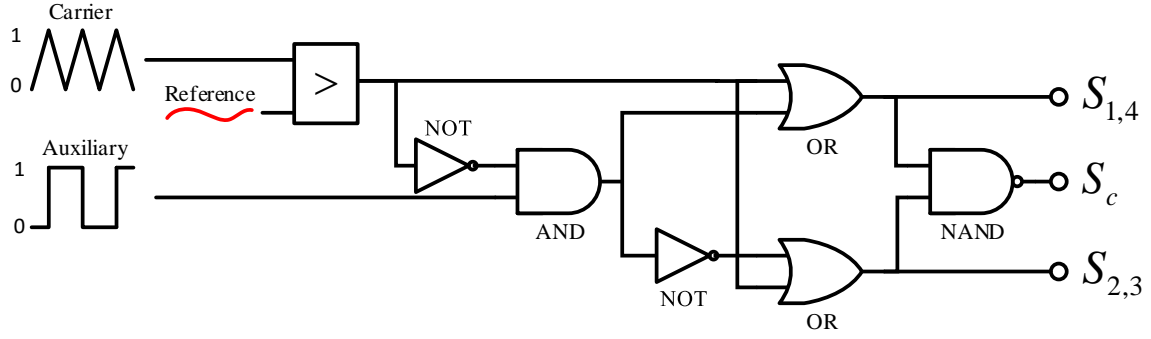


Figure 6.7: 3-Level PWM logic circuit.

The main waveforms that result from the PWM logic circuit are displayed in Figure 6.8, where it is shown that the instantaneous value of the reference waveform determines the value of the duty cycle  $\delta$  (boost of the current  $I_{pv}$ ) and that the waveform applied to the transformer is bipolar as supposed.

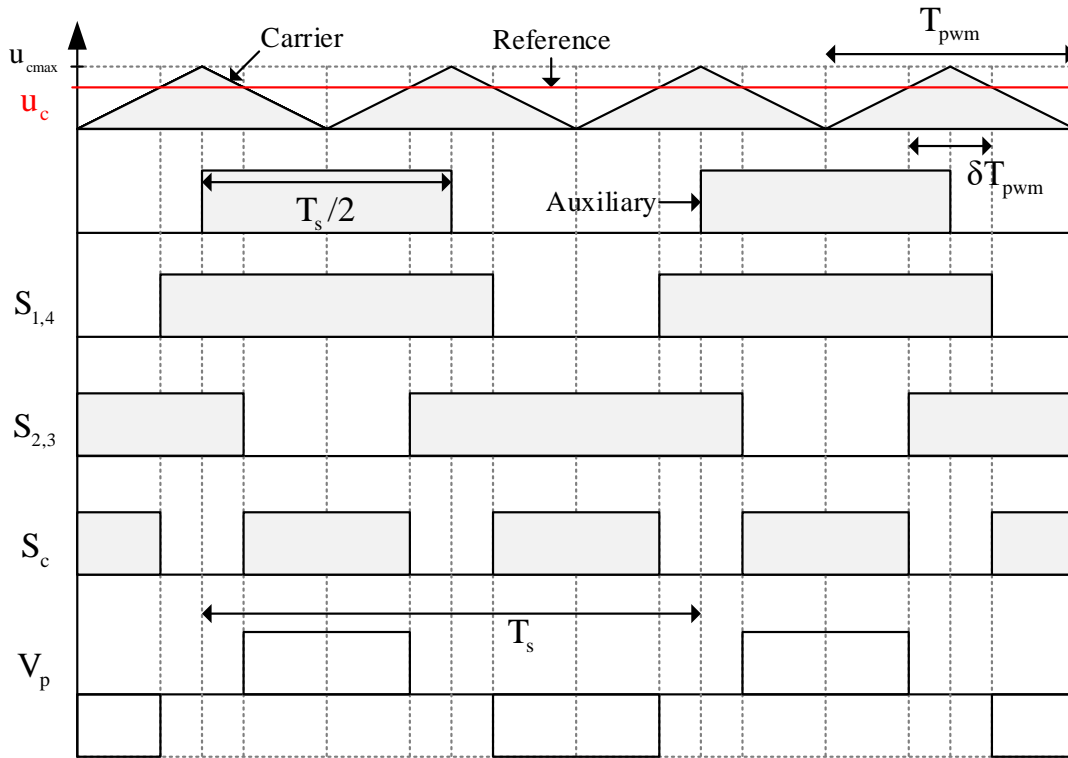


Figure 6.8: 3-Level PWM main waveforms.

The carrier  $r(t)$  has a period equal to  $T_{pwm}$ , a maximum amplitude of  $u_{cmax}$  and is given by:

$$r(t) = \frac{u_{cmax}}{\frac{T_{pwm}}{2}} t \quad (6.6)$$

where if:

$$r \left( t = \frac{(1 - \delta)}{2} T_{pwm} \right) = u_c \quad (6.7)$$

then:

$$\delta = 1 - \frac{u_c}{u_{cmax}} \quad (6.8)$$

## 6.4 Linear PI Controller of MPPT

Instead of equation 6.4 being written in terms of the mode of operation (current boost/transfer), it can be written in terms of its average value, which is related to the duty-cycle  $\delta$  (of the PWM described previously) as follows:

$$L_{dc} \frac{dI_{pv}}{dt} + r_{Ldc} I_{pv} = V_{pv} - nV_{Co}(1 - \delta) \quad (6.9)$$

using the relation (6.8), it is obtained:

$$\begin{aligned} L_{dc} \frac{dI_{pv}}{dt} + r_{Ldc} I_{pv} &= V_{pv} - nV_{Co} \left( \frac{u_c}{u_{cmax}} \right) \\ &= V_{pv} + K_D u_c \end{aligned} \quad (6.10)$$

As explained in [1] the average voltage output of direct converters are dependent on the duty-cycle (which is then related to  $u_c$ ). This means that for small incremental variations the direct converter can be represented using the following transfer function.

$$K_c(s) = \frac{V_{pav}(s)}{u_c(s)} = \frac{\partial V_{pav}}{\partial u_c} e^{-sT_d} = K_D e^{-sT_d} \approx \frac{K_D}{1 + sT_d} \quad (6.11)$$

Where  $K_D$  denotes the equivalent gain and  $T_d$  represents the medium delay of the power converter when reacting to a change of  $u_c$  which for a switching frequency much lower than the reactive components time constant:

$$T_{pwm} \ll \frac{\pi}{\frac{\sqrt{1 - \xi^2}}{\sqrt{L_{dc} n^2 C_o}}} \quad (6.12)$$

can be given by:

$$T_d = \frac{T_{pwm}}{2} \quad (6.13)$$

When a conversion is achieved without an intermediate energy storage stage, the conversion is called direct conversion and is achieved by a direct converter. On the other hand, when a conversion makes use of one or more stages storing energy temporarily, the conversion is called indirect and is achieved by an indirect converter [29]. This means that the Active-Clamp Full-Bridge Boost converter is not categorized as a direct converter, but as an indirect converter since it stores energy temporarily in the inductance  $L_{dc}$ . Figure 6.9 shows the stages of the studied converter.

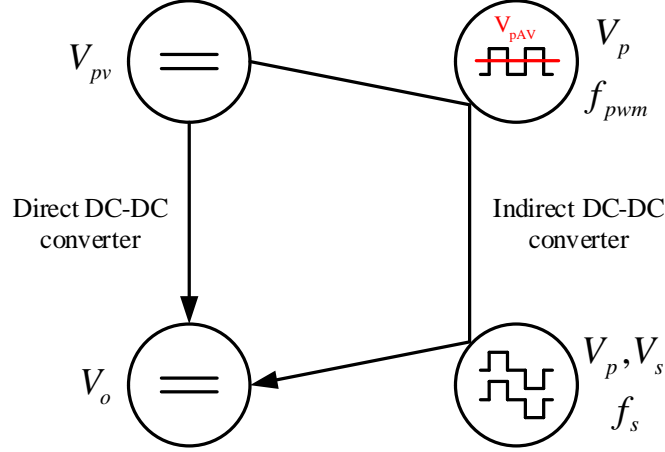


Figure 6.9: Different stages of the Active-Clamp Full-Bridge Boost converter.

Indirect converters are characterized as non-minimum phase systems<sup>1</sup> since their response to a step input has an "undershoot". This means, if the output is initially zero and the steady state output is positive, the output becomes first negative before changing direction and converging to its positive steady state value.

Although non-minimum phase systems require a more careful control design, when their reactive components are correctly sized similar techniques and controllers used for direct converters are applicable to indirect converters [1].

Using equations 6.10 and 6.11 the proportional gain  $K_p$  and integration coefficient  $K_i$  of the PI controller are sized based on the equivalent block diagram of the system in Figure 6.10 with a measurement gain  $\alpha_i$  on the feedback loop.

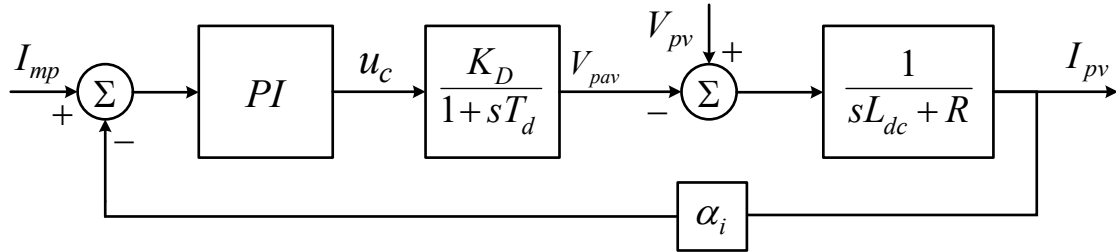


Figure 6.10: Block diagram of the feedback system of the MPPT current control.

Where the proportional integral controller (PI) is given by:

$$C(s) = \frac{1 + sT_z}{sT_p} = \left( \frac{T_z}{T_p} \right) + \left( \frac{1}{T_z} \right) \frac{1}{s} = K_P + K_i \frac{1}{s} \quad (6.14)$$

and  $R$  by equation (6.15), where  $\eta = 0.951$  from Figure 5.11.

<sup>1</sup>Non-minimum phase system: has zeros in the right-hand side of the s-plane.

$$R = r_{Ldc} + R_o \approx r_{Ldc} + \frac{V_o^2}{\eta P_{mp}^r} n^2 \quad (6.15)$$

A methodology to compute the PI gains is proposed in [1] and is described below. The zero of the PI controller should eliminate the low frequency dominant pole of the system as follows:

$$1 + sT_z = 1 + s \left( \frac{L_{dc}}{R} \right) \Rightarrow T_z = \frac{L_{dc}}{R} \quad (6.16)$$

By using the principle of linear superposition with  $V_{pv}(s) = 0$  and by substituting  $T_z$  by its value in 6.16, the closed-loop transfer function of system 6.10 is given by:

$$\begin{aligned} \frac{I_{mp}(s)}{I_{pv}(s)} &= \frac{\frac{1}{sT_p} \frac{K_D}{1 + sT_d} \frac{1}{R} \alpha_i}{1 + \frac{1}{sT_p} \frac{K_D}{1 + sT_d} \frac{1}{R} \alpha_i} \\ &= \frac{\frac{K_D \alpha_i}{T_d T_p R}}{s^2 + s \frac{1}{T_d} + \frac{K_D \alpha_i}{T_d T_p R}} \\ &= \frac{\omega_n^2}{s^2 + 2\xi \omega_n^2 s + \omega_n^2} \end{aligned} \quad (6.17)$$

where  $\xi$  and  $\omega_n$  denote the damping ratio and natural frequency of the system. By Applying the final value theorem to equation 6.17 its shown that the steady state error is equal to zero (since  $i_{pv} = I_{mp}$ ):

$$\lim_{t \rightarrow \infty} \frac{I_{mp}(t)}{I_{pv}(t)} = \lim_{s \rightarrow 0} \frac{I_{mp}(s)}{I_{pv}(s)} = \frac{\omega_n^2}{\omega_n^2} = 1 \quad (6.18)$$

From equation 6.17:

$$\begin{aligned} \omega_n^2 &= \frac{K_D \alpha_i}{T_d T_p R} \\ 2\xi \omega_n^2 &= \frac{1}{T_d} \end{aligned} \quad (6.19)$$

which leads to:

$$T_p = \frac{4\xi^2 K_D T_d \alpha_i}{R} \quad (6.20)$$

At this point the control system design has reached a point where there is only one parameter,  $\xi$ , that can be selected to give the system the best performance. To choose an optimal value  $\xi$  there are a number of performance indexes available based on integral performance measurements.

A common performance index used in 2nd order systems is the ITAE<sup>2</sup> index, which is given by:

$$J_{ITAE} = \int_0^{\infty} |e(t)| t dt \quad (6.21)$$

where:

$$e(t) = I_{mp}(t) - I_{pv}(t) \quad (6.22)$$

The time constants and gains of the PI compensator are displayed in Table 6.1, where a damping ratio equal to  $\xi = \sqrt{2}/2$  is chosen, based on the ITAE index. We will consider a unity measurement gain  $\alpha_i = 1$  since its out of the scope of this thesis to go into further details.

Table 6.1: The time constants and gains of the MPPT current PI controller.

$T_z [\mu s]$	$T_p [\mu s]$	$K_p$	$K_i$
612	-510	-1.20	-1959

#### 6.4.1 PI Controller Stability Analysis

In order to assess the stability and the degree of stability of the controlled system a number of tools will be used. According to [1] to study the stability of this control system, it is not enough to consider the real pole of the power converters equivalent transfer function 6.11 but one must consider at least its second order pole.

$$K_c(s) = \frac{K_D}{1 + sT_d + \frac{s^2}{2!}(T_d)^2 + \dots + \frac{s^n}{n!}(T_d)^n + \dots} \approx \frac{K_D}{1 + sT_d + \frac{s^2}{2!}(T_d)^2} \quad (6.23)$$

A linear system is asymptotically stable if the roots of its characteristic equation (denominator of the closed-loop transfer function) lie in the left-half of the s-plane [35].

By analysing Figure 6.11 its shown that the designed control system is asymptotically stable for small perturbations since the location (shown in orange) of its closed-loop poles are located on the left-half of the s-plane. The poles of the closed-loop transfer function are identical with those of the open-loop transfer function when its open-loop gain is equal to zero (shown in blue).

The frequency domain bode plot of the open-loop and closed-loop transfer functions allow for performance indices and stability degrees to be found. The bode plot of the open-loop transfer function left Figure 6.12 (and/or the Nyquist plot left Figure 6.12), provides the gain and phase stability margins  $A_p$  and  $\varphi_c$  of the control system, which refer to how much the gain can be increased or how much the system can lag (in phase) before it oscillates and becomes installable. The greater the stability margins the less prone the system is to process variations causing instability.

---

<sup>2</sup>ITAE – Integral of time multiplied by the absolute value of error: suitable for non-monotonic responses; regards the permanence of the control error. A control system is better the smaller the value of  $J_{ITAE}$ .

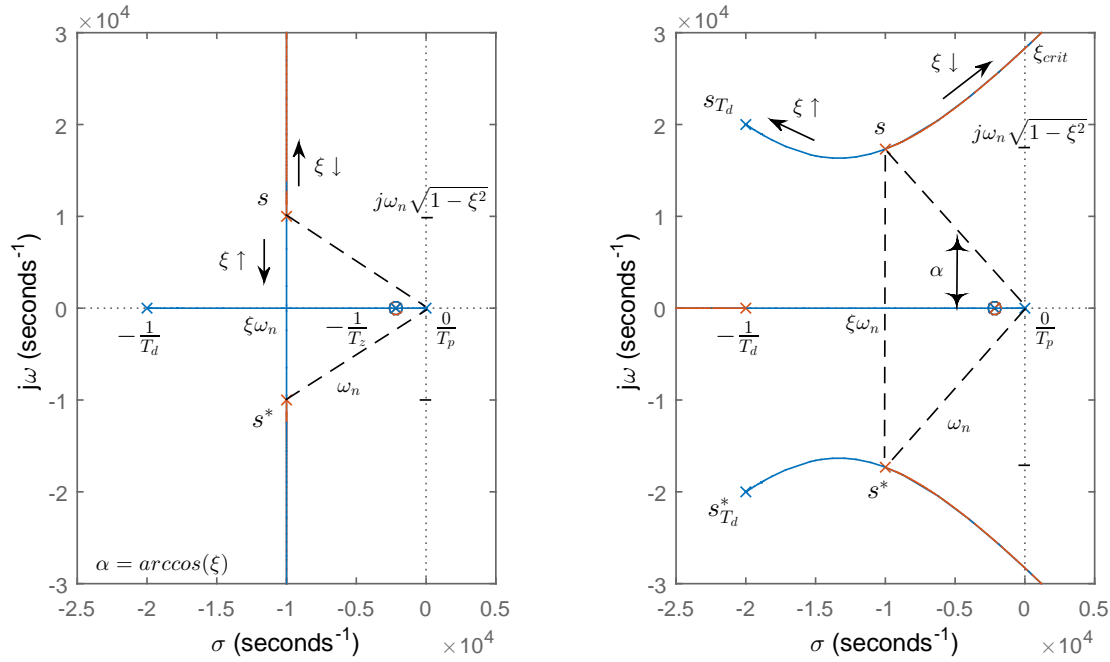


Figure 6.11: Root-Locus of the current control system. Left: Neglecting higher order poles of the power converter. Right: Considering the 2nd order pole, which causes instability for high gains.

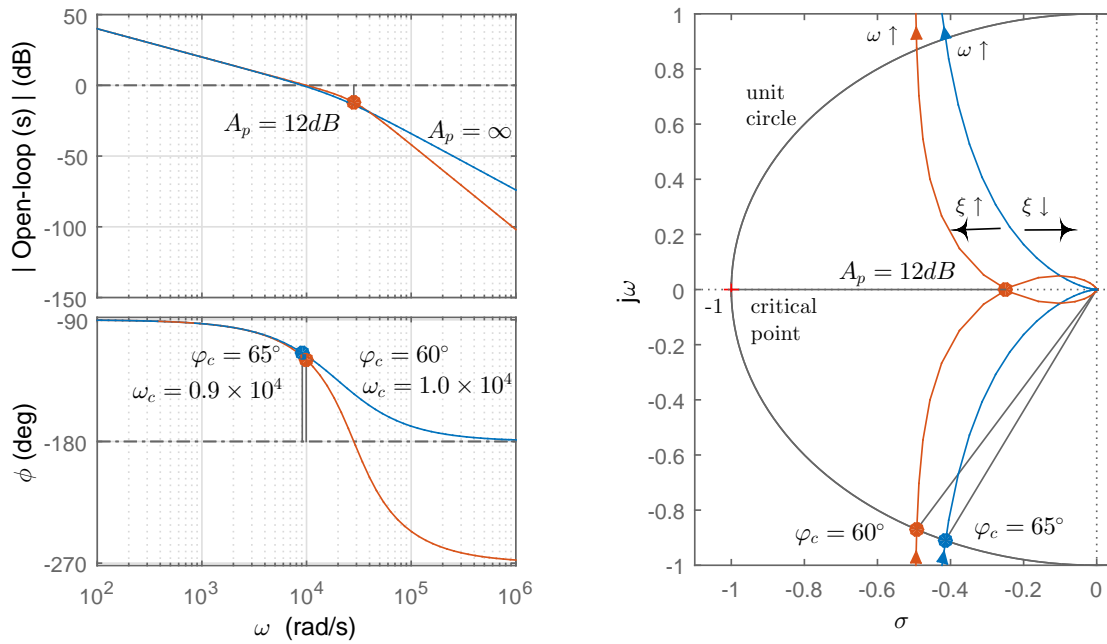


Figure 6.12: Left: Open-loop Bode Plot. Right: Nyquist Plot. The blue line represents the simplified TF while the orange line accounts for the 2nd order TF of the power converter.

Typically, a well damped control system should yield the following characteristics [35], equations 6.24 and 6.25, which are fulfilled by the designed control system (Fig. 6.12):

$$A_p = \begin{cases} -12 \text{ dB} & \text{to} & -20 \text{ dB} & \text{for command response} \\ -3.5 \text{ dB} & \text{to} & -9.5 \text{ dB} & \text{for disturbance response} \end{cases} \quad (6.24)$$

and

$$\varphi_c = \begin{cases} 40^\circ & \text{to} & 60^\circ & \text{for command response} \\ 20^\circ & \text{to} & 50^\circ & \text{for disturbance response} \end{cases} \quad (6.25)$$

The crossover frequency  $\omega_c$  is a measure of the dynamical quality of the control loop. The higher  $\omega_c$ , the higher the bandwidth of the closed-loop and the faster the reaction on command input or disturbances.

The step response shown in the left Figure 6.13 shows that the control system is bounded-input-bounded-output stable and that it contains a null steady state error as expected (Eq. 6.18). The control system also has an acceptable amount of maximum overshoot  $M_p < 10\%$ , a rise-time  $t_r \approx 1 \times T_{pwm}$  and a settling-time  $t_\epsilon \approx 4 \times T_{pwm}$  which are too acceptable values.

In control engineering is it common to characterize how robust the closed-loop is to process variations simultaneously in gain and phase using the sensitivity transfer function  $S(j\omega)$ . The bode plot of the sensitivity transfer function is shown in the right Figure 6.13.

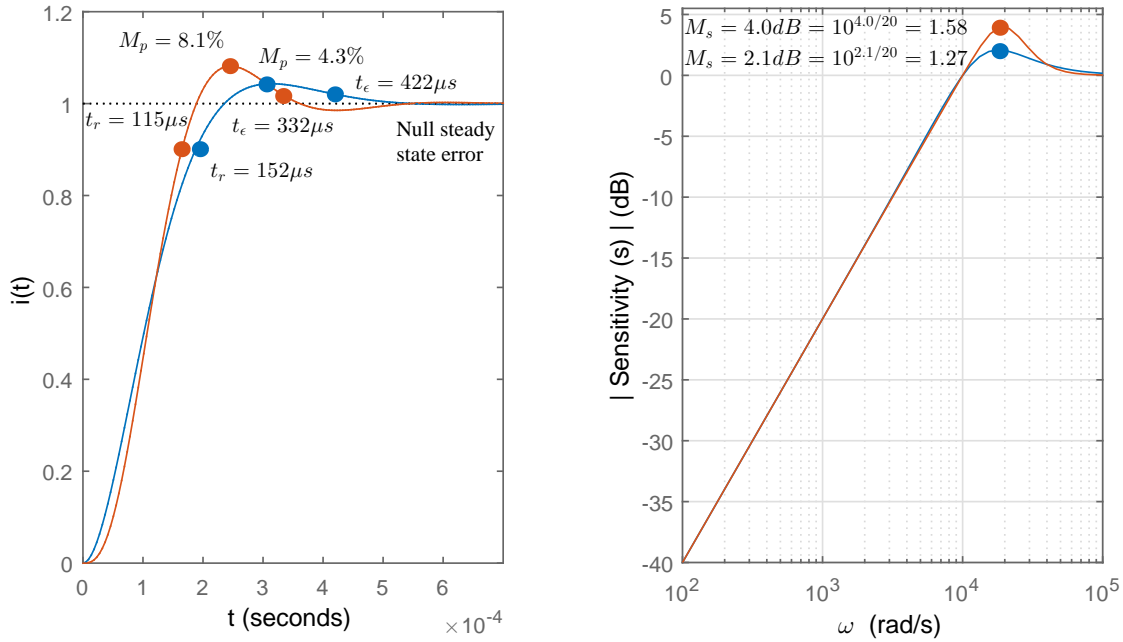


Figure 6.13: Left: Closed-loop step response. Right: Sensitivity bode Plot. The blue line represents the simplified TF while the orange line accounts for the 2nd order TF of the power converter.

The sensitivity transfer function is obtained by considering that all process variations can be simplified and approximated to a measurement noise. By tracing the sensitivity transfer function bode plot, the maximum sensitivity  $M_s$  (Eq. 6.26) of the closed-loop to process variation can be computed.

$$M_s = \max_{0 \leq \omega < \infty} |S(j\omega)| = \max_{0 \leq \omega < \infty} \left| \frac{1}{1 + G_{open-loop}(j\omega)} \right| \quad (6.26)$$

It is important that the largest value of the sensitivity function to be limited and it is common to require that its maximum value  $M_s$  be in a range between 1.3 to 2, which is fulfilled by the designed control system (right Fig. 6.13).

### 6.4.2 Anti-Windup

The PWM described in subsection 6.3 compares a triangular carrier with minimum and maximum values  $u_{cmin} = 0$  and  $u_{cmax} = 1$  to a reference waveform which too must be limited between those values. To limit the reference waveform generated by the PI controller its output should have a saturation block (nonlinear discontinuous element).

When a reference change  $I_{mp}$  is applied, the output  $u_c$  of the PI controller might attain of the limits during the transient response. In this case the system operates as in the open-loop case, since the system's input is at its maximum (or minimum) limit, independently of the system output value. The error decreases slower than the ideal case (without saturation) and therefore the integral term becomes large (it winds up). Thus, even when the system variable is equal to the reference waveform, the controller will still be saturated due to the integral term [30].

There are many methods used to avoid integrator windup. The approach utilized is the anti-windup based on Back-Calculation proposed by [1] which is illustrated in Figure 6.14. The system has an extra feedback path that is generated by measuring the actual PI controller output and the output of a mathematical model of the saturating block, and forming an error waveform ( $e_w$ ) as the difference between the output of the PI controller ( $u'_c$ ) and the saturating block output ( $u_c$ ).

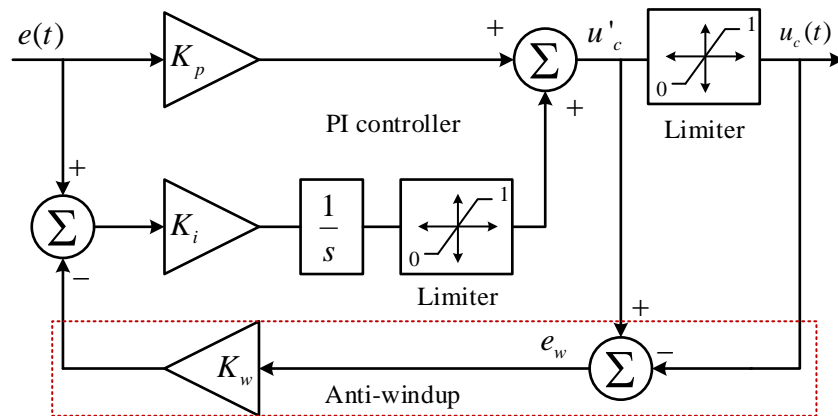


Figure 6.14: PI controller with a saturation block and an extra feedback loop used for Anti-Windup (based on Back-Calculation).

The quantity  $e_w$  is zero when there is no saturation, meaning that the extra feedback loop has no effect on the system. When the actuator saturates, the quantity  $e_w$  is feedback to the integrator through a gain  $K_w$  in such a way that  $e_w$  goes towards zero. This implies that controller output is kept close to the saturation limit  $u_{cmax}$ .

The rate at which the controller output is reset is governed by the feedback gain,  $K_w$ , a large value of  $K_w$  gives a short reset time. The parameter  $K_w$  can, however, not be too large because measurement error can then cause an undesirable reset. The anti-windup Back-Calculation proposed by [1] suggests that the minimum error of the additional feedback loop should be greater than the limit error  $e(t) = E_{lim}$  that leads to integral windup:

$$\min[ K_w e_w ] > E_{lim} \quad (6.27)$$

with an interval of values  $K_w$  given by (6.28) for PI controllers.

$$0 < K_w < \sqrt{K_p K_i} \quad (6.28)$$

## 6.5 Nonlinear Backstepping Control of MPPT

An alternative way to compute the duty-cycle  $\delta = 1 - u_c$  is the nonlinear backstepping approach. Having described the design procedures in the framework of backstepping control (subchapter 3.2.2), one can now apply them the current control of the reference value provided by the MPPT controller.

The first step should be to find the state variables  $\underline{x}$ , the control input  $u$  and construct the systems strict-feedback form. The one and only state variable of the full-bridge boost inverter is the current  $i_{pv}$  of the  $L_{dc}$  inductor, since capacitor  $C_c$  does not affect the current as explained before. The modulation used to control the inverter is a 3-level PWM with  $u_{cmin} = 0$  and  $u_{cmax} = +1$  that receives a reference  $u_c$  responsible for generating the duty cycle as shown in Figure 6.8. This means that  $u_c$  is the control input  $u$  of the nonlinear inverter system.

$$\begin{aligned} L_{dc} \frac{d}{dt} (I_{pv}) &= V_{pv} - r_{Ldc} I_{pv} - nV_o(1 - \delta) \\ \Leftrightarrow L_{dc} \frac{d}{dt} (I_{pv}) &= V_{pv} - r_{Ldc} I_{pv} - nV_o u_c \\ \Leftrightarrow \frac{d}{dt} (I_{pv}) &= f_1 + g_1 u_c \end{aligned} \quad (6.29)$$

The backstepping control algorithm is applicable to a strict-feedback system of any order, including one. This means that the systems strict-feedback form is given by:

$$\frac{d}{dt} (I_{pv}) = f_1 + g_1 u_c \quad (6.30)$$

with  $\underline{x} = (x_1) = (I_{pv}) \in \mathbb{R}^1$  and  $g_i \neq 0 \ \forall i \in \{1\}$ .

The process starts by defining the tracking error coordinates:

$$z_1 = \epsilon_{I_{pv}} = I_{pv} - I_{mp} \quad (6.31)$$

With the change of coordinates (6.31) it is now possible to build positive quadratic control Lyapunov function of  $\epsilon_{I_{pv}}$  as:

$$V_1 = \frac{1}{2} z_1^2 = \frac{1}{2} (\epsilon_{I_{pv}})^2 \quad (6.32)$$

The time derivative of (6.32) is given by:

$$\frac{d}{dt} V_1 = z_1 \dot{z}_1 = \epsilon_{I_{pv}} \frac{d \epsilon_{I_{pv}}}{dt} \quad (6.33)$$

where the dynamics of the error coordinate is:

$$\begin{aligned} \dot{z}_1 &= \dot{x}_1 - \dot{y}_r \\ \Leftrightarrow \frac{d \epsilon_{I_{pv}}}{dt} &= \frac{d}{dt} I_{pv} - \frac{d}{dt} I_{mp} \\ \Leftrightarrow \frac{d \epsilon_{I_{pv}}}{dt} &= f_1 + g_1 u_c - \frac{d}{dt} I_{mp} \end{aligned} \quad (6.34)$$

Substituting (6.34) in (6.33) and by the application of LaSalle-Yoshizawa Theorem (3.4), it is obtained:

$$\frac{d V_1}{dt} = \epsilon_{I_{pv}} \left[ f_1 + g_1 u_c - \frac{d}{dt} (I_{mp}) \right] = -c_1 (\epsilon_{I_{pv}})^2 \quad (6.35)$$

After some manipulation, the control input  $u$  is obtained:

$$u = u_c = \frac{1}{g_1} \left( -c_1 \epsilon_{I_{pv}} - f_1 + \frac{d}{dt} I_{mp} \right), \quad c_1 > 0 \quad (6.36)$$

## Chapter 7

# DC-AC Inverter Power Control

As explained in Chapter 6 the inverter is responsible for injecting the power produced by the PV module into the grid with near unity power factor. In order for the inverter to work correctly the voltage at capacitors  $C_o$  should be maintained at a higher level than the grid voltage to be able to impose the direction of the power flow through the inductor  $L_{ac}$ . This implies that the reference voltage should satisfy the following principle:

$$V_{oREF} > \sqrt{2}V_{gmax} \quad (7.1)$$

To guarantee that the voltage at the capacitors  $C_o$  are maintained at  $V_{oREF}$  while simultaneously injecting power into the grid with near unity power factor, two controllers should be devised (i.e. an outer voltage loop and inner current loop).

The control of the  $1\phi$  half-bridge inverter (Fig. 5.7) is more challenging than the control of  $1\phi$  full-bridge inverter since there are two capacitors to maintain at a reference voltage  $V_{oREF}$ , and the AC current must be shaped, while only having two degree of freedom (the AC current root mean square value and the semiconductors  $Q_1$  or  $Q_2$  duty cycle).

### 7.1 Linear PI Controller of DC-Link

Applying Kirchhoff's current law (KCL) to each capacitor of the DC-link (Fig. 5.7), it is obtained:

$$C_{o1} \frac{dV_{o1}}{dt} = i_{D1} - \gamma_g i_g \quad (7.2)$$

$$C_{o2} \frac{dV_{o2}}{dt} = i_{D2} - (1 - \gamma_g) i_g \quad (7.3)$$

where  $\gamma_g$  is given by:

$$\gamma_g = \begin{cases} 1, & \text{when : } Q_1 \text{ on} \\ 0, & \text{when : } Q_2 \text{ off} \end{cases} \quad (7.4)$$

Due to the fact that there are two degrees of freedom ( $i_g$ ;  $\gamma_g$ ), the control of voltages  $V_{o1}$  and  $V_{o2}$  has to be done indirectly by controlling the  $i_g$  root mean square value (or amplitude) [1], since the fast time varying  $\gamma_g$  is used to shape the sinusoidal shape AC current. The principle premise used to obtain voltage control of the DC-link capacitors is based on the power balance between the average power from the half-bridge rectifier and the average power injected into the grid. This means that it is necessary to regulate the RMS value  $i_{g_{RMS}}$  in order to maintain voltages  $V_{o1} \approx V_{o2} = V_{o_{REF}}$ . This is possible because the dynamic of  $V_o$  is much slower when compared to the current  $i_g$  dynamic.

Its important to remember that although there may be an equivalence in the average powers ( $P_{pv_{AV}} \approx P_{g_{AV}}$ ), it is not possible to equal the instantaneous powers ( $p_{pv}(t) \neq p_g(t)$ ). This means that the excess instantaneous power is stored in the DC-link capacitors.

The electric current  $i_g$  must have an approximately sinusoidal waveform. To control the power balance its fundamental RMS value may be used. Considering near unity power factor and electric power conservation:

$$\begin{aligned} P_g &= \eta P_o \\ \Leftrightarrow V_{g_{RMS}} I_{g_{RMS}} &= \eta V_o I_o \\ \Leftrightarrow I_{g_{RMS}} &= \frac{\eta V_o}{V_{g_{RMS}}} I_o \end{aligned} \quad (7.5)$$

If we assume that  $V_o$  average value is maintained constant and that the grids RMS voltage  $V_{g_{RMS}}$  is equally constant, the current  $I_{g_{RMS}}$  from equation (7.5) can be considered a function of  $I_o$  with a gain  $G$  as shown below:

$$I_{g_{RMS}} = \frac{\eta V_o}{V_{g_{RMS}}} I_o = G I_o \quad (7.6)$$

By assuming  $C_{o1} \approx C_{o2} = C_o$  and adding equations (7.2) and (7.3) we obtain the energy balance at the DC-AC inverter:

$$2 C_o \frac{d V_o}{dt} = (i_{D1} + i_{D2}) - i_g \quad (7.7)$$

Taking into account equation (7.6) and applying the Laplace transformation to (7.7) it is obtained:

$$\begin{aligned} s 2 C_o V_o(s) &= [I_{D1}(s) + I_{D2}(s)] - G I_o(s) \\ \Leftrightarrow V_o(s) &= \frac{[I_{D1}(s) + I_{D2}(s)] - G I_o(s)}{s 2 C_o} \end{aligned} \quad (7.8)$$

Using equation (7.8) and assuming that the inverter has a delay equal to  $T_{dV}$  the control gains of the PI controller responsible for controlling the voltage of the DC-link capacitors can be computed, based on the block diagram shown in Figure 7.1.

$$T_{dV} = \pi \frac{\sqrt{L_{ac} C_o}}{\sqrt{1 - \xi^2}} \quad (7.9)$$

Where the proportional integral controller (PI) is given by:

$$C_v(s) = \frac{1 + s T_{zV}}{s T_{pV}} = \left( \frac{T_{zV}}{T_{pV}} \right) + \left( \frac{1}{T_{zV}} \right) \frac{1}{s} = K_{PV} + K_{iV} \frac{1}{s} \quad (7.10)$$

By using the principle of linear superposition with  $I_{D1}(s) = I_{D2}(s) = 0$ , the closed-loop transfer

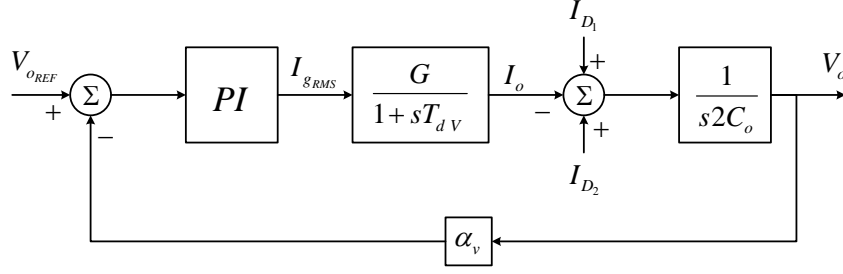


Figure 7.1: Block diagram of linearised voltage control.

function of system 7.1 is given by:

$$\frac{V_{oREF}(s)}{V_o(s)} = \frac{\frac{1+sT_{zV}}{sT_{pV}} \frac{-G}{1+sT_{dV}} \frac{1}{s2C_o} \alpha_v}{1 + \frac{1+sT_{zV}}{sT_{pV}} \frac{-G}{1+sT_{dV}} \frac{1}{s2C_o} \alpha_v} \quad (7.11)$$

After some computation of (7.11) we obtain:

$$\frac{V_{oREF}(s)}{V_o(s)} = \frac{(1+sT_{zV})}{s^3 \frac{-T_{pV}2C_oT_{dV}}{G\alpha_v} + s^2 \frac{-T_p2C_o}{G\alpha_v} + sT_{zV} + 1} \quad (7.12)$$

In order to compute  $T_{pV}$  and  $T_{zV}$  one can apply the rule  $b_k^2 = a b_{k-1} b_{k+1}$  (with  $a \neq 0$  and  $b_k$  being the coefficients) to the denominator of polynomial (7.12), resulting in:

$$\begin{cases} \left( -\frac{T_{pV}2C_o}{G\alpha_v} \right)^2 = -a \frac{T_{pV}C_o2T_{dV}}{G\alpha_v} T_{zV} \\ (T_{zV})^2 = -a \frac{T_{pV}2C_o}{G\alpha_v} 1 \end{cases} \Leftrightarrow \begin{cases} T_{pV} = -\frac{a^3 T_{dV}^2 G\alpha_v}{2C_o} \\ T_{zV} = a^2 T_{dV} \end{cases} \quad (7.13)$$

By substituting values  $T_{pV}$  and  $T_{zV}$  into (7.12) we obtain that the closed-loop transfer function of the voltage, as a function of  $a$  and  $T_{dV}$ :

$$\begin{aligned} \frac{V_{oREF}(s)}{V_o(s)} &= \frac{(1+s a^2 T_{dV})}{s^3 a^3 T_{dV}^3 + s^2 a^3 T_{dV}^2 + s a^2 T_{dV} + 1} \\ &= \frac{(1+s a^2 T_{dV})}{(1+s a T_{dV}) (s^2 a^2 T_{dV}^2 + s (a^2 - a) T_{dV} + 1)} \end{aligned} \quad (7.14)$$

which results in the following real zero and real pole:

$$\text{real zero: } -\frac{1}{a^2 T_{dV}} \quad (7.15)$$

$$\text{real pole: } -\frac{1}{a T_{dV}} = -\omega_n \quad (7.16)$$

and complex poles:

$$\begin{aligned} \text{compl. poles: } -\frac{1}{aT_{dv}} \left[ -\frac{a-1}{2} \pm \sqrt{\left(\frac{a-1}{2}\right)^2 - 1} \right] &= \omega_n \left[ -\xi \pm \sqrt{\xi^2 - 1} \right] \\ &= -\omega_n \xi \pm \omega_n \sqrt{\xi^2 - 1} \end{aligned} \quad (7.17)$$

As well known, the poles of a closed loop should have a negative real part in order for the system's transient response to reach zero (i.e. stability). Another common notion is that the damping factor  $\xi$  should belong to the interval  $\xi \in ]0; 1]$ . As a reminder the following terms are used to describe a transient response of a system:

- $\xi \rightarrow 0$ : *Undamped* - Simple harmonic oscillator.
- $\xi < 1$ : *Underdamped* - The solution is a decaying exponential combined with an oscillatory portion.
- $\xi = 1$ : *Critically damped* - The border between the overdamped and underdamped cases, and is referred to as critically damped.
- $\xi > 1$ : *Overdamped* - The solution is simply a decaying exponential with no oscillation.

Based on equation (7.17) and the previous explanation, it's possible to compute the value of  $a$  by choosing a damping factor equal to  $\xi = 0.7 = \frac{a-1}{2} \Leftrightarrow a = 2.4$ , which results in:

Table 7.1: The time constants and gains of the DC-Link voltage PI controller.

$T_{zv} [ms]$	$T_{pv} [\mu s]$	$K_{pv}$	$K_{iv}$
50.7	6.5303	0.0078	0.1531

### 7.1.1 PI Controller Stability Analysis

In order to assess the stability of the system the root-locus of the open and closed-loop transfer function of the block diagram of Figure 7.1 will be performed (Fig. 7.2) as well as the step response of the closed-loop transfer function (Fig. 7.3). The gain and phase margins will not be studied due to the fact that the voltage control is the outer-loop part of the embedded loops.

By analysing Figure 7.2 its shown that the designed control system is asymptotically stable for small perturbations since the location (shown in orange) of its closed-loop poles are located on the left-half of the s-plane. The poles of the closed-loop transfer function are identical with those of the open-loop transfer function when its open-loop gain is equal to zero (shown in blue).

The step response shown in Figure 7.3 shows that the control system is bounded-input-bounded-output stable and that it contains a null steady state error.

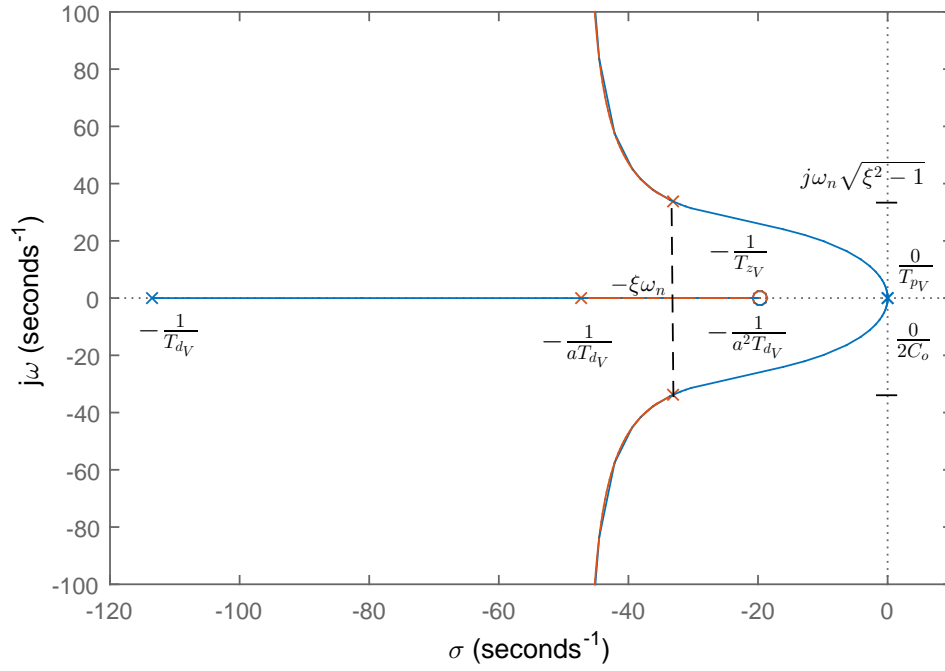


Figure 7.2: Root Locus of DC-Link voltage control.

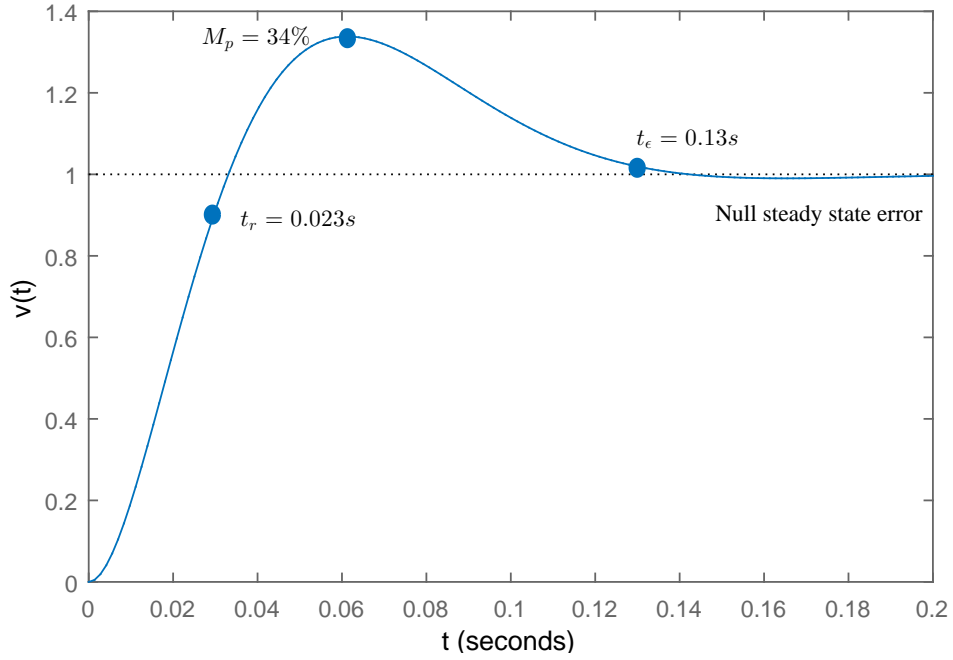


Figure 7.3: Step Response of DC-Link voltage control.

### 7.1.2 Near Unity Power Factor Control

Once the RMS value of the grid current  $I_{g_{RMS}}$  is computed (value provided by the  $PI$  controller of the DC-link voltage), it will be necessary to guarantee that the inverter injects the near sinusoidal current into the grid at near unity power factor. A common used controller is the hysteresis band current control.

The principle of hysteresis current control is very simple. The current controller controls the grid current by forcing it to follow a reference which is constructed based on  $I_{g_{RMS}}$  and on the grid voltage  $v_g$  shape, frequency  $\omega$  and phase  $\theta_v$ , as shown below:

$$i_{g_{REF}} = \sqrt{2}I_{g_{RMS}} \sin(\omega t + \theta_v) \quad (7.18)$$

In order to control the grid current  $i_g$  it is necessary to know how its dynamic is affected by the inverter (actuator):

$$\begin{aligned} L_{ac} \frac{d}{dt}(i_g) &= v_{pwm} - v_g \\ \Leftrightarrow L_{ac} \frac{d}{dt}(i_g) &= \gamma_{pwm} v_o - v_g \end{aligned} \quad (7.19)$$

where  $\gamma_{pwm}$  is given by:

$$\gamma_{pwm} = \begin{cases} 1, & \text{when : } Q_1 \text{ on} \\ -1, & \text{when : } Q_2 \text{ off} \end{cases} \quad (7.20)$$

This means that if:

$$\gamma_{pwm} = \begin{cases} 1, & \Rightarrow \frac{di_g}{dt} > 0 \\ -1, & \Rightarrow \frac{di_g}{dt} < 0 \end{cases} \quad (7.21)$$

The switching action  $\gamma_{pwm}$  of the inverter keeps the current  $i_g$  within the hysteresis band  $[-\epsilon_{i_g}; \epsilon_{i_g}]$ , by using theorem 3.2.1 the following control principle can be used to achieve tracking of  $i_{g_{REF}}$ :

$$\begin{aligned} e_{i_g} > +\epsilon_{i_g} &\Rightarrow i_{g_{REF}} > i_g \Rightarrow i_g \uparrow \Rightarrow \frac{di_g}{dt} > 0 \Rightarrow \gamma_{pwm} = 1 \\ e_{i_g} < -\epsilon_{i_g} &\Rightarrow i_{g_{REF}} < i_g \Rightarrow i_g \downarrow \Rightarrow \frac{di_g}{dt} < 0 \Rightarrow \gamma_{pwm} = -1 \end{aligned} \quad (7.22)$$

where:

$$e_{i_g} = i_{g_{REF}} - i_g \quad (7.23)$$

The block diagram of the previous control is shown in Figure 7.5 while its resulting behaviour is illustrated in Figure 7.4.

When the grid current reaches the lower hysteresis limit, the inverter switches its state to produce an increasing grid current. On the other hand, a decreasing grid current is produced when the current reaches the upper hysteresis limit. The hysteresis controller output current waveform is similar to that of a two-level PWM.

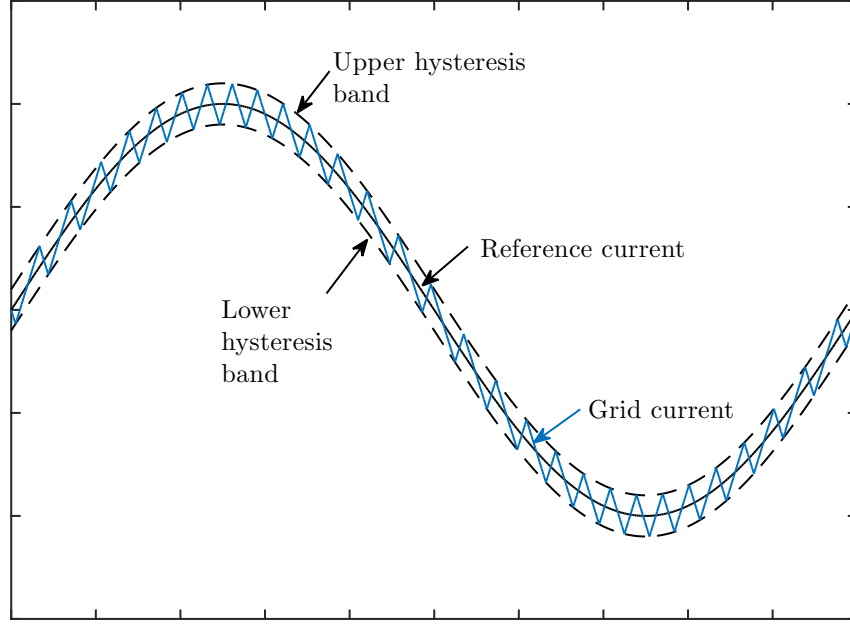


Figure 7.4: Illustration of the current ripple and respective control by the hysteresis upper and lower limits.

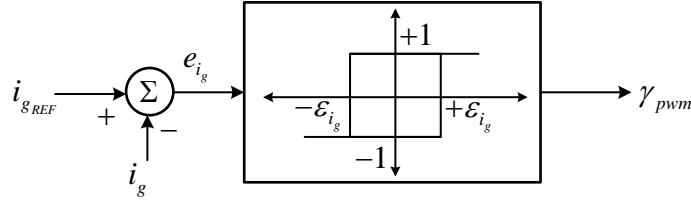


Figure 7.5: Hysteresis band nonlinear control.

## 7.2 Nonlinear Backstepping Control of DC-Link

Having described the design procedures in the framework of backstepping control (subchapter 3.2.2), one can now apply them to the  $1\phi$  half-bridge inverter model. The approach used will be similar to the one used in [41].

The first step should be to find the state variables  $\underline{x}$ , the control input  $u$  and construct the systems strict-feedback form. The state variables of the output inverter are voltages  $V_{o1}$  and  $V_{o2}$  at each half-bridge capacitor and the output current  $i_g$  of the  $L_{ac}$  inductor. The modulation used to control the inverter is a 2-level PWM that receives a sinusoidal modulation index  $\beta$  as an input. This means that  $\beta$  is the control input  $u$  of the nonlinear inverter system.

The energy transfer through the DC-AC converter, considering it is conservative and operates at unity power factor is given by:

$$\frac{d}{dt} \left( \frac{1}{2} C_{o1} V_{o1}^2 \right) + \frac{d}{dt} \left( \frac{1}{2} C_{o2} V_{o2}^2 \right) = i_{D1} V_{o1} + i_{D2} V_{o2} - i_g v_g \quad (7.24)$$

Assuming that  $C_{o_1} \approx C_{o_2} = C_o$ :

$$V_{o_1} \approx V_{o_2} = V_o \quad \Rightarrow \quad V_o = \frac{V_{o_1} + V_{o_2}}{2} \quad (7.25)$$

The stabilizing function must relate the system energy balance to the amplitude value  $I_g$  to separate the converter dynamics [41]. This means that the control parameter  $I_{g_{RMS}}$  for the inner current loop sinusoidal reference current (in phase with  $v_g$ ) is obtained based on:

$$\frac{d}{dt}(V_o^2) = f_1 + g_1 I_{g_{RMS}} \quad (7.26)$$

with  $g_1 \neq 0$ . The equation that relates the control input  $u = \beta$  to the inverter model is given as follows:

$$\begin{aligned} L_{ac} \frac{d}{dt}(i_g) &= v_{pwm} - v_g \\ \Leftrightarrow \frac{d}{dt}(i_g) &= f_2 + g_2 \beta \end{aligned} \quad (7.27)$$

Finally, we can construct the system's strict-feedback form, which is given by:

$$\frac{d}{dt}(V_o^2) = f_1 + g_1 I_{g_{RMS}} \quad (7.28)$$

$$\frac{d}{dt}(i_g) = f_2 + g_2 \beta \quad (7.29)$$

with  $\underline{x} = (x_1, x_2) = (V_o^2, i_g) \in \mathbb{R}^2$  and  $g_i \neq 0 \forall i \in \{1, 2\}$ .

The process starts by defining the tracking error coordinates:

$$z_1 = \epsilon_{V_o^2} = V_o^2 - V_{o_{REF}}^2 = V_o^2 - y_r^2 \quad (7.30)$$

$$z_2 = \epsilon_{i_g} = i_g - i_{g_{REF}} = i_g - \sqrt{2}\alpha_1 \sin(\omega t + \theta_v) \quad (7.31)$$

With the change of coordinates (7.30) and (7.31) it is now possible to build positive quadratic control Lyapunov Functions of  $\epsilon_{V_o^2}$  and  $\epsilon_{i_g}$  as:

$$V_1 = \frac{1}{2} z_1^2 = \frac{1}{2} (\epsilon_{V_o^2})^2 \quad (7.32)$$

$$V_2 = \frac{1}{2} z_2^2 = \frac{1}{2} (\epsilon_{i_g})^2 \quad (7.33)$$

Note that (7.33) does not contain  $V_{i-1}$  as shown in (3.8), this can be explained by the fact of the tracking error  $\epsilon_{i_g}$  not being directly related to  $\alpha_1$ .

The time derivatives of (7.32) and (7.33) are given by:

$$\frac{d}{dt} V_1 = z_1 \dot{z}_1 = \epsilon_{V_o^2} \frac{d \epsilon_{V_o^2}}{dt} \quad (7.34)$$

$$\frac{d}{dt} V_2 = z_2 \dot{z}_2 = \epsilon_{i_g} \frac{d \epsilon_{i_g}}{dt} \quad (7.35)$$

where the dynamics of the error coordinate are:

$$\begin{aligned} \dot{z}_1 &= \dot{x}_1 - \dot{y}_r \\ \Leftrightarrow \frac{d\epsilon_{V_o^2}}{dt} &= f_1 + g_1 I_{g_{RMS}} - \frac{d}{dt} V_{o_{REF}}^2 \end{aligned} \quad (7.36)$$

and:

$$\begin{aligned} \dot{z}_2 &= \dot{x}_2 - \dot{i}_{g_{REF}} \\ \Leftrightarrow \frac{d\epsilon_{i_g}}{dt} &= f_2 + g_2 \beta - \sqrt{2} \left[ \omega \cos(\omega t + \theta_v) \alpha_1 + \sin(\omega t + \theta_v) \frac{d}{dt} (\alpha_1) \right] \end{aligned} \quad (7.37)$$

substituting (7.36) in (7.34), (7.37) in (7.35) and by the application of LaSalle-Yoshizawa Theorem (3.4) it is obtained:

$$\frac{dV_1}{dt} = \epsilon_{V_o^2} \left[ f_1 + g_1 I_{g_{RMS}} - \frac{d}{dt} (V_{o_{REF}}^2) \right] = -c_1 (\epsilon_{V_o^2})^2 \quad (7.38)$$

$$\frac{dV_2}{dt} = \epsilon_{i_g} \left[ f_2 + g_2 \beta - \sqrt{2} \left( \omega \cos(\omega t + \theta_v) \alpha_1 + \sin(\omega t + \theta_v) \frac{d}{dt} (\alpha_1) \right) \right] = -c_2 (\epsilon_{i_g})^2 \quad (7.39)$$

After some manipulation of (7.38) and (7.39) the stabilizing virtual control  $\alpha_1$  (feedback law) and control input  $u$  are obtained:

$$\alpha_1 = I_{g_{RMS}} = \frac{1}{g_1} \left( -c_1 \epsilon_{V_o^2} - f_1 + \frac{d}{dt} V_{o_{REF}}^2 \right), \quad c_1 > 0 \quad (7.40)$$

$$u = \beta = \frac{1}{g_2} \left( -c_2 \epsilon_{i_g} - f_2 + \sqrt{2} \left( \omega \cos(\omega t + \theta_v) \alpha_1 + \sin(\omega t + \theta_v) \frac{d}{dt} (\alpha_1) \right) \right), \quad c_2 > 0 \quad (7.41)$$

where  $\alpha_1$  is part of the outer slow dynamics DC voltage loop and  $u$  the inner fast dynamics AC current loop.

### 7.2.1 Gain Selection

Lyapunov second method theoretically only requires that the design gains be  $c_i > 0$  for the system to be asymptotically stable. The positive design gains  $c_i$  strongly influence the dynamic of the closed loop and should be chosen carefully. Selecting larger values for  $c_i$  make the derivative of the Lyapunov function more negative, thus, making the system reaching its steady state faster, however this may lead to inner-loops performance being deteriorated in favour of the outer-loops.

A common practice is to guarantee that inner-loops have constants  $c_i$  which are greater than their respective outer-loops (i.e.  $c_i > c_{i-1}$ ) [37]. This rule should be used when selecting the positive design gains in order to guarantee a faster dynamic of the grid current.

## Chapter 8

# Simulation and Performance Analysis

The power converters (Chapter 5) performance will be measured based on the commonly used European Weighted Efficiency [17] given by:

$$\eta_{EU} = 0.20 \eta_{100\%} + 0.48 \eta_{50\%} + 0.10 \eta_{30\%} + 0.13 \eta_{20\%} + 0.06 \eta_{10\%} + 0.03 \eta_{5\%} \quad (8.1)$$

Inverters don't always operate at their maximum efficiency, the European Weighted Efficiency ( $\eta_{EU}$ ) is a weighted average operating efficiency, over a yearly power distribution. The value of this weighted efficiency is obtained by assigning a percentage of time the inverter is expected to reside in a given operating range (for a European climate).

In order to evaluate the performance of the control systems derived in Chapters 6 and 7, a set of simulation scenarios will be performed, including varying atmospheric conditions, unbalanced initial voltages between DC-link capacitors and grid disturbances.

As explained in the *Thesis Objectives* 1.5, two different control systems, represented in Figures A.2 and A.3, will be compared to choose the best control system for the proposed microinverter. For the presentation and discussion of results the controllers will be referred to as: **CFBS**, command filtering backstepping and **TCT**, traditional control techniques.

The different design constants of each controller and respective command filter parameters (when present) are displayed in Table 8.1. Analysing Table 8.1 it is possible to verify that the inner-loop gain  $c_2$  is greater than the outer-loop  $c_1$  (subchapter 7.2.1) and that the bandwidth of the filters obey the criteria shown in the inequality 3.15.

Table 8.1: All controller design gains and command filter parameters.

TCT MPPT			TCT DC-link		CFBS MPPT			CFBS DC/AC power control			
$K_p$	$K_i$	$K_w$	$K_{pV}$	$K_{iV}$	$\omega_n$	$\xi$	$c_1$	$c_1$	$\omega_n$	$\xi$	$c_2$
1.20	1959	48.49	0.0078	0.1531	$2\pi 50$	1	5000	159	$2\pi 50$	1	5000

## 8.1 Varying Atmospheric Conditions

The most important feature of the microinverter control is the MPPT and respective DC/AC voltage and current control. In order to evaluate the correctness of these control systems the PV module will be exposed to different levels of irradiance, more specifically an irradiance variation of  $1000 \text{ W/m}^2$  to  $100 \text{ W/m}^2$ .

For the sake of not overextending this Chapter no temperature variation tests are performed due to irradiance variations leading to the greater power changes (Fig. 4.2) which is a greater test to the control system.

*MPPT Control* (Fig. 8.1): When the PV module is exposed to different levels of irradiances it is expected to adjust its current  $I_{pv}$  and consequent voltage  $V_{pv}$  in order to achieve MPPT. Figure 8.1 proves that in both controllers the current at the PV module  $I_{pv}$  is adjusted accordingly to the level of irradiance. The TCT approach leads to a less successful MPPT, this is seen in the form of a "knee" (temporary non-maximum point).

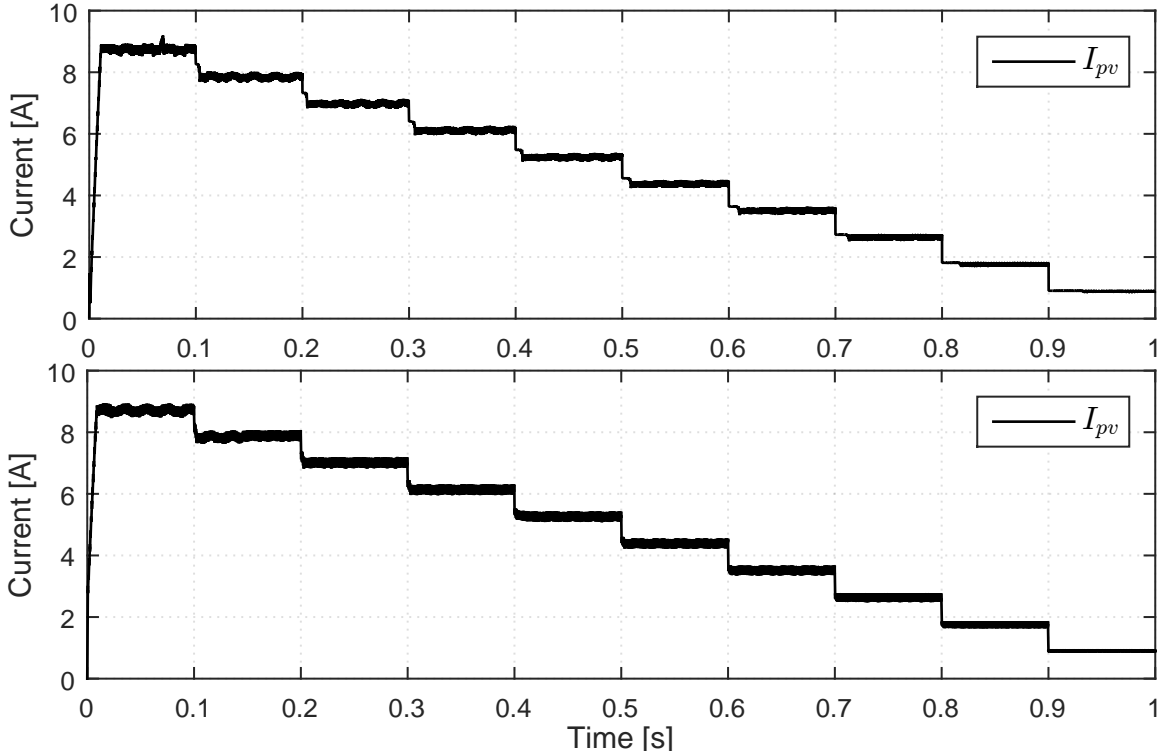


Figure 8.1: MPPT current control. Top Fig.) **TCT** approach. Bottom Fig.) **CFBS** approach.

*DC-AC Voltage Control* (Fig. 8.2): As explained in Chapter 7 the voltage at each capacitor  $C_{o_i}$  should be maintained at a higher voltage than the maximum expected grid voltage  $V_{g_{MAX}} = 358 \text{ V}$  independently of the power produced by the PV module. The objective to maintain the voltage at the DC-link above the maximum expected maximum grid value, is achieved by both controllers, although the CFBS obtains a better performance since the overshoot and undershoot when in transient regime is minimum.

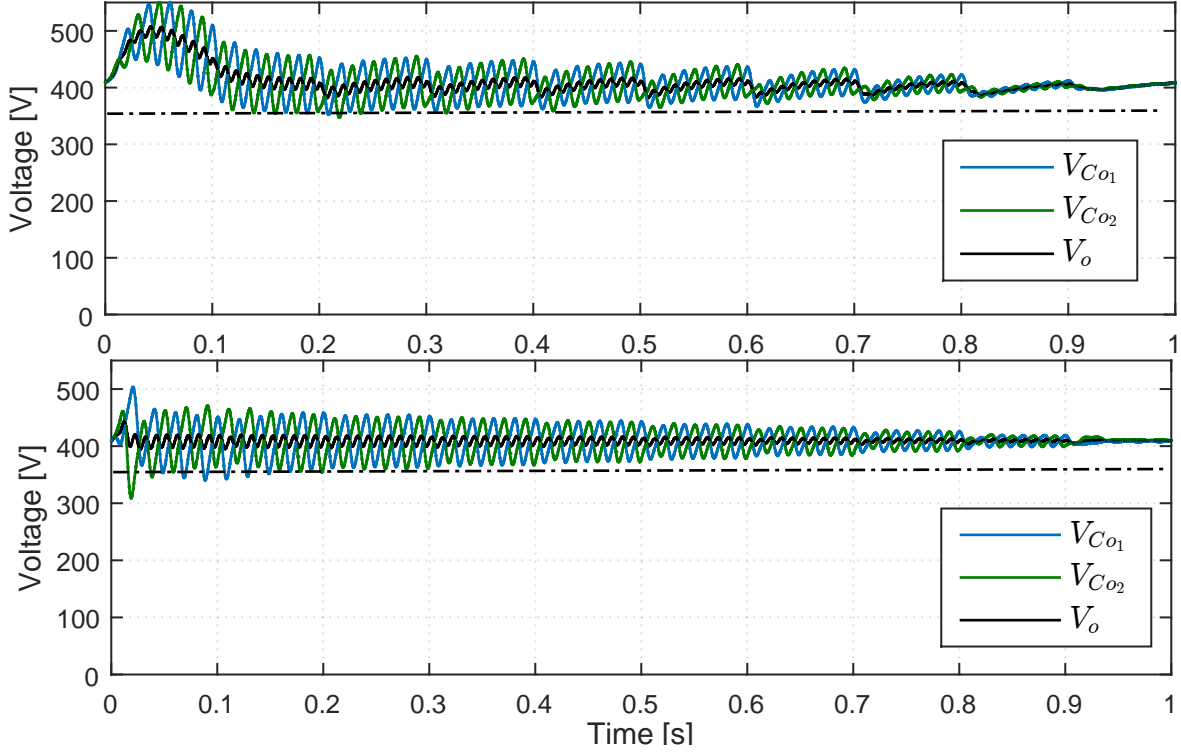


Figure 8.2: DC-AC Voltage Control. Top Fig.) **TCT** approach. Bottom Fig.) **CFBS** approach.

*DC-AC Injected Current Control* (Fig. 8.3): This control system is responsible for injecting the power produced by the PV module into the grid by imposing a sinusoidal current  $i_g$  with a nearly unity power factor. In this simulation, it is possible to verify that both control systems do in fact inject a sinusoidal current  $i_g$  into the grid for a wide range of irradiance level while the amplitude of the current  $i_{gREF}$  is provided by the DC/AC voltage control and is used as part of the reference current.  $L_{ac}$  was computed for the current (5.34), so performance loss is expected for low  $i_g$  levels.

- To evaluate the quality of the injected current a common parameter used is the *current total harmonic distortion (THD)*. As shown in Figure 8.4 both control systems exhibit low THD ( $< 10\%$ ) for a wide range of power levels, this proves that the DC-AC injected current control is in fact injecting a near sinusoidal current as supposed. Another conclusion that can be made by analysing Figure 8.4 is that the CFBS control has a lower THD for low levels of current which indicates that it has a better performance than the TCT control.
- A successful power injection should exhibit a *near unity power factor ( $f_p$ )*, since this means that the power converter is injecting mostly active power. As shown in Figure 8.5, once again, both control systems achieve this objective, since they both display  $f_p > 0.99$  for a wide range of PV module output power levels.
- The *total energy* produced  $E_{pv}$  and injected  $E_g$  can be computed based on the power curves displayed in Figure 8.6. By applying a trapezoidal numerical integration to each power curve the following produced/injected energies ( $[W s]$ ) are obtained: TCT):  $E_{pv} = 139.3$  and  $E_g = 130.0$ ; CFBS):  $E_{pv} = 146.1$  and  $E_g = 136.4$ . Which represents a 4.7% increase in  $E_{pv}$  and a 4.4% increase in  $E_g$  by the CFBS control approach.

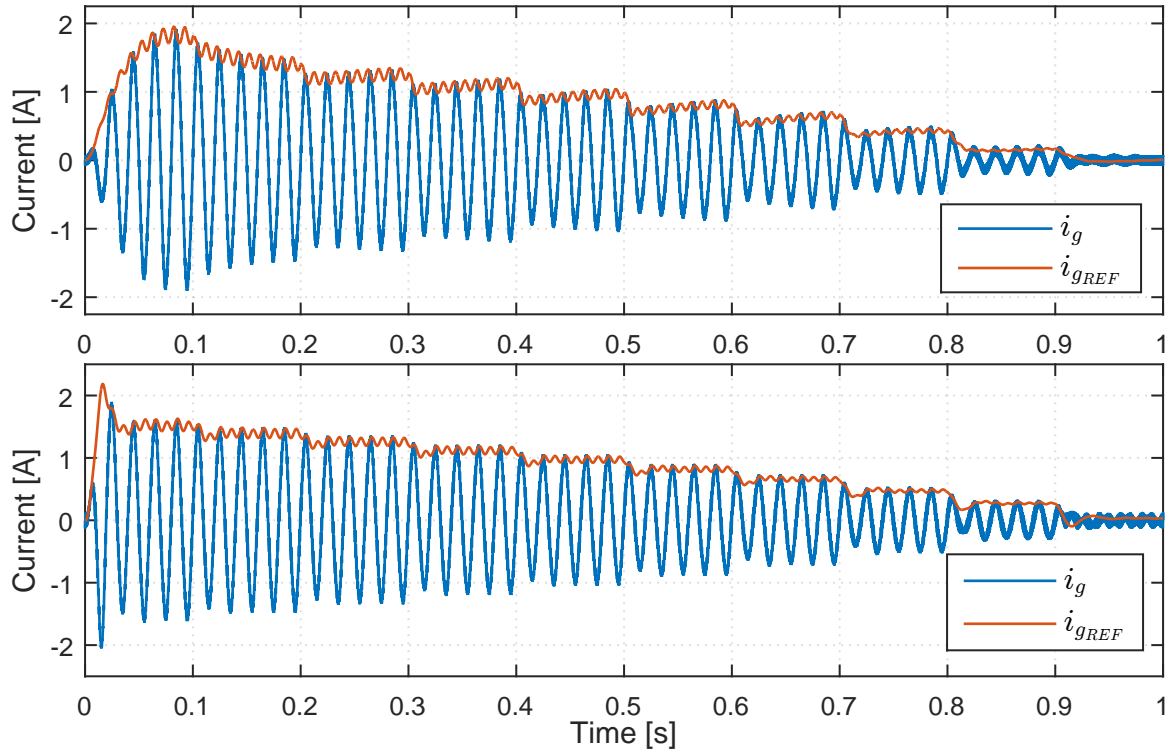


Figure 8.3: DC-AC Current Control. Top Fig.) **TCT** approach. Bottom Fig.) **CFBS** approach.

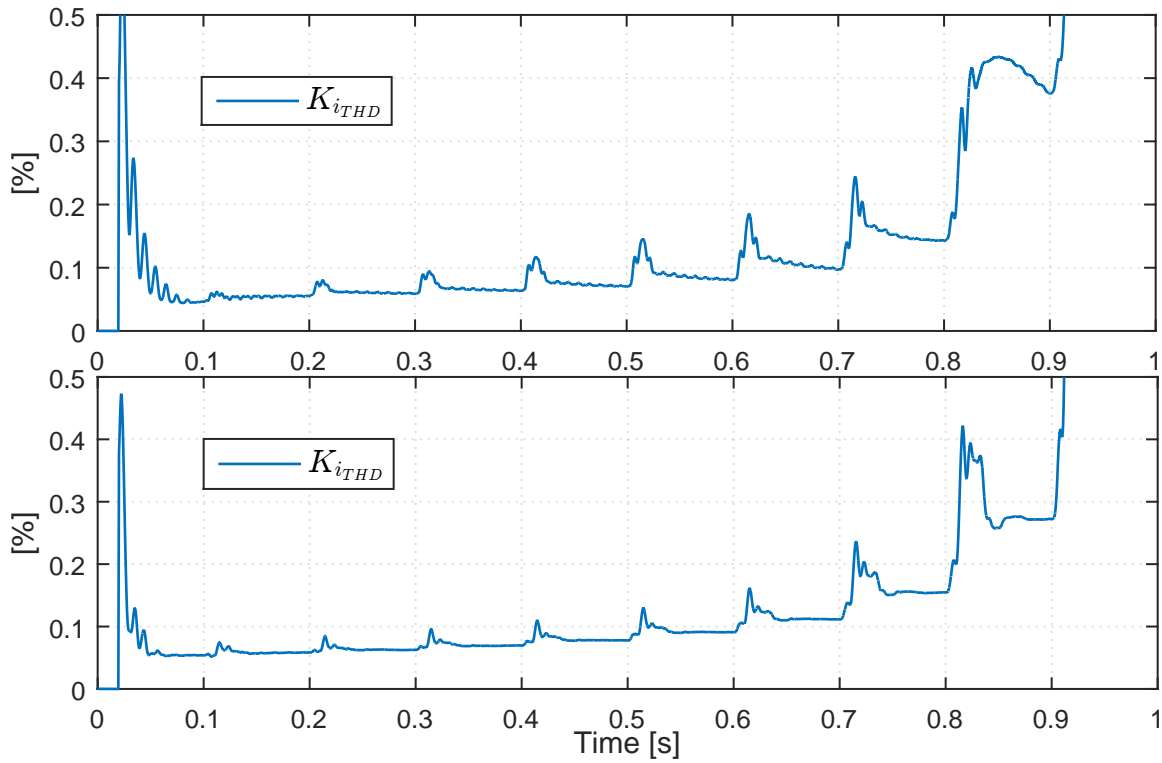


Figure 8.4: Injected current *THD*. Top Fig.) **TCT** approach. Bottom Fig.) **CFBS** approach.

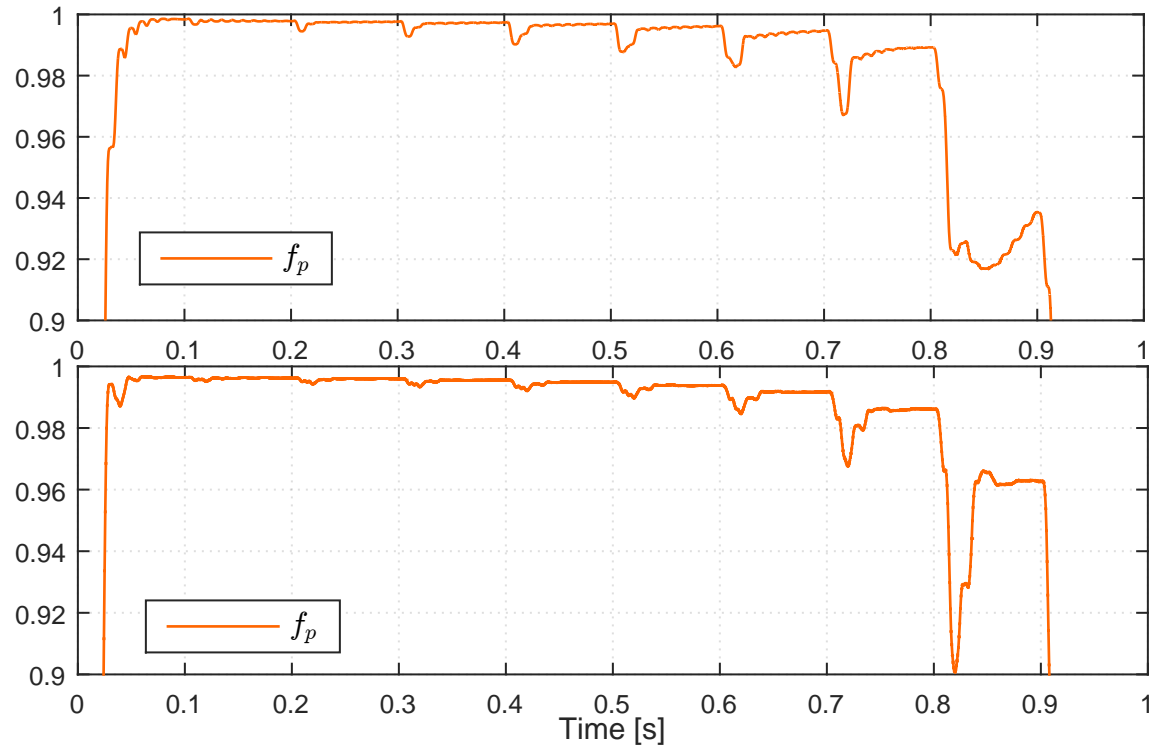


Figure 8.5: Power factor  $f.p.$ . Top Fig.) **TCT** approach. Bottom Fig.) **CFBS** approach.

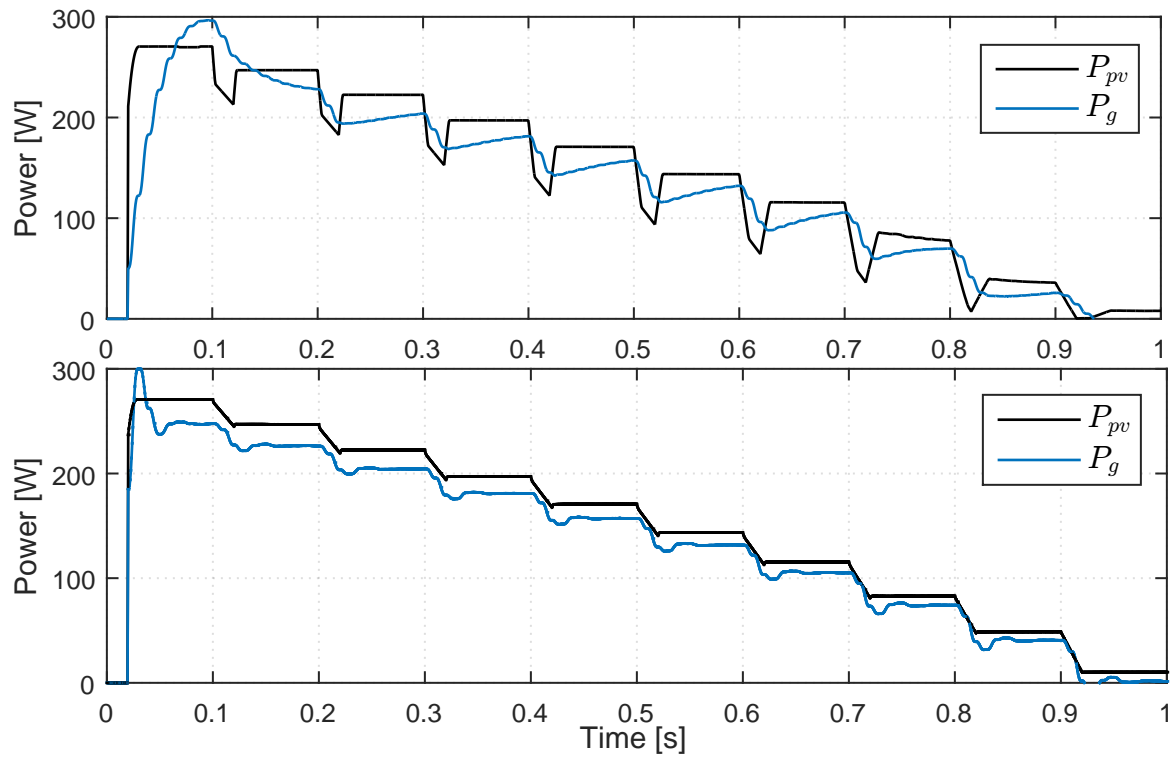


Figure 8.6: Input and Output Power Curves. Top Fig.) **TCT**. Bottom Fig.) **CFBS**.

In order for the converter to be a viable candidate for an AC module it is necessary to exhibit a high *Efficiency* for a wide range of power levels. Analysing Figure 8.7 it can be shown that the converter has a maximum steady-state efficiency of  $\eta_{Total} = 94.6\%$  and manages to maintain efficiencies  $\eta_{Total} \geq 93.1\% \forall P_{pv} \geq 30\%P_{mp}^r$  using both control approaches.

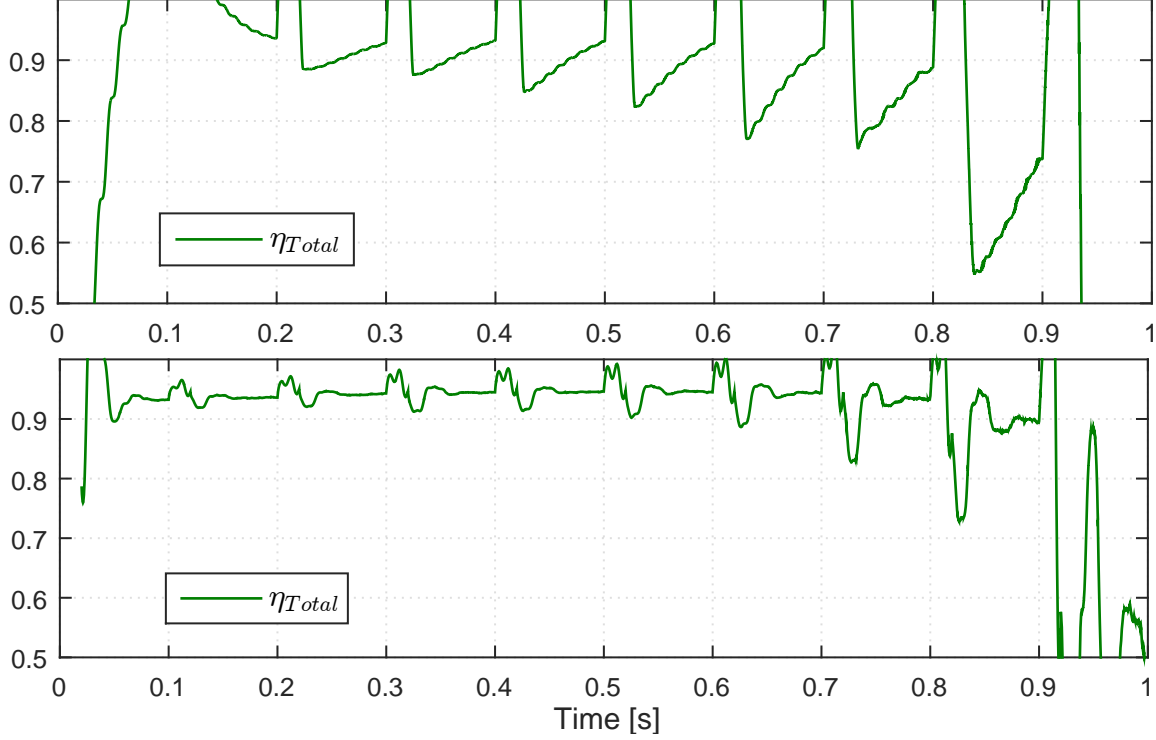


Figure 8.7: Microinverter Efficiency. Top Fig.) **TCT** approach. Bottom Fig.) **CFBS** approach.

## 8.2 European Weighted Efficiency

As explained before the  $\eta_{EU}$  is commonly used to compute the weighted average operating efficiency over a yearly power distribution, below we can find the  $\eta_{EU}$  of the CFBS approach since it has a better MPPT performance at low irradiance levels.

$$\begin{aligned}
 \eta_{EU} &= 0.20 \times \eta_{100\%} + 0.48 \times \eta_{50\%} + 0.10 \eta_{30\%} + 0.13 \eta_{20\%} + 0.06 \eta_{10\%} + 0.03 \eta_{5\%} \\
 &= 0.20 \times 93.2 + 0.48 \times 94.6 + 0.10 \times 94.0 + 0.13 \times 93.5 + 0.06 \times 89.0 + 0.03 \times 0.55 \quad (8.2) \\
 &= 91.0\%
 \end{aligned}$$

## 8.3 Unbalanced Initial Voltages

A robust control system should be able to start-up the converter even if its capacitors are initially discharged, this feature is guaranteed as shown in Figure 8.8. Another scenario that may occur is the existence of a much higher voltage in one of the capacitors when the converter is turned on (due to less parasitic losses). The controller should be capable of steering the voltages (stabilize) in case of extreme unbalanced voltages as shown in Figure 8.9 to be considered robust.

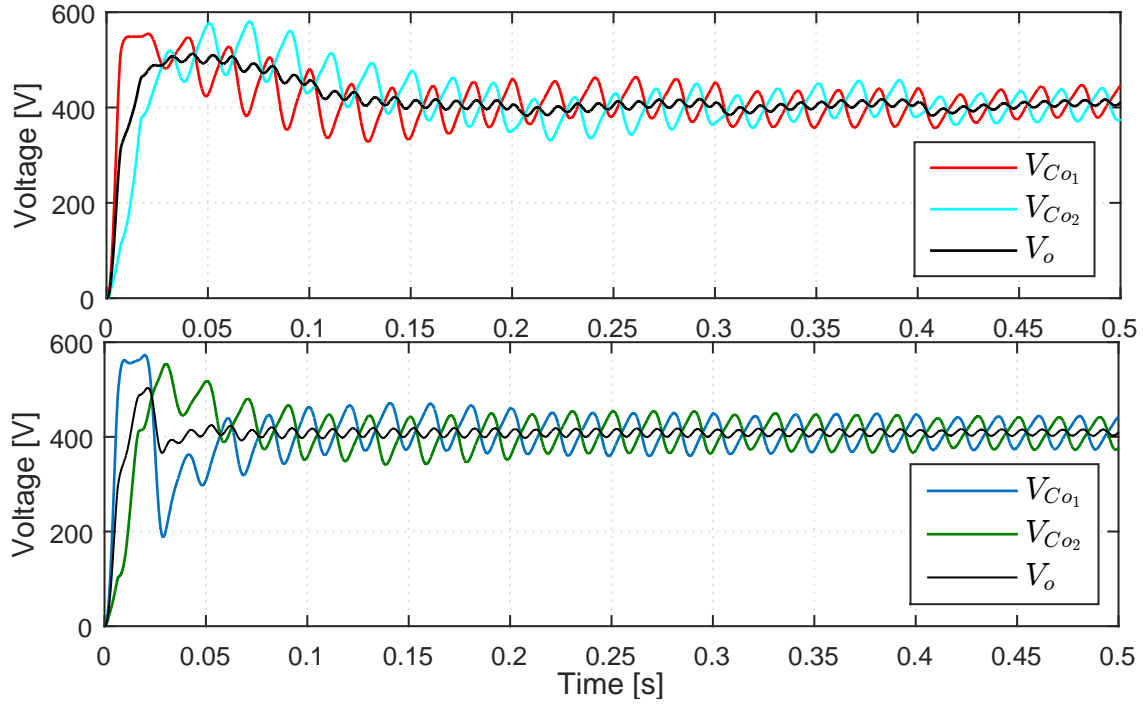


Figure 8.8: DC/AC voltage control when both capacitors are initially discharged. Top Fig.) **TCT** approach. Bottom Fig.) **CFBS** approach.

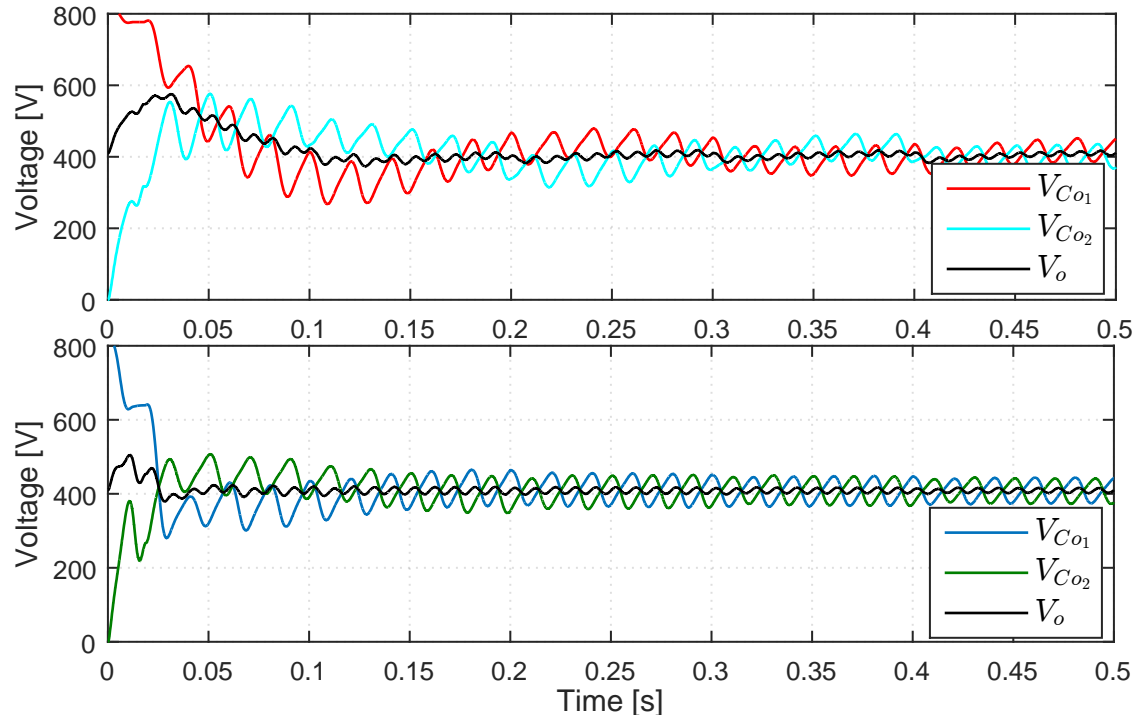


Figure 8.9: DC/AC voltage control when capacitors have different initial voltages. Top Fig.) **TCT** approach. Bottom Fig.) **CFBS** approach.

## 8.4 Grid Disturbances

The control system should also be capable of maintaining a stable behaviour, even in the presence of temporary grid disturbances. There are three types of grid disturbances: (i) *Frequency variations* (ii) *Voltage Sag<sup>1</sup> (or Voltage Dip)* and (iii) *Voltage Swell<sup>2</sup>*. As shown in Figures 8.10 and 8.11 in the presence of (ii) and (iii) grid disturbances both controllers are capable of maintaining a suitable behaviour. It is also possible to notice that the nonlinear controller maintains a near unity power factor for a wider range of disturbances. This occurs due to the nonlinear controller not assuming the grid RMS voltage as constant (shown Figure A.2).

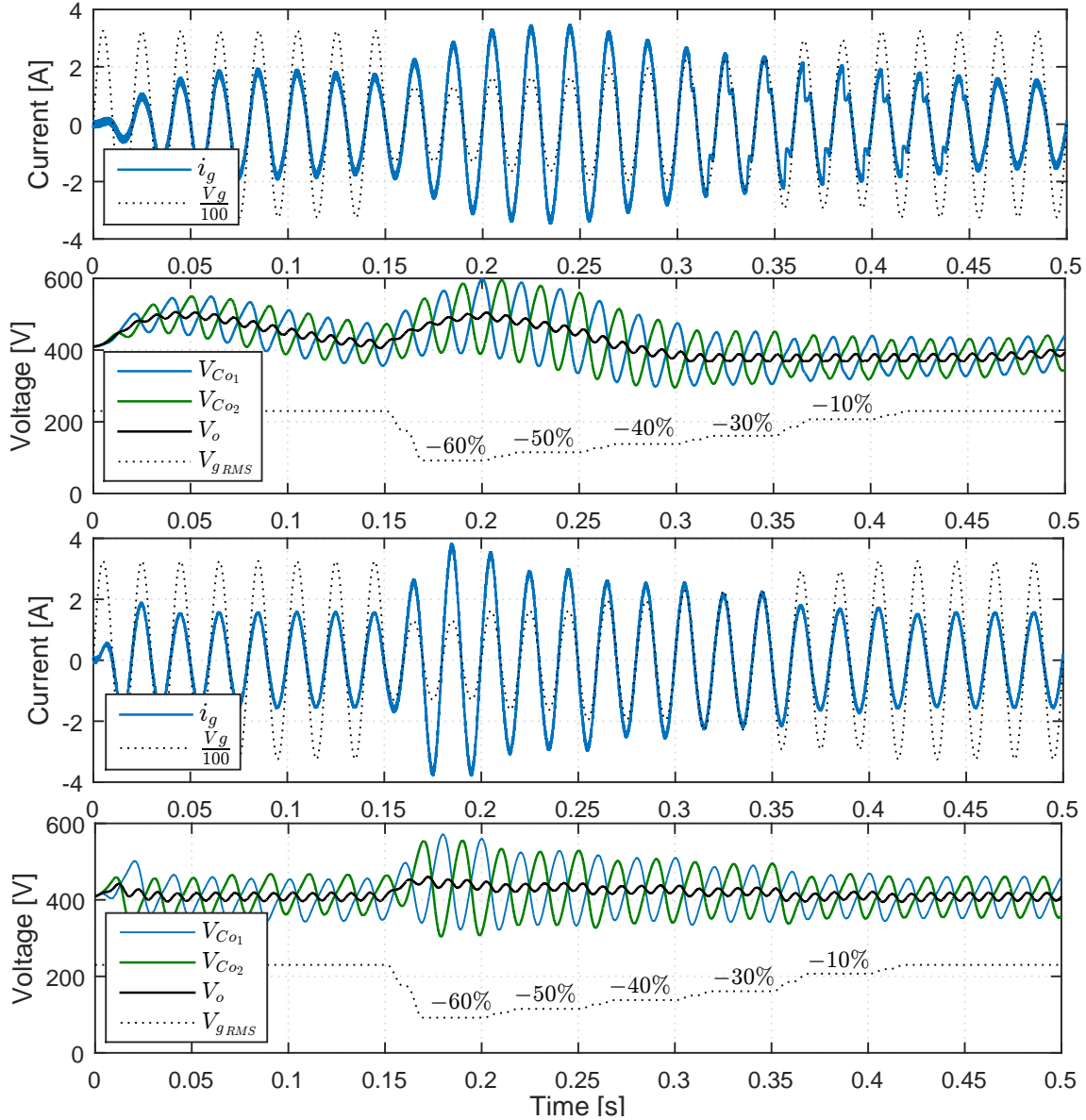


Figure 8.10: DC/AC control in presence of a grid voltage sag. Top two Fig.) **TCT** approach. Bottom two Fig.) **CFBS** approach.

<sup>1</sup>Caused by a short circuit, overload or starting of electric motors.

<sup>2</sup>Momentary increase in voltage which occurs when a heavy load disconnects from the power system.

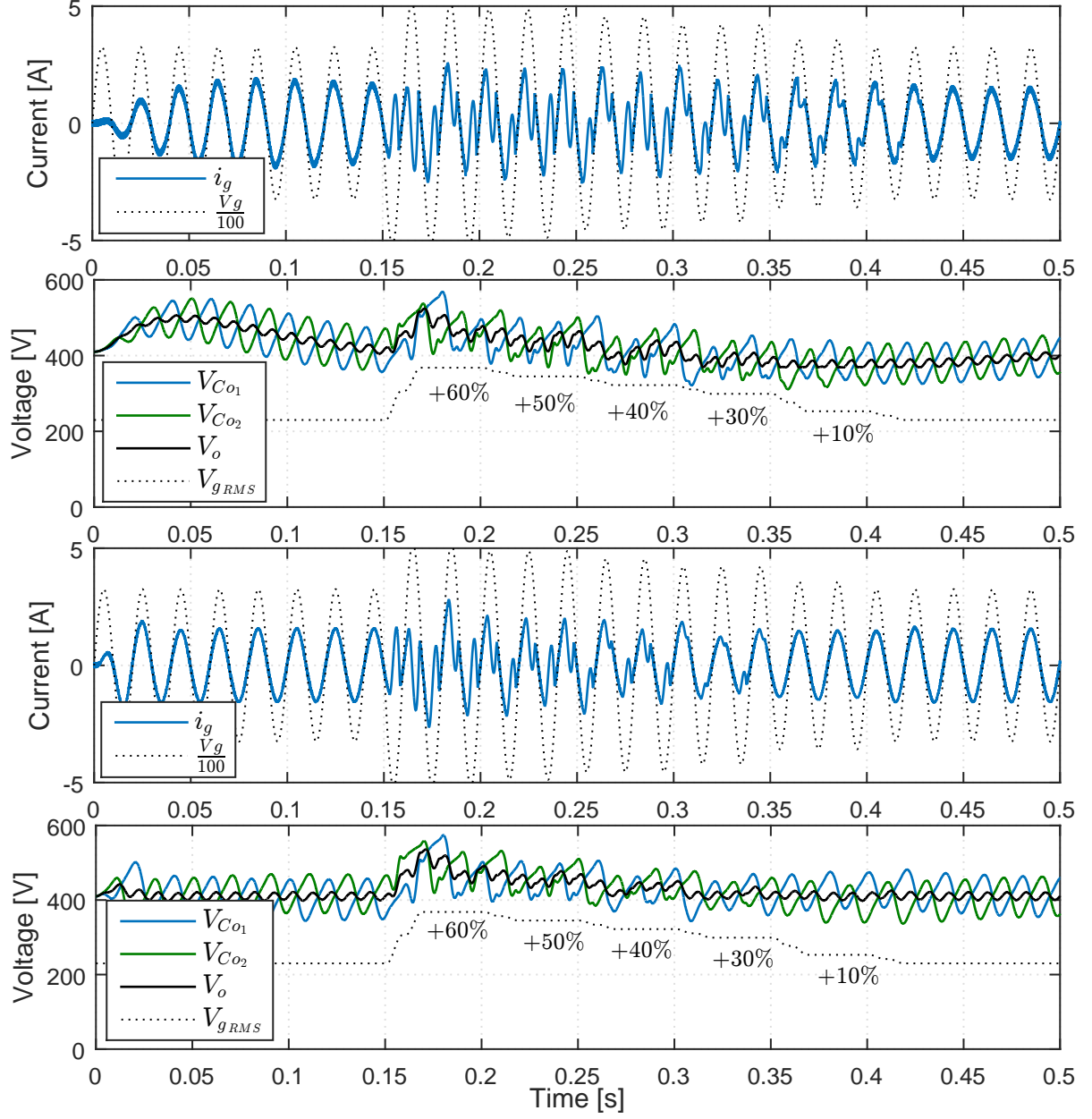


Figure 8.11: DC/AC control in the presence of a grid voltage swell. Top two Fig.) **TCT** approach. Bottom two Fig.) **CFBS** approach.

## Chapter 9

# Conclusions and Recommendations

### 9.1 Final Conclusions

The research presented in this dissertation focused on presenting a possible solution to remove the least reliable component of the microinverter, the electrolytic capacitor, but not without before explaining what causes the need for such capacitors. The solution presented was the use of a DC-DC current-fed topology converter for the MPPT control of the PV module, eliminating the need for a large capacitance across the PV module terminals. Due to the largest capacitor used in the proposed power converter being  $50\mu F$  the main objective was achieved since this value of capacitance is well within the range of a more reliable family of capacitors, the film capacitor (Fig. 2.2).

Once all the components of the proposed converter were designed, the focus was then changed to implementing two highly robust controllers both using different theoretical concepts to achieve stability.

The first controller uses the well known theory of approximating nonlinear systems by gains and delays and then using the frequency domain to obtain controllers that allow for system control, in a feedback-loop, this concept is known as linear control theory and is applicable to systems that obey the superposition principle. For each linear control system sized, frequency domain analysis was preformed in order to prove the correctness of the design, while also obtaining performance indices.

The second controller used is based on nonlinear control theory, more specifically the theory obtained by Lyapunov. One of the drawbacks related to the a nonlinear backstepping control design (concept based on Lyapunov second method) is the presence of derivatives, which, if not treated with precaution, leads the system to become unstable. To counter this problem a command filtering backstepping approach, proposed by [39] was utilized.

Once both control systems were designed and proven stable, via root-locus, step response or via Lyapunovs second method, simulations in a MATLAB/Simulink environment were made to compare which control system achieved a better performance when controlling the system composed by the PV module and a power converter.

Both control systems proved to be highly robust, however the nonlinear approach achieved better

indices of performance for every test performed without any trade-offs (i.e. overshoots or undershoots). This control approach converges to steady states much faster than the linear control without the need of high overshoot currents, which indicates that it is the better control approach, while achieving injected energy gains of 4.4%. Some trade-off's of the nonlinear control include:

- The need for more current measurements since this control does not use the superposition principle.
- Tedious gain selection, since positive design gains  $c_i$  strongly influence the dynamic of the closed loop.

In terms of the power converters performance, it has a maximum efficiency of 94.6 %, which coincided with the theoretical estimation. This efficiency value is a good value (maximum known is 96 % [10]) for a PV microinverter since, as it is well known, microinverters have the least efficient converters (due to the inclusion of the HF transformer) as displayed in Table 1.1 [10]. A European Weighted Efficiency equal to  $\eta_{EU} = 91.0\%$  was obtained.

## 9.2 Recommendations

- The high losses at the full-bridge inverter (Fig. 5.11), due to the active-clamp, indicates that maybe the ZVS-PWM full-bridge boost converter (present in Fig. 2.6) could have been a better solution to obtain a higher efficiency since its author claims efficiency improvements by at least 2% under heavy-load conditions and more than 10% under light-load conditions.
- Since the largest capacitance is located in the voltage grid inverter (bottleneck) an alternative current source grid inverter would be an interesting solution, however in this research no viable solution was found.
- In order to increase even further the controllers performance, nonlinear Adaptive Backstepping and Modular Adaptive Backstepping which include dynamic feedbacks would be the natural step forward. The adaptive feature means that the controller tunes itself for different power levels. This is achieved by the control law adjusting its gains, according to the output error of the system in order to always maintain stability and the designed performance.

# Bibliography

- [1] Fernando Silva, *"ELECTRÓNICA INDUSTRIAL Semicondutores e Conversores de Potência, 2nd Edition"*, Gulbenkian, February 2013.
- [2] Fernando Silva, *Sistemas de Alimentação Autónomas*, Notes, Instituto Superior Técnico, Universidade de Lisboa, 2015.
- [3] Fernando Silva, *Switching Power Systems*, Notes, Instituto Superior Técnico, Universidade de Lisboa, 2015.
- [4] Sónia Pinto, *Conversores Comutados para Energias Renováveis*, Notes, Instituto Superior Técnico, Universidade de Lisboa, 2014.

## **Renewable Energy Targets and Statistics:**

- [5] EU, *"<http://europa.eu/pol/ener/>"* [online] Last accessed March 2016.
- [6] ITRE, *"Decentralized Energy Systems"*, June 2010.
- [7] Eurostat, *"Key Figures on Europe"*, 2015 edition.

## **PV Systems:**

- [8] Rui Castro, *"Uma Introdução às Energias Renováveis, 2nd Edition"*, IST Press, October 2012.
- [9] Ian Woofenden, *"Photovoltaic... Cell, Module, String, Array"*, Home Power 113, June & July 2006.
- [10] Samir Kouro, Jose I. Leon, Dimitri Vinnikov & Leopoldo G. Franquelo, *"Grid-Connected Photovoltaic Systems: An Overview of Recent Research and Emerging PV Converter Technology"*, IEEE Industrial Electronics Magazine, Volume:9, Issue: 1, pp. 47-61, March 2015, DOI: 10.1109/MIE.2014.2376976.
- [11] V. Tamrakar, S. Gupta and Y. Sawle - ResearchGate Paper - Single-Diode and Two-Diode PV Cell Modelling Using Matlab For Studying Characteristics of Solar Cell Under Varying Conditions, 2015.
- [12] Hugo Martins, *"Interactive anti-islanding inverter"*, MSc Thesis, Instituto Superior Técnico, Universidade de Lisboa, October 2009.
- [13] Pedro Carlos, *"Conversor electrónico distribuído para painéis fotovoltaicos granulares"*, MSc Thesis, Instituto Superior Técnico, Universidade de Lisboa, October 2014.
- [14] Miguel Cardador, *"Seguidor de Potência Máxima para Sistema Fotovoltaico com Conversor Matricial"*, MSc Thesis, Instituto Superior Técnico, Universidade de Lisboa, June 2011.

[15] "<http://sinovoltaics.com/solar-basics/comparing-major-solar-panel-testing-conditions/>" [online], Last accessed March 2016.

[16] Abhishek Kumar Gupta & Ravi Saxena, "*Review on widely-used MPPT techniques for PV applications*", 2016 International Conference on Innovation and Challenges in Cyber Security, 3-5 Feb.2016, DOI: 10.1109/ICICCS.2016.7542321.

#### **Microinverters, Decoupling Techniques and Lifetime of Components:**

[17] S.B.Kjaer, J.K. Pedersen & F. Blaabjerg, "*A review of single-phase grid-connected inverters for photovoltaic modules*", IEEE Transactions on Industry Applications, Volume: 41, Issue: 5, pp. 1496-1504, Sept.-Oct. 2005, DOI: 10.1109/TIA.2005.853371.

[18] Cuauhtemoc Rodriguez & Gehan A. J. Amaratunga, "*Long-Lifetime Power Inverter for Photovoltaic AC Modules*", IEEE Transactions on Industrial Electronics, Volume: 55, Issue: 7, pp. 2593-2601, July 2008, DOI: 10.1109/TIE.2008.922401.

[19] S. Harb & R. S. Balog, "*Reliability of a PV-module integrated inverter (PV-MII): A usage model approach*", Photovoltaic Specialists Conference (PVSC), 38th IEEE, 3-8 June 2012, DOI: 10.1109/PVSC.2012.6317934.

[20] Fritz Schimpf & Lars Norum, "*Effective use of film capacitors in single-phase PV-inverters by active power decoupling*", IECON - 36th Annual Conference on IEEE Industrial Electronics Society, 7-10 Nov. 2010, DOI: 10.1109/IECON.2010.5675091.

[21] Quan Li & Peter Wolfs, "*A Review of the Single Phase Photovoltaic Module Integrated Converter Topologies With Three Different DC Link Configurations*", IEEE Transactions on Power Electronics, Volume: 23, Issue: 3, pp. 1320-1333, May 2008, DOI: 10.1109/TPEL.2008.920883.

[22] Haibing Hu, Souhib Harb, Nasser Kutkut, Issa Batarseh & Z. John Shen, "*A Review of Power Decoupling Techniques for Microinverters With Three Different Decoupling Capacitor Locations in PV Systems*", IEEE Transactions on Power Electronics, Volume: 28, Issue: 6, pp. 2711-2726, June 2013, DOI: 10.1109/TPEL.2012.2221482.

[23] Fumihiro Shinjo, Keiji Wada & Toshihisa Shimizu, "*A Single-Phase Grid-Connected Inverter with a Power Decoupling Function*", Power Electronics Specialists Conference - IEEE, 17-21 June 2007, DOI: 10.1109/PESC.2007.4342171.

[24] Michael Salcone & Joe Bond, "*Selecting film bus link capacitors for high performance inverter applications*", Electric Machines and Drives Conference - IEEE International, 3-6 May 2009, DOI: 10.1109/IEMDC.2009.5075431.

#### **Isolated Current-Fed DC-DC Topologies:**

[25] Mohammadjavad Baei, "*A New ZVS-PWM Full-Bridge Boost Converter*", MSc Thesis, The University of Western Ontario, March 2012.

[26] En-Sung Park, Sung Jin Choi, J.M. Lee & B.H. Cho, "*A soft-switching active-clamp scheme for isolated full-bridge boost converter*", Applied Power Electronics Conference and Exposition - APEC - Nineteenth Annual IEEE, 22-26 Feb. 2004, DOI: 10.1109/APEC.2004.1295954.

[27] Kyohei Konishi, Tomokazu Mishima & Mutsuo Nakaoka, "*A novel time-sharing current-fed ZCS high frequency inverter-applied resonant DC-DC converter for inductive power transfer*",

Applied Power Electronics Conference and Exposition (APEC) - IEEE, 20-24 March 2016, DOI: 10.1109/APEC.2016.7468109.

- [28] Young-Ho Kim, Soo-Cheol Shin, Jung-Hyo Lee, Yong-Chae Jung & Chung-Yuen Won, "*Soft-Switching Current-Fed Push-Pull Converter for 250-W AC Module Applications*", IEEE Transactions on Power Electronics, Volume: 29, Issue: 2, pp. 863-872, Feb. 2014, DOI: 10.1109/TPEL.2013.2258942.
- [29] Frédérick Bordry, "*Power converters: definitions, classification and converter topologies*", CERN Geneva Switzerland, May 2004.
- [30] Sílvia Rodrigues, *Dynamic Modeling and Control of VSC-based Multi-terminal DC Networks*, MSc Thesis, Instituto Superior Técnico, Universidade de Lisboa, December 2011.
- [31] T. Shimizu, K. Wada & N. Nakamura, "*Flyback-Type Single-Phase Utility Interactive Inverter With Power Pulsation Decoupling on the DC Input for an AC Photovoltaic Module System*", IEEE Transactions on Power Electronics, Volume: 21, Issue: 5, pp. 1264-1272, Sept. 2006, DOI: 10.1109/TPEL.2006.880247.
- [32] J.M. Carrasco, L.G. Franquelo, J.T. Bialasiewicz, E. Galvan, R.C. PortilloGuisado, M.A.M. Prats, J.I. Leon & N. Moreno-Alfonso, "*Power-Electronic Systems for the Grid Integration of Renewable Energy Sources: A Survey*", IEEE Transactions on Industrial Electronics, Volume: 53, Issue: 4, pp. 1002-1016, June 2006, DOI: 10.1109/TIE.2006.878356.

#### **Current Source Inverters:**

- [33] Carlos R. Baier, Miguel Torres, Javier A. Muñoz, Rivera A. Marco, Espinosa N. Eduardo & Pablo Acuña, "*Bidirectional power flow control of a single-phase current-source grid-tie battery energy storage system*", IEEE 24th International Symposium on Industrial Electronics (ISIE), 3-5 June 2015, DOI: 10.1109/ISIE.2015.7281673.
- [34] Yoshiya Ohnuma, Koji Orikiwa & Jun-ichi Itoh, "*A Single-Phase Current-Source PV Inverter With Power Decoupling Capability Using an Active Buffer*", IEEE Transactions on Industry Applications, Volume: 51, Issue: 1, pp. 531-538, Jan.-Feb. 2015, DOI: 10.1109/TIA.2014.2347312.

#### **Linear Control Theory:**

- [35] Christian Schmid - Website - Course on Dynamics of multidisciplinary and controlled Systems, "<http://virtual.cvut.cz/course/syscontrol/main.html>" Last accessed March 2016.
- [36] M. Ribeiro, A. Pascoal & E. Morgado, Fundamentos de Controlo, Notes, Instituto Superior Técnico, Universidade de Lisboa, 2009.

#### **Backstepping Control:**

- [37] Guilherme Trigo, "*Robust and Adaptive Nonlinear Attitude Control of a Spacecraft*", MSc Thesis, Instituto Superior Técnico, Universidade de Lisboa, October 2011.
- [38] J. Farrell, M. Polycarpou & M. Sharma, "*Adaptive backstepping with magnitude, rate, and bandwidth constraints: aircraft longitude control*", American Control Conference, 4-6 June 2003, DOI: 10.1109/ACC.2003.1240444.

- [39] Jay A. Farrell, Marios Polycarpou, Manu Sharma & Wenjie Dong, "*Command Filtered Backstepping*", IEEE Transactions on Automatic Control, Volume: 54, Issue: 6, pp. 1391-1395, June 2009, DOI: 10.1109/TAC.2009.2015562.
- [40] Jiabing Hu, Lei Shang, Yikang He & Z. Q. Zhu, "*Direct Active and Reactive Power Regulation of Grid-Connected DC/AC Converters Using Sliding Mode Control Approach*", IEEE Transactions on Power Electronics, Volume: 26, Issue: 1, pp. 210-222, Jan. 2011, DOI: 10.1109/TPEL.2010.2057518.
- [41] Aranzazu D. Martin, J. M. Cano, J. Fernando A. Silva & Jesús R. Vázquez, "*Backstepping Control of Smart Grid-Connected Distributed Photovoltaic Power Supplies for Telecom Equipment*", IEEE Transactions on Energy Conversion, Volume: 30, Issue: 4, pp. 1496-1504, Dec. 2015, DOI: 10.1109/TEC.2015.2431613.
- [42] Leonardo A. B. Tôrres, "*Teoria de Estabilidade de Lyapunov*", Notes, Abril de 2012.
- [43] Julian Cayero, Josep Cugueró & Bernardo Morcego, "*Backstepping with virtual filtered command: Application to a 2D autonomous Vehicle*", Universitat Politècnica de Catalunya, Departament d'Enginyeria de Sistemes, Automàtica i Informàtica Industrial, 2014.
- [44] He Yuebang, Pei Hailong & Zhou Hongbo, "*Command filtered backstepping-based flight control of unmanned helicopters with disturbance observers*", 34th Chinese Control Conference, 28-30 July 2015, DOI: 10.1109/ChiCC.2015.7260511.

## Appendix A

# MATLAB/Simulink Implementations

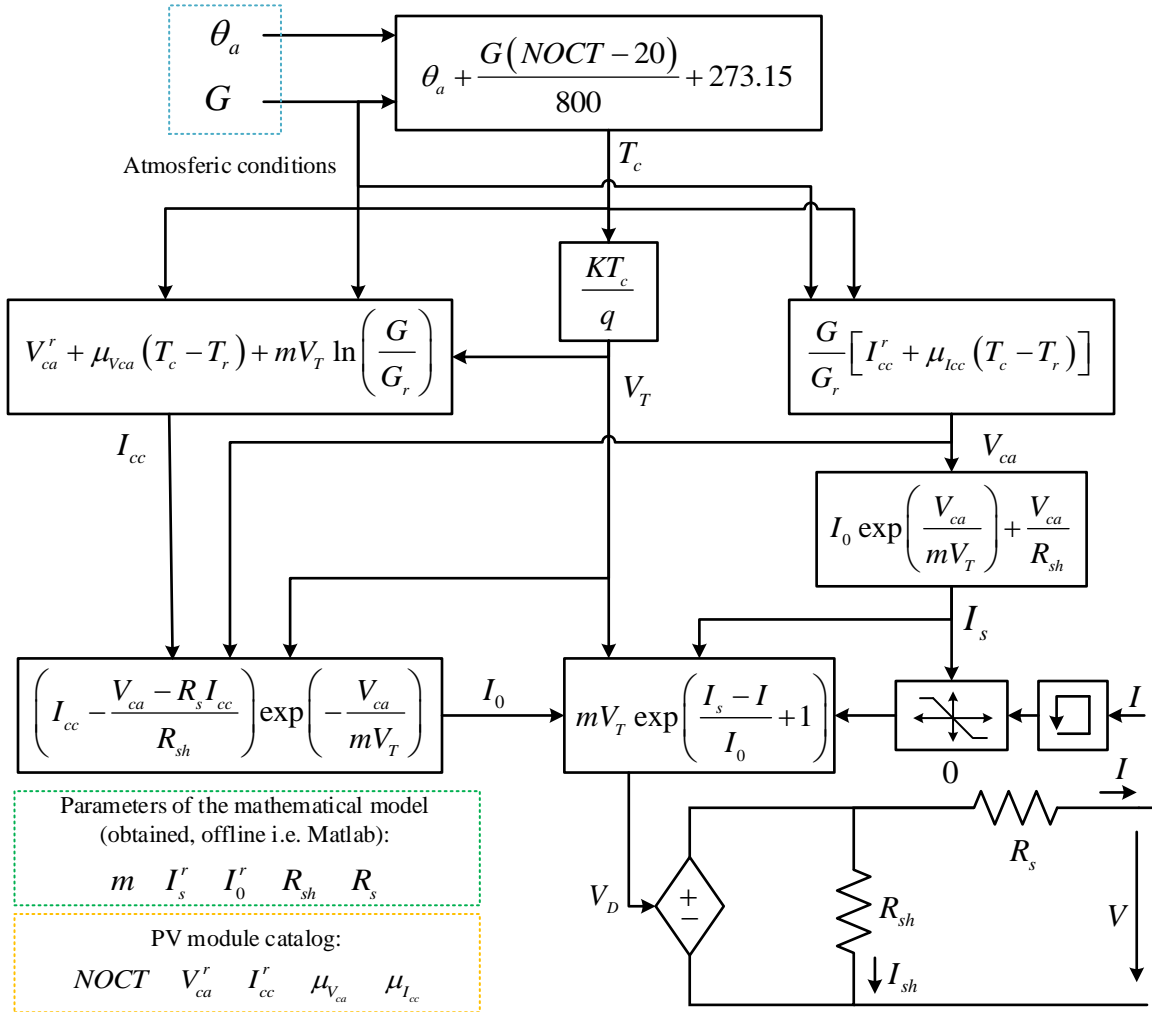
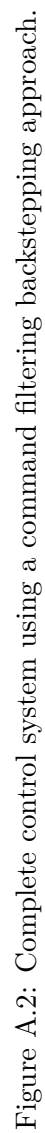


Figure A.1: Equivalent mathematical model of the PV module.



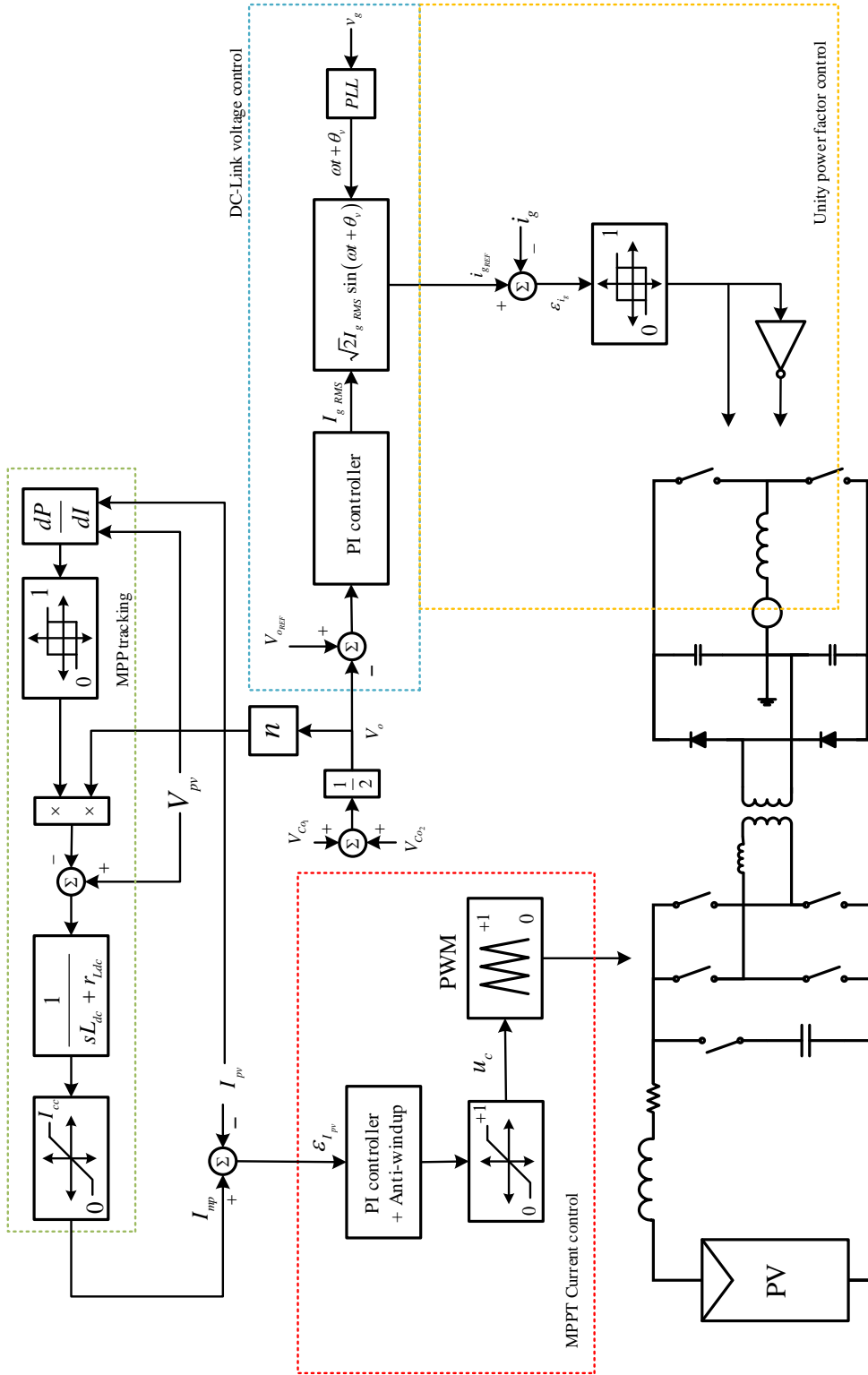
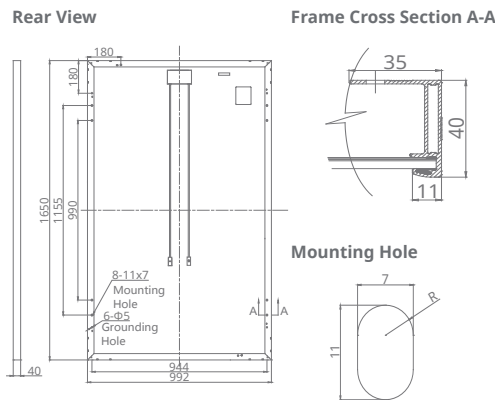


Figure A.3: Complete control system using traditional control techniques.

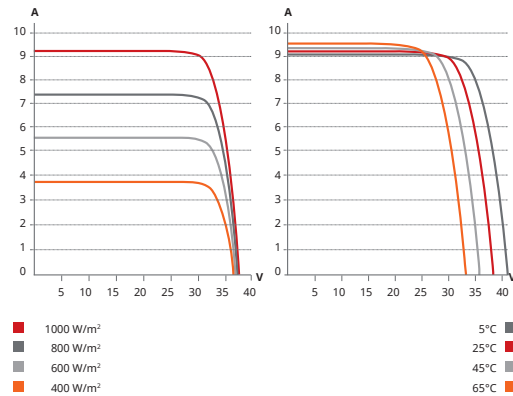
# Appendix B

## Datasheets

### ENGINEERING DRAWING (mm)



### CS6K-270M / I-V CURVES



### ELECTRICAL DATA / STC\*

CS6K	270M	275M	280M
Nominal Max. Power (Pmax)	270 W	275 W	280 W
Opt. Operating Voltage (Vmp)	31.1 V	31.3 V	31.5 V
Opt. Operating Current (Imp)	8.67 A	8.80 A	8.89 A
Open Circuit Voltage (Voc)	38.2 V	38.3 V	38.5 V
Short Circuit Current (Isc)	9.19 A	9.31 A	9.43 A
Module Efficiency	16.50 %	16.80 %	17.11 %
Operating Temperature	-40°C ~ +85°C		
Max. System Voltage	1000 V (IEC) or 1000 V (UL)		
Module Fire Performance	TYPE 1 (UL 1703) or CLASS C (IEC 61730)		
Max. Series Fuse Rating	15 A		
Application Classification	Class A		
Power Tolerance	0 ~ + 5 W		

\* Under Standard Test Conditions (STC) of irradiance of 1000 W/m², spectrum AM 1.5 and cell temperature of 25°C.

### ELECTRICAL DATA / NOCT\*

CS6K	270M	275M	280M
Nominal Max. Power (Pmax)	195 W	199 W	202 W
Opt. Operating Voltage (Vmp)	28.4 V	28.5 V	28.7 V
Opt. Operating Current (Imp)	6.87 A	6.95 A	7.04 A
Open Circuit Voltage (Voc)	35.0 V	35.1 V	35.3 V
Short Circuit Current (Isc)	7.44 A	7.54 A	7.63 A

### MECHANICAL DATA

Specification	Data
Cell Type	Mono-crystalline, 6 inch
Cell Arrangement	60 (6×10)
Dimensions	1650×992×40 mm (65.0×39.1×1.57 in)
Weight	18.2 kg (40.1 lbs)
Front Cover	3.2 mm tempered glass
Frame Material	Anodized aluminium alloy
J-Box	IP67, 3 diodes
Cable	4 mm² (IEC) or 4 mm² & 12 AWG 1000 V (UL), 1000 mm (39.4 in)
Connectors	Friends PV2a (IEC), Friends PV2b (IEC / UL)
Standard	26 pieces, 520 kg (1146.4 lbs)
Packaging	(quantity & weight per pallet)
Module Pieces per Container	728 pieces (40' HQ)

### TEMPERATURE CHARACTERISTICS

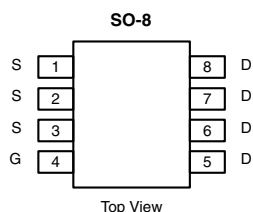
Specification	Data
Temperature Coefficient (Pmax)	-0.41 % / °C
Temperature Coefficient (Voc)	-0.31 % / °C
Temperature Coefficient (Isc)	0.053 % / °C
Nominal Operating Cell Temperature	45±2 °C

Figure B.1: Canadian Solar - CS6K - 270|275|280 PV Module main characteristics.



## N-Channel 100 V (D-S) MOSFET

PRODUCT SUMMARY			
V <sub>DS</sub> (V)	R <sub>DS(on)</sub> (Ω) Max.	I <sub>D</sub> (A) <sup>a</sup>	Q <sub>g</sub> (Typ.)
100	0.0100 at V <sub>GS</sub> = 10 V	19.7	27.9 nC
	0.0105 at V <sub>GS</sub> = 7.5 V	19.2	
	0.0120 at V <sub>GS</sub> = 6.0 V	18	



**Ordering Information:**  
Si4090DY-T1-GE3 (Lead (Pb)-free and Halogen-free)

### FEATURES

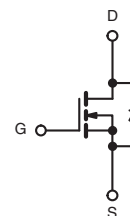
- TrenchFET® Power MOSFET
- 100 % R<sub>g</sub> and UIS Tested
- Material categorization:  
For definitions of compliance please see [www.vishay.com/doc?99912](http://www.vishay.com/doc?99912)



**RoHS**  
COMPLIANT  
HALOGEN  
**FREE**

### APPLICATIONS

- DC/DC Primary Side Switch
- Telecom/Server
- Motor Drive Control
- Synchronous Rectification



N-Channel MOSFET

ABSOLUTE MAXIMUM RATINGS (T <sub>A</sub> = 25 °C, unless otherwise noted)				
Parameter	Symbol	Limit	Unit	
Drain-Source Voltage	V <sub>DS</sub>	100	V	
Gate-Source Voltage	V <sub>GS</sub>	± 20		
Continuous Drain Current (T <sub>J</sub> = 150 °C)	I <sub>D</sub>	T <sub>C</sub> = 25 °C	19.7	A
		T <sub>C</sub> = 70 °C	15.8	
		T <sub>A</sub> = 25 °C	13.2 <sup>b, c</sup>	
		T <sub>A</sub> = 70 °C	10.4 <sup>b, c</sup>	
Pulsed Drain Current (t = 300 μs)	I <sub>DM</sub>	70		
Continuous Source-Drain Diode Current	I <sub>S</sub>	T <sub>C</sub> = 25 °C	7	
		T <sub>A</sub> = 25 °C	3.1 <sup>b, c</sup>	
Single Pulse Avalanche Current	I <sub>AS</sub>	30		
Avalanche Energy	E <sub>AS</sub>	45	mJ	
Maximum Power Dissipation	P <sub>D</sub>	T <sub>C</sub> = 25 °C	7.8	W
		T <sub>C</sub> = 70 °C	5	
		T <sub>A</sub> = 25 °C	3.5 <sup>b, c</sup>	
		T <sub>A</sub> = 70 °C	2.2 <sup>b, c</sup>	
Operating Junction and Storage Temperature Range	T <sub>J</sub> , T <sub>stg</sub>	- 55 to 150	°C	

Figure B.2: Full-Bridge Semiconductors - Part 1 - Absolute Maximum Ratings.

SPECIFICATIONS (T <sub>J</sub> = 25 °C, unless otherwise noted)																
Parameter	Symbol	Test Conditions	Min.	Typ.	Max.	Unit										
Static																
Drain-Source Breakdown Voltage	V <sub>DS</sub>	V <sub>GS</sub> = 0 V, I <sub>D</sub> = 250 μA	100			V										
V <sub>DS</sub> Temperature Coefficient	ΔV <sub>DS</sub> /T <sub>J</sub>	I <sub>D</sub> = 250 μA		67		mV/°C										
V <sub>GS(th)</sub> Temperature Coefficient	ΔV <sub>GS(th)</sub> /T <sub>J</sub>			- 6.4												
Gate-Source Threshold Voltage	V <sub>GS(th)</sub>	V <sub>DS</sub> = V <sub>GS</sub> , I <sub>D</sub> = 250 μA	2		3.3	V										
Gate-Source Leakage	I <sub>GSS</sub>	V <sub>DS</sub> = 0 V, V <sub>GS</sub> = ± 20 V			± 100	nA										
Zero Gate Voltage Drain Current	I <sub>DSS</sub>	V <sub>DS</sub> = 100 V, V <sub>GS</sub> = 0 V			1	μA										
		V <sub>DS</sub> = 100 V, V <sub>GS</sub> = 0 V, T <sub>J</sub> = 55 °C			10											
On-State Drain Current <sup>a</sup>	I <sub>D(on)</sub>	V <sub>DS</sub> ≥ 5 V, V <sub>GS</sub> = 10 V	30			A										
Drain-Source On-State Resistance <sup>a</sup>	R <sub>DS(on)</sub>	V <sub>GS</sub> = 10 V, I <sub>D</sub> = 15 A		0.0080	0.0100	Ω										
		V <sub>GS</sub> = 7.5 V, I <sub>D</sub> = 12 A		0.0085	0.0105											
		V <sub>GS</sub> = 6.0 V, I <sub>D</sub> = 10 A		0.0090	0.0120											
Forward Transconductance <sup>a</sup>	g <sub>fs</sub>	V <sub>DS</sub> = 15 V, I <sub>D</sub> = 15 A		54		S										
Dynamic <sup>b</sup>																
Input Capacitance	C <sub>iss</sub>	V <sub>DS</sub> = 50 V, V <sub>GS</sub> = 0 V, f = 1 MHz		2410		pF										
Output Capacitance	C <sub>oss</sub>			790												
Reverse Transfer Capacitance	C <sub>rss</sub>			60												
Total Gate Charge	Q <sub>g</sub>	V <sub>DS</sub> = 50 V, V <sub>GS</sub> = 10 V, I <sub>D</sub> = 10 A		45.6	69	nC										
Gate-Source Charge	Q <sub>gs</sub>	V <sub>DS</sub> = 50 V, V <sub>GS</sub> = 6 V, I <sub>D</sub> = 10 A		27.9	42											
Gate-Drain Charge	Q <sub>gd</sub>			8.5												
Output Charge	Q <sub>oss</sub>			9.2												
Gate Resistance	R <sub>g</sub>	V <sub>DS</sub> = 50 V, V <sub>GS</sub> = 0 V		63	95											
Turn-On Delay Time	t <sub>d(on)</sub>	f = 1 MHz	0.4	1.3	2.6	Ω										
Rise Time	t <sub>r</sub>						V <sub>DD</sub> = 50 V, R <sub>L</sub> = 5 Ω I <sub>D</sub> ≅ 10 A, V <sub>GEN</sub> = 7.5 V, R <sub>g</sub> = 1 Ω		16	32						
Turn-Off Delay Time	t <sub>d(off)</sub>										V <sub>DD</sub> = 50 V, R <sub>L</sub> = 5 Ω I <sub>D</sub> ≅ 10 A, V <sub>GEN</sub> = 10 V, R <sub>g</sub> = 1 Ω		11	22		
Fall Time	t <sub>f</sub>															35
Turn-On Delay Time	t <sub>d(on)</sub>		10	20												
Rise Time	t <sub>r</sub>															
Turn-Off Delay Time	t <sub>d(off)</sub>							10	20							
Fall Time	t <sub>f</sub>										36	70				
Drain-Source Body Diode Characteristics																
Continuous Source-Drain Diode Current	I <sub>S</sub>	T <sub>C</sub> = 25 °C				7							A			
Pulse Diode Forward Current <sup>a</sup>	I <sub>SM</sub>				70											
Body Diode Voltage	V <sub>SD</sub>	I <sub>S</sub> = 5 A		0.75	1.1	V										
Body Diode Reverse Recovery Time	t <sub>rr</sub>	I <sub>F</sub> = 10 A, di/dt = 100 A/μs, T <sub>J</sub> = 25 °C		49	95	ns										
Body Diode Reverse Recovery Charge	Q <sub>rr</sub>			58	115	nC										
Reverse Recovery Fall Time	t <sub>a</sub>			21		ns										
Reverse Recovery Rise Time	t <sub>b</sub>			28												

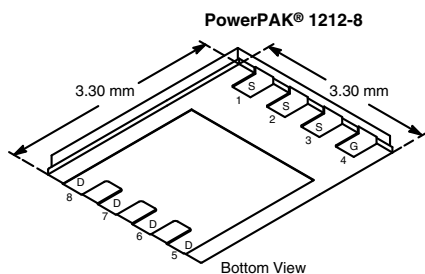
Figure B.3: Full-Bridge Semiconductors - Part 2 - Specifications MOSFET and Body Diode.



**SiS890DN**  
Vishay Siliconix

## N-Channel 100 V (D-S) MOSFET

PRODUCT SUMMARY			
V <sub>DS</sub> (V)	R <sub>DS(on)</sub> (Ω) (Max.)	I <sub>D</sub> (A) <sup>f</sup>	Q <sub>g</sub> (Typ.)
100	0.0235 at V <sub>GS</sub> = 10 V	30 <sup>g</sup>	9.5 nC
	0.0245 at V <sub>GS</sub> = 7.5 V	30 <sup>g</sup>	
	0.0315 at V <sub>GS</sub> = 4.5 V	28.5	



Ordering Information:  
SiS890DN-T1-GE3 (Lead (Pb)-free and Halogen-free)

### FEATURES

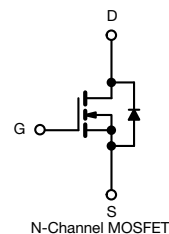
- TrenchFET® Power MOSFET
- 100 % R<sub>g</sub> and UIS Tested
- Capable of Operating with 5 V Gate Drive
- Material categorization:  
For definitions of compliance please see  
[www.vishay.com/doc?99912](http://www.vishay.com/doc?99912)



**RoHS**  
COMPLIANT  
HALOGEN  
FREE

### APPLICATIONS

- Telecom Bricks
- Primary side switch
- Synchronous Rectification
- Industrial



ABSOLUTE MAXIMUM RATINGS (T <sub>A</sub> = 25 °C, unless otherwise noted)				
Parameter	Symbol	Limit	Unit	
Drain-Source Voltage	V <sub>DS</sub>	100	V	
Gate-Source Voltage	V <sub>GS</sub>	± 20		
Continuous Drain Current (T <sub>J</sub> = 150 °C)	T <sub>C</sub> = 25 °C	30 <sup>g</sup>	A	
	T <sub>C</sub> = 70 °C	26.5		
	T <sub>A</sub> = 25 °C	8.8 <sup>a, b</sup>		
	T <sub>A</sub> = 70 °C	7.1 <sup>a, b</sup>		
Pulsed Drain Current (t = 300 μs)	I <sub>DM</sub>	60		
Continuous Source-Drain Diode Current	T <sub>C</sub> = 25 °C	30 <sup>g</sup>		
	T <sub>A</sub> = 25 °C	3.1 <sup>a, b</sup>		
Single Pulse Avalanche Current	I <sub>AS</sub>	10		
Single Pulse Avalanche Energy	E <sub>AS</sub>	5	mJ	
Maximum Power Dissipation	T <sub>C</sub> = 25 °C	52	W	
	T <sub>C</sub> = 70 °C	33		
	T <sub>A</sub> = 25 °C	3.7 <sup>a, b</sup>		
	T <sub>A</sub> = 70 °C	2.4 <sup>a, b</sup>		
Operating Junction and Storage Temperature Range	T <sub>J</sub> , T <sub>stg</sub>	- 55 to 150	°C	
Soldering Recommendations (Peak Temperature) <sup>c, d</sup>		260		

Figure B.4: Active-Clamp Semiconductor - Part 1 - Absolute Maximum Ratings.

SPECIFICATIONS (T <sub>J</sub> = 25 °C, unless otherwise noted)						
Parameter	Symbol	Test Conditions	Min.	Typ.	Max.	Unit
Static						
Drain-Source Breakdown Voltage	V <sub>DS</sub>	V <sub>GS</sub> = 0 V, I <sub>D</sub> = 250 μA	100			V
V <sub>DS</sub> Temperature Coefficient	ΔV <sub>DS</sub> /T <sub>J</sub>	I <sub>D</sub> = 250 μA		63		mV/°C
V <sub>GS(th)</sub> Temperature Coefficient	ΔV <sub>GS(th)</sub> /T <sub>J</sub>			- 5.5		
Gate-Source Threshold Voltage	V <sub>GS(th)</sub>	V <sub>DS</sub> = V <sub>GS</sub> , I <sub>D</sub> = 250 μA	1.5		3	V
Gate-Source Leakage	I <sub>GSS</sub>	V <sub>DS</sub> = 0 V, V <sub>GS</sub> = ± 20 V			± 100	nA
Zero Gate Voltage Drain Current	I <sub>DSS</sub>	V <sub>DS</sub> = 100 V, V <sub>GS</sub> = 0 V			1	μA
		V <sub>DS</sub> = 100 V, V <sub>GS</sub> = 0 V, T <sub>J</sub> = 55 °C			10	
On-State Drain Current <sup>a</sup>	I <sub>D(on)</sub>	V <sub>DS</sub> ≥ 5 V, V <sub>GS</sub> = 10 V	20			A
Drain-Source On-State Resistance <sup>a</sup>	R <sub>DS(on)</sub>	V <sub>GS</sub> = 10 V, I <sub>D</sub> = 10 A		0.0195	0.0235	Ω
		V <sub>GS</sub> = 7.5 V, I <sub>D</sub> = 7 A		0.0204	0.0245	
		V <sub>GS</sub> = 4.5 V, I <sub>D</sub> = 5 A		0.0260	0.0315	
Forward Transconductance <sup>a</sup>	g <sub>fs</sub>	V <sub>DS</sub> = 15 V, I <sub>D</sub> = 10 A		25		S
Dynamic <sup>b</sup>						
Input Capacitance	C <sub>iss</sub>	V <sub>DS</sub> = 50 V, V <sub>GS</sub> = 0 V, f = 1 MHz		802		pF
Output Capacitance	C <sub>oss</sub>			291		
Reverse Transfer Capacitance	C <sub>rss</sub>			39		
Total Gate Charge	Q <sub>g</sub>	V <sub>DS</sub> = 50 V, V <sub>GS</sub> = 10 V, I <sub>D</sub> = 10 A		19.1	29	nC
		V <sub>DS</sub> = 50 V, V <sub>GS</sub> = 7.5 V, I <sub>D</sub> = 10 A		14.7	22	
Gate-Source Charge	Q <sub>gs</sub>	V <sub>DS</sub> = 50 V, V <sub>GS</sub> = 4.5 V, I <sub>D</sub> = 10 A		9.5	14.5	
Gate-Drain Charge	Q <sub>gd</sub>			2.8		
Output Charge	Q <sub>oss</sub>			4.9		
Output Charge	Q <sub>oss</sub>	V <sub>DS</sub> = 50 V, V <sub>GS</sub> = 0 V		23	35	
Gate Resistance	R <sub>g</sub>	f = 1 MHz	0.2	0.9	1.8	Ω
Turn-On Delay Time	t <sub>d(on)</sub>	V <sub>DD</sub> = 50 V, R <sub>L</sub> = 5 Ω I <sub>D</sub> ≅ 10 A, V <sub>GEN</sub> = 7.5 V, R <sub>g</sub> = 1 Ω		10	20	ns
Rise Time	t <sub>r</sub>			12	24	
Turn-Off Delay Time	t <sub>d(off)</sub>			16	32	
Fall Time	t <sub>f</sub>			9	18	
Turn-On Delay Time	t <sub>d(on)</sub>	V <sub>DD</sub> = 50 V, R <sub>L</sub> = 5 Ω I <sub>D</sub> ≅ 10 A, V <sub>GEN</sub> = 10 V, R <sub>g</sub> = 1 Ω		9	18	
Rise Time	t <sub>r</sub>			10	20	
Turn-Off Delay Time	t <sub>d(off)</sub>			16	32	
Fall Time	t <sub>f</sub>			8	16	
Drain-Source Body Diode Characteristics						
Continuous Source-Drain Diode Current	I <sub>S</sub>	T <sub>C</sub> = 25 °C			30	A
Pulse Diode Forward Current	I <sub>SM</sub>				60	
Body Diode Voltage	V <sub>SD</sub>	I <sub>S</sub> = 4 A, V <sub>GS</sub> = 0 V		0.78	1.2	V
Body Diode Reverse Recovery Time	t <sub>rr</sub>	I <sub>F</sub> = 10 A, dI/dt = 100 A/μs, T <sub>J</sub> = 25 °C		34	68	ns
Body Diode Reverse Recovery Charge	Q <sub>rr</sub>			34	68	nC
Reverse Recovery Fall Time	t <sub>a</sub>			19.5		ns
Reverse Recovery Rise Time	t <sub>b</sub>			14.5		

Figure B.5: Active-Clamp Semiconductor - Part 2 - Specifications MOSFET and Body Diode.

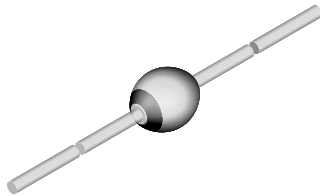


www.vishay.com

SF1200, SF1600

Vishay Semiconductors

## Ultrafast Avalanche Sinterglass Diode



949539

### FEATURES

- Very low switching losses
- Glass passivated
- High reverse voltage
- Hermetically sealed axial-leaded glass envelope
- Material categorization:  
For definitions of compliance please see [www.vishay.com/doc?99912](http://www.vishay.com/doc?99912)



### APPLICATIONS

- Switched mode power supplies
- High-frequency inverter circuits

### MECHANICAL DATA

**Case:** SOD-57

**Terminals:** plated axial leads, solderable per MIL-STD-750, method 2026

**Polarity:** color band denotes cathode end

**Mounting position:** any

**Weight:** approx. 369 mg

### ORDERING INFORMATION (Example)

DEVICE NAME	ORDERING CODE	TAPED UNITS	MINIMUM ORDER QUANTITY
SF1600	SF1600-TR	5000 per 10" tape and reel	25 000
SF1600	SF1600-TAP	5000 per ammpack	25 000

### PARTS TABLE

PART	TYPE DIFFERENTIATION	PACKAGE
SF1200	$V_R = 1200\text{ V}$ ; $I_{F(AV)} = 1\text{ A}$	SOD-57
SF1600	$V_R = 1600\text{ V}$ ; $I_{F(AV)} = 1\text{ A}$	SOD-57

### ABSOLUTE MAXIMUM RATINGS ( $T_{amb} = 25\text{ }^{\circ}\text{C}$ , unless otherwise specified)

PARAMETER	TEST CONDITION	PART	SYMBOL	VALUE	UNIT
Reverse voltage = repetitive peak reverse voltage	See electrical characteristics	SF1200	$V_R = V_{RRM}$	1200	V
		SF1600	$V_R = V_{RRM}$	1600	V
Peak forward surge current	$t_p = 10\text{ ms}$ , half sine wave		$I_{FSM}$	30	A
Average forward current	Half sine wave, $V_R = V_{RRM}$ , $R_{thJA} = 45\text{ K/W}$		$I_{F(AV)}$	1	A
Max. pulse energy in avalanche mode, non repetitive (inductive load switch off)	$I_{(BR)R} = 400\text{ mA}$ , inductive load		$E_R$	10	mJ
Junction and storage temperature					

Figure B.6: Half-bridge Rectifier Semiconductor - Part 1 - Absolute Maximum Ratings.

<b>ELECTRICAL CHARACTERISTICS</b> ( $T_{amb} = 25\text{ }^{\circ}\text{C}$ , unless otherwise specified)							
PARAMETER	TEST CONDITION	PART	SYMBOL	MIN.	TYP.	MAX.	UNIT
Forward voltage	$I_F = 1\text{ A}$		$V_F$	-	-	3.4	V
Reverse current	$V_R = V_{RRM}$		$I_R$	-	-	5	$\mu\text{A}$
	$V_R = V_{RRM}, T_j = 125\text{ }^{\circ}\text{C}$		$I_R$	-	-	50	$\mu\text{A}$
Reverse breakdown voltage	$I_R = 100\text{ }\mu\text{A}$	SF1200	$V_{(BR)R}$	1250	-	-	V
		SF1600	$V_{(BR)R}$	1650	-	-	V
Reverse recovery time	$I_F = 0.5\text{ A}, I_R = 1\text{ A}, i_R = 0.25\text{ A}$		$t_{rr}$	-	-	75	ns

**TYPICAL CHARACTERISTICS** ( $T_{amb} = 25\text{ }^{\circ}\text{C}$ , unless otherwise specified)

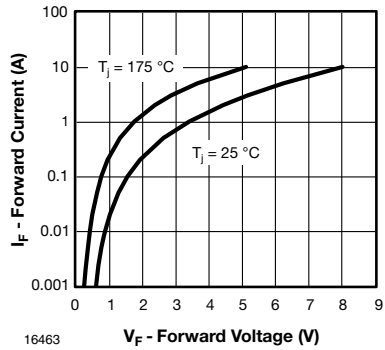


Fig. 1 - Forward Current vs. Forward Voltage

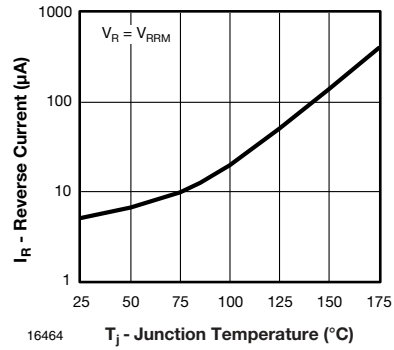


Fig. 3 - Reverse Current vs. Junction Temperature

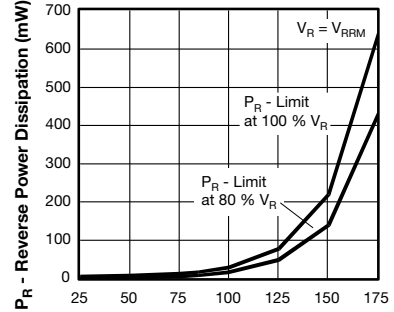
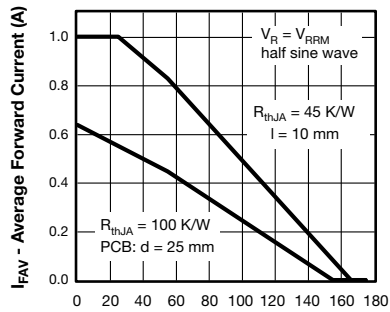


Figure B.7: Half-bridge Rectifier Semiconductor - Part 2 - Characteristic curves.



## C2M1000170J

**Silicon Carbide Power MOSFET**  
**C2M™ MOSFET Technology**  
N-Channel Enhancement Mode

$V_{DS}$	1700 V
$I_D$ @ 25°C	5.3 A
$R_{DS(on)}$	1.0 $\Omega$

### Features

- High blocking voltage with low  $R_{DS(on)}$
- Easy to parallel and simple to drive
- Low parasitic inductance
- Separate driver source pin
- Ultra-low drain-gate capacitance
- Halogen Free, RoHS compliant

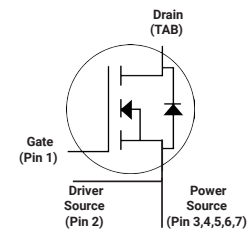
### Benefits

- Higher system efficiency
- Smooth switching waveforms
- Reduced cooling requirements
- Increased system reliability

### Applications

- Auxiliary power supplies
- Switch Mode Power Supplies
- High-voltage capacitive loads

### Package



Part Number	Package
C2M1000170J	7L D2PAK

### Maximum Ratings ( $T_C = 25^\circ\text{C}$ unless otherwise specified)

Symbol	Parameter	Value	Unit	Test Conditions	Note
$V_{DSmax}$	Drain - Source Voltage	1700	V	$V_{GS} = 0\text{ V}$ , $I_D = 100\text{ }\mu\text{A}$	
$V_{GSmax}$	Gate - Source Voltage	-10/+25	V	Absolute maximum values	
$V_{GSop}$	Gate - Source Voltage	-5/+20	V	Recommended operational values	
$I_D$	Continuous Drain Current	5.3	A	$V_{GS} = 20\text{ V}$ , $T_C = 25^\circ\text{C}$	Fig. 19
		3.6		$V_{GS} = 20\text{ V}$ , $T_C = 100^\circ\text{C}$	
$I_{D(pulse)}$	Pulsed Drain Current	6.0	A	Pulse width $t_p$ limited by $T_{jmax}$	Fig. 22
$P_D$	Power Dissipation	78	W	$T_C = 25^\circ\text{C}$ , $T_J = 150^\circ\text{C}$	Fig. 20
$T_J, T_{stg}$	Operating Junction and Storage Temperature	-55 to +150	$^\circ\text{C}$		
$T_L$	Solder Temperature	260	$^\circ\text{C}$	1.6mm (0.063") from case for 10s	

Figure B.8: Half-bridge Inverter Semiconductor - Part 1 - Absolute Maximum Ratings.

### Electrical Characteristics (T<sub>c</sub> = 25 °C unless otherwise specified)

Symbol	Parameter	Min.	Typ.	Max.	Unit	Test Conditions	Note
V <sub>(BR)DSS</sub>	Drain-Source Breakdown Voltage	1700			V	V <sub>GS</sub> = 0 V, I <sub>D</sub> = 100 µA	
V <sub>GS(th)</sub>	Gate Threshold Voltage	2.0	2.6	4	V	V <sub>DS</sub> = V <sub>GS</sub> , I <sub>D</sub> = 0.5 mA	Fig. 11
			2.1		V	V <sub>DS</sub> = V <sub>GS</sub> , I <sub>D</sub> = 0.5 mA, T <sub>J</sub> = 150 °C	
I <sub>DSS</sub>	Zero Gate Voltage Drain Current		1	100	µA	V <sub>DS</sub> = 1.7 kV, V <sub>GS</sub> = 0 V	
I <sub>GSS</sub>	Gate-Source Leakage Current			250	nA	V <sub>GS</sub> = 20 V, V <sub>DS</sub> = 0 V	
R <sub>DS(on)</sub>	Drain-Source On-State Resistance		1.0	1.4	Ω	V <sub>GS</sub> = 20 V, I <sub>D</sub> = 2 A	Fig. 4,5,6
			2.0			V <sub>GS</sub> = 20 V, I <sub>D</sub> = 2 A, T <sub>J</sub> = 150 °C	
g <sub>fs</sub>	Transconductance		0.82		S	V <sub>DS</sub> = 20 V, I <sub>DS</sub> = 2 A	Fig. 7
			0.81			V <sub>DS</sub> = 20 V, I <sub>DS</sub> = 2 A, T <sub>J</sub> = 150 °C	
C <sub>iss</sub>	Input Capacitance		200		pF	V <sub>GS</sub> = 0 V	Fig. 17,18
C <sub>oss</sub>	Output Capacitance		12			V <sub>DS</sub> = 1000 V	
C <sub>rss</sub>	Reverse Transfer Capacitance		1.3			f = 1 MHz	
E <sub>oss</sub>	C <sub>oss</sub> Stored Energy		7		µJ	V <sub>AC</sub> = 25 mV	Fig 16
E <sub>ON</sub>	Turn-On Switching Energy		31		µJ	V <sub>DS</sub> = 1.2 kV, V <sub>GS</sub> = -5/20 V	Fig. 26
E <sub>OFF</sub>	Turn Off Switching Energy		10			I <sub>D</sub> = 2 A, R <sub>G(ext)</sub> = 2.5 Ω, L = 1368 µH, T <sub>J</sub> = 150 °C	
t <sub>d(on)</sub>	Turn-On Delay Time		4		ns	V <sub>DS</sub> = 1.2 kV, V <sub>GS</sub> = -5/20 V I <sub>D</sub> = 2 A, R <sub>G(ext)</sub> = 2.5 Ω, R <sub>L</sub> = 600 Ω Timing relative to V <sub>DS</sub> Per IEC60747-8-4 pg 83	Fig. 27
t <sub>r</sub>	Rise Time		4.8				
t <sub>d(off)</sub>	Turn-Off Delay Time		10.8				
t <sub>f</sub>	Fall Time		40.4				
R <sub>G(int)</sub>	Internal Gate Resistance		24.8		Ω	f = 1 MHz, V <sub>AC</sub> = 25 mV	
Q <sub>gs</sub>	Gate to Source Charge		4.7		nC	V <sub>DS</sub> = 1.2 kV, V <sub>GS</sub> = -5/20 V I <sub>D</sub> = 2 A Per IEC60747-8-4 pg 21	Fig. 12
Q <sub>gd</sub>	Gate to Drain Charge		5.4				
Q <sub>g</sub>	Total Gate Charge		13				

### Reverse Diode Characteristics

Symbol	Parameter	Typ.	Max.	Unit	Test Conditions	Note
V <sub>SD</sub>	Diode Forward Voltage	3.8		V	V <sub>GS</sub> = -5 V, I <sub>SD</sub> = 1 A, T <sub>J</sub> = 25 °C	Fig. 8, 9, 10
		3.3		V	V <sub>GS</sub> = -5 V, I <sub>SD</sub> = 1 A, T <sub>J</sub> = 150 °C	
I <sub>S</sub>	Continuous Diode Forward Current		4	A	T <sub>c</sub> = 25 °C	Note 1
t <sub>rr</sub>	Reverse Recovery Time	20		ns	V <sub>GS</sub> = -5 V, I <sub>SD</sub> = 2 A T <sub>J</sub> = 25 °C V <sub>R</sub> = 1.2 kV dif/dt = 1200 A/µs	Note 1
Q <sub>rr</sub>	Reverse Recovery Charge	24		nC		
I <sub>rrm</sub>	Peak Reverse Recovery Current	6.5		A		

Figure B.9: Half-bridge Inverter Semiconductor - Part 2 - Specifications.



[www.vishay.com](http://www.vishay.com)

## MKP1848 DC-Link

Vishay Roederstein

### Metallized Polypropylene Film Capacitors DC-Link Capacitor



#### FEATURES

- High performance DC filter
- Low ESR
- High peak current capabilities
- High RMS current capabilities
- AEC-Q200 qualified
- Mounting: radial
- Material categorization:  
for definitions of compliance please see  
[www.vishay.com/doc?99912](http://www.vishay.com/doc?99912)

AUTOMOTIVE  
GRADE



RoHS  
COMPLIANT

#### APPLICATIONS

- High performance DC filtering
- HEV / EV: i.e. power train and OBC
- Renewable energies inverters
- Motor drives
- Power supplies

QUICK REFERENCE DATA	
Rated capacitance range	1 $\mu$ F to 400 $\mu$ F
Capacitance tolerance	5 %
Rated voltage range, $U_{NDC}$	450 V to 1200 V
Climatic testing class	40/105/56
Rated temperature	85 °C
Maximum permissible case temperature	105 °C, observing voltage derating
Maximum applicable peak to peak ripple voltage	0.2 x $U_{NDC}$
Reference standards	IEC 61071, IEC 60068
Dielectric	Polypropylene film
Electrodes	Metallized dielectric capacitor
Construction	Mono construction
Encapsulation	Plastic case, sealed with resin; flame retardant
Terminals	Tinned wires
Self inductance ( $L_S$ )	< 1 nH per mm of lead spacing
Withstanding DC voltage between terminals <sup>(1)</sup>	1.5 $U_{NDC}$ for 10 s, cut off current 10 mA, rise time $\leq$ 1000 V/s
Insulation resistance	RC between leads, after 1 min > 10 000 s For $U_{NDC} \leq$ 500 V measuring voltage 100 V For $U_{NDC} >$ 500 V measuring voltage 500 V
Life time expectancy	Useful life time: > 100 000 h at $U_{NDC}$ and 70 °C FIT: < $10 \times 10^{-9}$ /h (10 per $10^9$ component h) at 0.5 x $U_{NDC}$ , 40 °C
Marking	C-value; tolerance; rated voltage; code for dielectric material; code for manufacturing origin; manufacturer's type designation; manufacturer's logo; year and week of manufacture

Figure B.10: Film Capacitors - Part 1 - Features.

ELECTRICAL DATA AND ORDERING CODE															
U <sub>NDC</sub> AT 85 °C (V)	CAP. <sup>(8)</sup> (μF)	DIMENSION <sup>(5)</sup> (mm)			P1 (mm)	P2 (mm)	dV/dt (V/μs)	I <sub>PEAK</sub> (A)	I <sub>RMS</sub> <sup>(2)</sup> (A)		ESR <sup>(3)</sup> (mΩ)		tan δ 10 kHz ( $< 10^{-4}$ ) <sup>(4)</sup>		ORDERING CODE <sup>(1)</sup>
		w	h	l					2 PINS	4 PINS	2 PINS	4 PINS	2 PINS	4 PINS	
450	U <sub>OPDC</sub> AT 70 °C = 500 V, U <sub>OPDC</sub> AT 105 °C = 300 V														
	1	9.0	19.0	32.0	27.5	-	75	75	2.5	-	54	-	85	-	MKP1848510454K2
	2	9.0	19.0	32.0	27.5	-	75	150	3	-	34.5	-	85	-	MKP1848520454K2
	3	11.0	21.0	32.0	27.5	-	75	225	4	-	23.0	-	85	-	MKP1848530454K2
	4	11.0	21.0	32.0	27.5	-	75	300	4	-	20.5	-	85	-	MKP1848540454K2
	5	13.0	23.0	32.0	27.5	-	75	375	5	-	16.5	-	85	-	MKP1848550454K2
	6	15.0	25.0	32.0	27.5	-	75	450	6	-	13.5	-	85	-	MKP1848560454K2
	7	15.0	25.0	32.0	27.5	-	75	525	6.5	-	11.5	-	85	-	MKP1848570454K2
	8	18.0	28.0	32.0	27.5	-	75	600	8.5	-	8.5	-	85	-	MKP1848580454K2
	9	18.0	28.0	32.0	27.5	-	75	675	8.5	-	9.0	-	85	-	MKP1848590454K2
	10	18.0	28.0	32.0	27.5	-	75	750	9	-	8.0	-	85	-	MKP1848610454K2
	12	21.0	31.0	32.0	27.5	-	75	900	10	-	7.0	-	85	-	MKP1848612454K2
	15	20.0	35.0	32.0	27.5	-	75	1125	11.5	-	6.0	-	85	-	MKP1848615454K2
10	18.5	35.5	43.0	37.5	10.2	40	400	7.5	8	13.5	12.0	160	140	MKP1848610454P*	

Figure B.11: Film Capacitors - Part 2 - Electrical data.

ELECTRICAL DATA AND ORDERING CODE															
U <sub>NDC</sub> AT 85 °C (V)	CAP. <sup>(8)</sup> (μF)	DIMENSION <sup>(5)</sup> (mm)			P1 (mm)	P2 (mm)	dV/dt (V/μs)	I <sub>PEAK</sub> (A)	I <sub>RMS</sub> <sup>(2)</sup> (A)		ESR <sup>(3)</sup> (mΩ)		tan δ 10 kHz ( $< 10^{-4}$ ) <sup>(4)</sup>		ORDERING CODE <sup>(1)</sup>
		w	h	l					2 PINS	4 PINS	2 PINS	4 PINS	2 PINS	4 PINS	
450	U <sub>OPDC</sub> AT 70 °C = 500 V, U <sub>OPDC</sub> AT 105 °C = 300 V														
	12	18.5	35.5	43.0	37.5	10.2	40	480	8	8.5	11.5	10.0	160	140	MKP1848612454P*
	15	18.5	35.5	43.0	37.5	10.2	40	600	9	10	9.0	8.0	160	140	MKP1848615454P*
	20	21.5	38.5	43.0	37.5	10.2	40	800	11	12	7.0	6.0	160	140	MKP1848620454P*
	22	21.5	38.5	43.0	37.5	10.2	40	880	11	11.5	7.5	6.5	160	140	MKP1848622454P*
	25	21.5	38.5	43.0	37.5	10.2	40	1000	11.5	12.5	6.5	5.5	160	140	MKP1848625454P*
	30	24.0	44.0	42.0	37.5	10.2	40	1200	13.5	15	5.5	4.5	160	140	MKP1848630454P*
	35	30.0	45.0	42.0	37.5	10.2 / 20.3	40	1400	17	18.5	4.0	3.5	160	140	MKP1848635454P*
	40	30.0	45.0	42.0	37.5	10.2 / 20.3	40	1600	17	18.5	4.0	3.5	160	140	MKP1848640454P*
	40	25.0	45.0	57.5	52.5	10.2	20	800	13	13.5	6.5	6.0	310	280	MKP1848640454Y*
	45	25.0	45.0	57.5	52.5	10.2	20	900	12.5	13.5	7.0	6.0	310	280	MKP1848645454Y*
	50	30.0	45.0	57.5	52.5	20.3	20	1000	15	15.5	5.5	5.0	310	280	MKP1848650454Y*
	55	30.0	45.0	57.5	52.5	20.3	20	1100	15	15.5	5.5	5.0	310	280	MKP1848655454Y*
	60	30.0	45.0	57.5	52.5	20.3	20	1200	15.5	16.5	5.0	4.5	310	280	MKP1848660454Y*
	65	35.0	50.0	57.5	52.5	20.3	20	1300	19	20.5	4.0	3.5	310	280	MKP1848665454Y*
	70	35.0	50.0	57.5	52.5	20.3	20	1400	18	19	4.5	4.0	310	280	MKP1848670454Y*
	75	35.0	50.0	57.5	52.5	20.3	20	1500	19	20.5	4.0	3.5	310	280	MKP1848675454Y*
	80	35.0	50.0	57.5	52.5	20.3	20	1600	19	20.5	4.0	3.5	310	280	MKP1848680454Y*
	90	45.0	45.0	57.5	52.5	20.3	20	1800	-	21.5	-	3.0	-	280	MKP1848690454Y5
	95	45.0	45.0	57.5	52.5	20.3	20	1900	-	21.5	-	3.0	-	280	MKP1848695454Y5
	100	45.0	45.0	57.5	52.5	20.3	20	2000	-	23.5	-	2.5	-	280	MKP1848710454Y5
	200	70.0	65.0	57.5	52.5	20.3	20	2000	-	30.5	-	2.0	-	310	MKP1848720454Y5 <sup>(6)</sup>
	400	130	65.0	57.5	52.5	20.3	10	4000	-	50.5	-	1.5	-	380	MKP1848740454Y5 <sup>(7)</sup>

Figure B.12: Film Capacitors - Part 3 - Electrical data.